NORTHWESTERN UNIVERSITY

Rational Design of Spherical Nucleic Acids as Therapeutic Constructs

A DISSERTATION

SUBMITTED TO THE GRADUATE SCHOOL

IN PARTIAL FULLFILLMENT OF THE REQUIREMENTS

for the degree

DOCTOR OF PHILOSOPHY

Field of Materials Science and Engineering

By

Shengshuang Zhu

EVANSTON, ILLINOIS

September 2019

ABSTRACT

Rational Design of Spherical Nucleic Acids as Therapeutic Constructs

Shengshuang Zhu

Nucleic acids not only are the building blocks of life but also a class of attractive macromolecular therapeutics. However, the delivery of therapeutic oligonucleotides into cells has been a major challenge due to their large size and highly negatively charged backbone. Spherical nucleic acids (SNAs) are a class of emerging nano-biomaterials that overcome this challenge and thus are highly useful as nucleic acids-based therapeutics. SNAs consist of a nanoparticle core with a dense shell of highly oriented oligonucleotides covalently or non-covalently conjugated to it. SNAs can freely enter numerous cell lines by engaging with scavenger receptors on their surface. Once inside the cells, they can act as potent agents for gene regulation or immunomodulation. In addition, SNA cores can be comprised of bioorganic materials, such as liposomes or polymeric nanoparticles, that provide interior space for encapsulating drugs, opening the possibility for dual therapeutics. These unusual biochemical properties of SNAs make them lead drug candidates in gene regulation and immunomodulation therapies.

This thesis further explores the unique properties of SNAs and introduces a new class of SNAs based on polymeric core materials that significantly expand their scope of function. Chapter 1 reviews the field of nanomedicine, especially in the context of SNA development and biochemical properties. Chapter 2 describes the development of a SNA-based topical formulation capable of attenuating abnormal scars. Specifically, liposomal SNAs and AuSNAs were utilized to silence transforming growth factor 1 (TGFβ1), a gene significantly implicated in abnormal

scarring, *in vitro* and *in vivo*. Limitations of conventional SNA constructs are also discussed in this chapter. Chapter 3 describes the design and synthesis of new poly-lactic-co-glycolic acid (PLGA)-SNAs that address these limitations. Chapter 4 further builds on this polymeric SNA construct and details how they can be used to improve gene regulation efficiency by co-delivering two therapeutic agents within a single SNA. The properties and functions of the PLGA-SNAs, including their colloidal stability, peptide release kinetics, and protein knockdown efficiencies were investigated as a function of SNA structure. Chapter 5 provides concluding remarks about the future outlook of SNA development, building upon the knowledge described in the previous chapters.

Thesis Advisor: Professor Chad A. Mirkin

ACKNOWLEDGEMENTS

The decision to pursuing a Ph.D was one that I took very seriously. In fact, I took one-year off after my undergraduate studies to work in order to find out whether pursuing a Ph.D would be the right choice for me. Luckily, I decided to embark on this journey that has allowed me to grow intellectually and personally. During my Ph.D, I received a tremendous amount of help from several groups of remarkable people; their insight and guidance have shaped me into the person I am today.

First, I thank my parents, who have been my primary source of help and inspiration, motivating me to achieve my goals. Born and raised in China, I have always been encouraged by them to be adventurous and explore new things. After high school, I decided to come to the U.S to pursue my undergraduate studies with the hope that I could experience a different culture, make new friends, and learn about the other half of the world. Adjusting to a foreign environment has not been easy, but my parents were always there to listen to and understand me. Intellectually, they always encouraged me to be a critical and creative thinker, which also turn out to be two of the most important attributes for scientific workers.

Second, I thank my Ph. D. advisor, Professor Chad Mirkin, for his dynamic mentoring style that gave me freedom to explore fields that interest me. I never thought about working on nucleic acid therapeutics prior to joining the group, but Professor Mirkin's enthusiasm and determination in overcoming challenges in nucleic acid therapies convinced me that I could make a significant impact by exploring the interface between materials science and biology. In addition to his advising, he provided me with a tremendous amount of support towards my professional and personal development, which I deeply appreciate.

Last but not least, I thank my friends, both in and out of lab, for sustaining me along the way. I firmly believe in building durable friendships and long-lasting relationships with my co-workers, and those friendships will continue and compound in the years ahead.

TABLE OF CONTENTS

LIST OF TABLES AND FIGURES

CHAPTER ONE

INTRODUCTION

1.1 The properties of spherical nucleic acids

1.1.1 Nucleic acid-based therapeutics and delivery methods

Short strands of nucleic acids, known as oligonucleotides, can act as a unique class of macromolecular therapeutics. One of the very first examples of oligonucleotide-based therapies utilized a specific oligodeoxyribonucleotide to inhibit viral mRNA translation[1]. This concept was introduced by Paul Zamecnik in 1978[1] and is now termed with antisense therapy. Antisense treatment normally utilizes a strand of oligodeoxyribonucleotide ranging from 18-25 base pairs to bind with a complimentary mRNA substrate. Antisense oligonucleotide can then alter the gene expression level by RNase-H recruitment[2], exon inclusion/exclusion[2], and miRNA sequestration[2, 3], leading to silencing of specific disease-related protein. This class of therapy is advantageous to traditional small molecule drugs and protein therapies, since in principle, any mRNA can be downregulated via antisense binding[4, 5]. A few other nucleic acid-based therapies
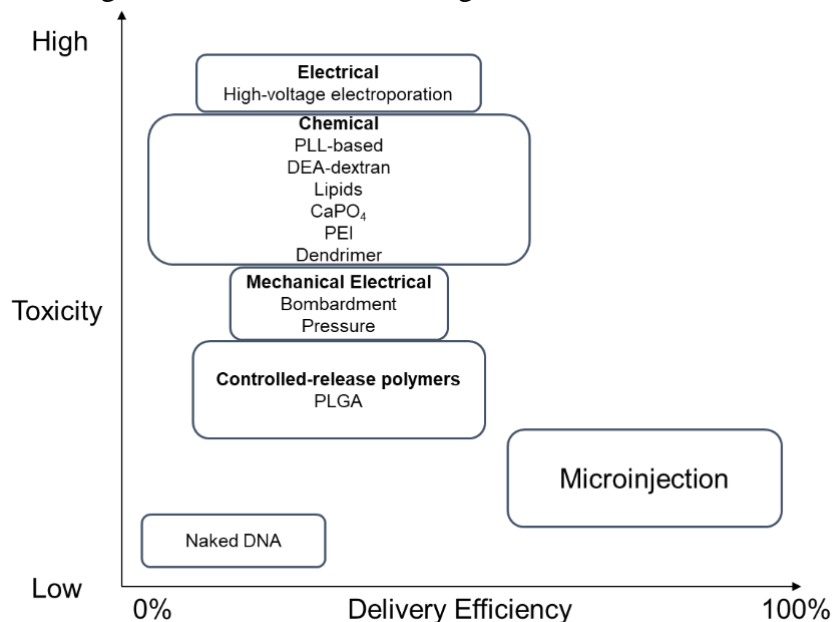
Figure 1.1 Strategies and limitations of therapeutic oligonucleotide intracellular delivery

have been discovered in the past decades[5], including small interference RNA[6, 7], which can regulate the flow of genetic information by introducing a 19-21 base pair RNA duplex, and immunostimulatory CpG[8-12], which can activate immune system by engaging with toll-like receptors[8-11, 13-15]. Nucleic acid-based therapies are advantageous because oligonucleotide-based therapeutics are highly specific and modular due to canonical Watson and Crick base paring.

Despite decades of efforts to discover and develop different modalities of nucleic acid therapies, there are only five FDA-approved oligonucleotide therapeutics. One of the main challenges is that naked oligonucleotides do not enter the cells by themselves[16]. In addition, naked oligonucleotides are rapidly degraded by DNase or RNase[17] in serum after systemic administration[18]. While there has been progress in overcoming the delivery challenges of nucleic acids[19, 20], most delivery methods either suffer from high intracellular toxicity or low delivery efficiency as illustrated by Figure 1.1[19, 21]. While viral delivery method has been tested in the clinics, the discussion of this thesis is only confined to non-viral vector due to potential safety issues with viral vector delivery methods. This thesis will first review the distinct biochemical properties that define the SNA structure and discuss its potential applications.

1.1.2 Biochemical properties of spherical nucleic acids

Spherical nucleic acids (SNAs) is a novel class of biomaterials that hold the potential to overcome the abovementioned challenges. The first SNAs were introduced in 1996 by Mirkin et
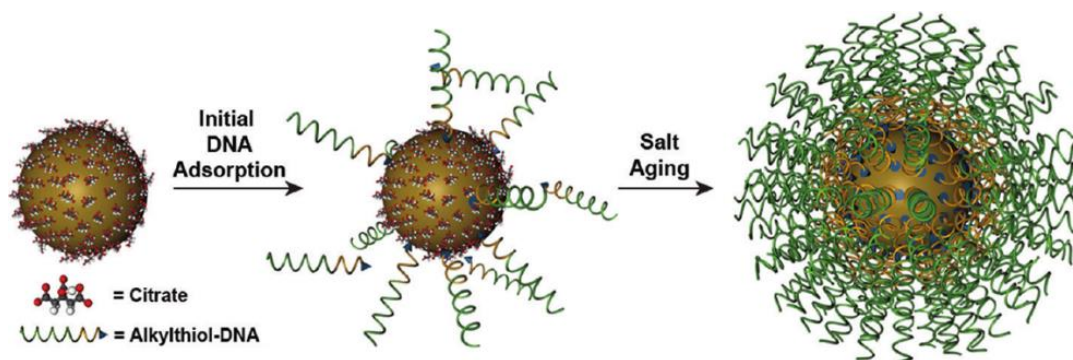
Figure 1.2 Preparation of AuSNAs by salt aging method. Au nanoparticle core was initially capped with citrate, a stabilizing ligand soon displaced by thiol-modified oligonucleotides. NaCl was gradually added to increase the salt concentration of the solution so that the negative charge of oligonucleotide can be screened, resulting in a dense shell of oligonucleotide highly radially oriented on the nanoparticle surface.

al[22]., where a 13 nm Au nanoparticle core was densely functionalized with thiol-modified oligonucleotides by salt-aging method (Figure 1.2).

It turns out that densely arranging oligonucleotides radially on the nanoparticle surface
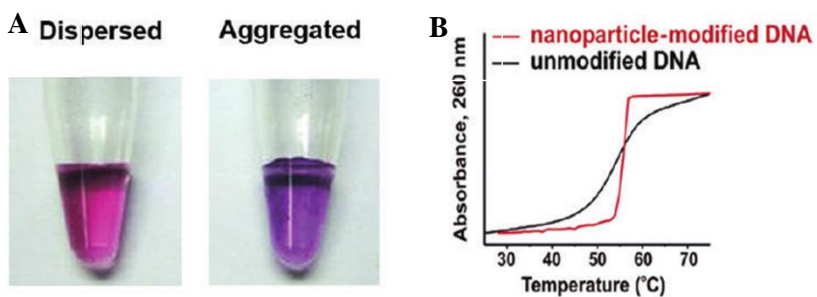
Figure 1.3 Cooperative binding property of SNAs. (A) Aggregation of SNAs via Watson and Crick base pairing of complementary sequences. (B) Elevated and sharp melting transition of SNAs.

results in very distinct properties from linear oligonucleotides. This part focuses on two of them: cooperative binding of the oligonucleotide shell and enhanced resistance to nuclease degradation. While SNA constructs have also been exploited as a novel programable materials and exhibit many interesting properties in materials assembly[23-25], this review chapter will primarily focus on the biochemical properties of SNAs pertaining to therapeutic development. Linear nucleic acid duplex can hybridize by means of canonical Watson and Crick base pairing. As temperature increases, the duplex will dehybridize. The hybridization of SNAs differs greatly from that of their linear counterpart. Following the Watson and Crick base pairing, SNAs bearing complementary sequences can hybridize, leading to a network of polymeric structure[22, 26, 27]. The hybridization can be visualized by a distinct color change from red (un-hybridize) to blue (hybridize) (Figure 1.3A). Different from their linear counterpart, SNAs have a higher melting temperature and much sharper melting transition (Figure 1.3B). These differences may arise from higher local salt concentration surrounding SNAs and more concentrated strands confined to the SNA surface. This

sharp melting transition creates the basis for highly sensitive and selective nucleic acid detection and diagnostic methods[28-32].

The second unique property of SNAs is that the oligonucleotide shell on the SNA surface
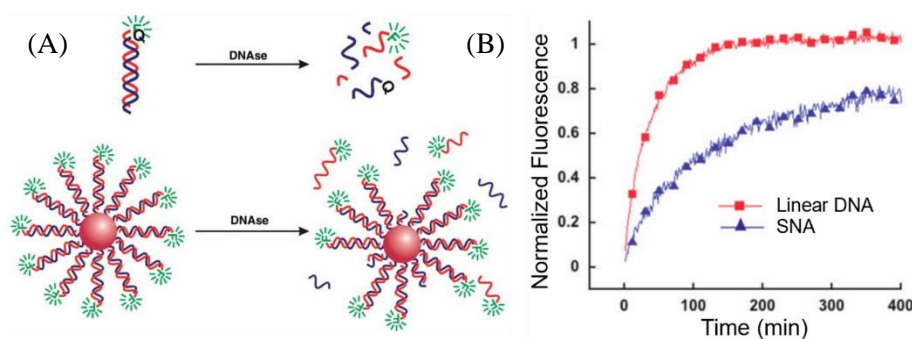
Figure 1.4 Nuclease resistance of oligonucleotide shell of SNAs. (A) Design of a fluorescence turn-on assay to monitor the stability of oligonucleotide. (B) Degradation profile of molecular DNA or oligonucleotide shell of SNAs

Figure 1.5 Degradation profile of oligonucleotide shell on SNAs with different surface coverage. (A) Degradation profile as a function of surface coverage of SNAs subjected to DNase I. (B) Degradation profile as a function of surface coverage of SNAs subjected to Turbo DNase

is more resistant to nuclease degradation than their linear counterpart. Figure 1.4 (A) shows a fluorescence quenching assay performed by Seferos [33] *et al* to compare stability of oligonucleotide shell to molecular DNA. To investigate the stability, a strand of DNA labeled with fluorescein was duplexed with another DNA labeled with a

dabcyl quencher. When the DNA duplex was degraded, a fluorescence turn-on from fluorescein

will be detected. Molecular DNA or SNAs were subject to DNase I challenge, and fluorescence turn-on was monitored. Figure 1.4B demonstrates that the oligonucleotide shell of SNAs degrade significantly slower than molecular DNA. They further hypothesized that the high local salt concentration, such as Na^+, inhibits enzymatic activity of DNase I. This hypothesis was tested by first showing more surface coverage by DNA results in slower degradation profiles of SNAs (Figure 1.5A). Then Turbo DNase, whose activity is less sensitive to salt concentration, was utilized to challenge a series of SNAs with different oligonucleotide coverage. It turned out that Turbo DNase is less affected by SNA surface coverage (Figure 1.5B), implying that salt concentration is the main driver that reduce DNase I activity in the vicinity of oligonucleotide shell.

1.1.3 Spherical nucleic acids delivery into cells and tissues

As previous part has alluded to, arranging a dense shell of oligonucleotides radially on a nanoparticle surface changes their biochemical properties. More remarkably, SNAs can enter cells freely despite their large size and highly negatively charged surface potential.
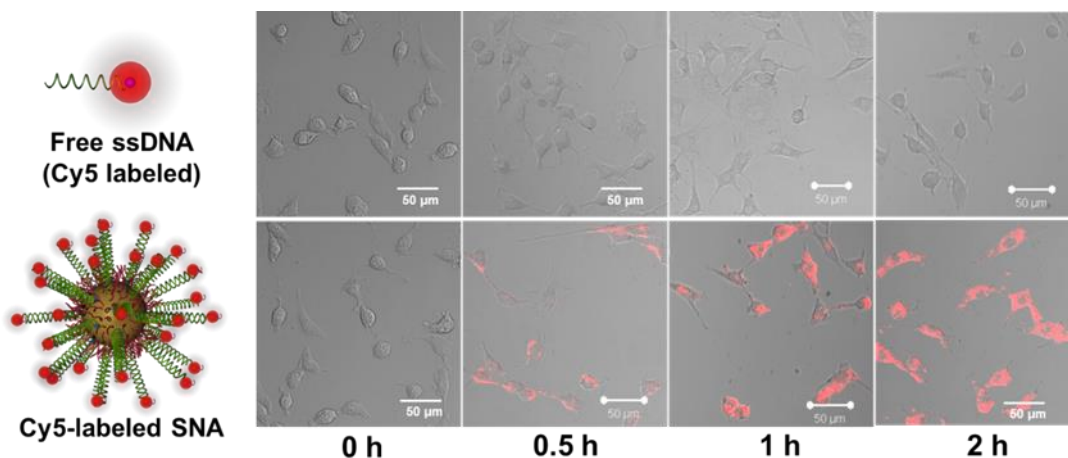
Figure 1.6 Cellular uptake of Cy5-labeled free DNA and SNAs into C166 cells over 2 h.

As can be seen from Figure 1.6, SNAs labeled with a Cy5 fluorophore can enter C166 cells as early as 0.5 h while the identical oligonucleotides with the same DNA-to-DNA concentration have minimal cellular entry[34, 35]. Importantly, compared to conventional transfection agent-mediated delivery of nucleic acids which are toxic and immunogenetic, SNAs are nontoxic (Figure 1.7)[36] and do not elicit cellular immune response. Figure 1.8 demonstrates AuSNAs delivering interferon stimulatory DNA elicit significantly less immune response, as measured by the amount of IFN-β, IL-1β, and IL-6
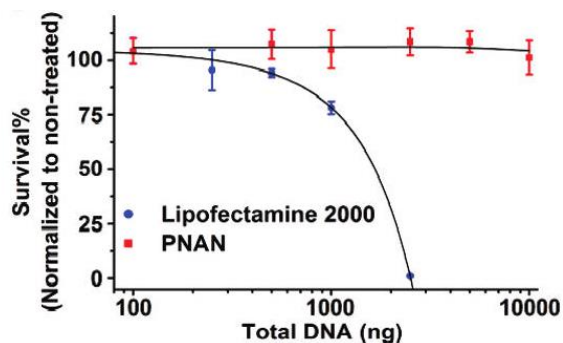
Figure 1.7 Cytotoxicity induced by SNAs as compared to commercial transfection agent.
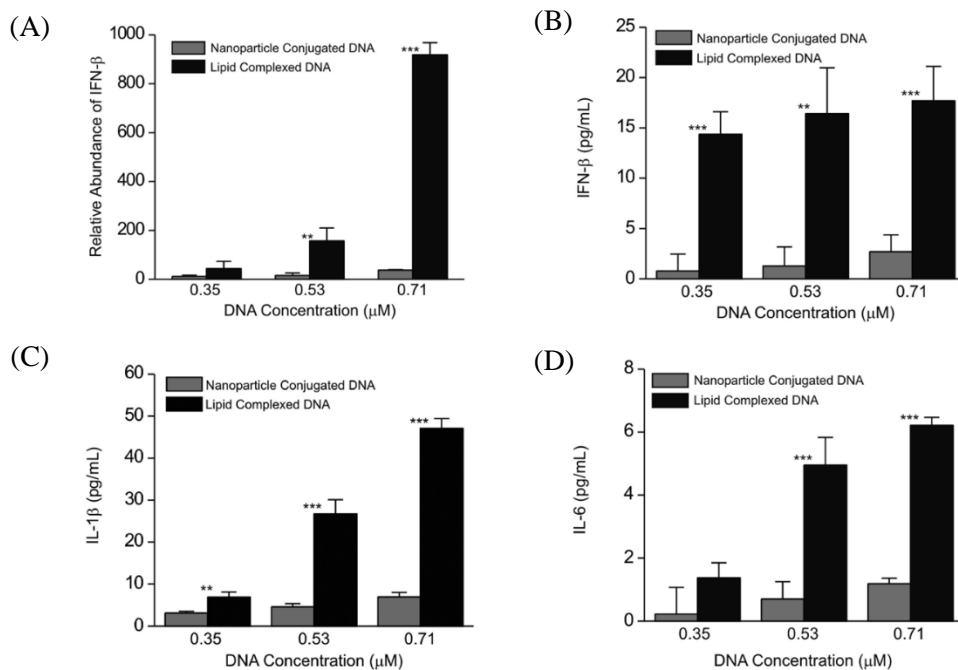
Figure 1.8 Detection of innate immune response related cytokines. (A) IFN-β mRNA level induced by AuSNAs or lipid complexed DNA. (B) IFN-β protein production induced by AuSNAs or lipid complexed DNA. (C) IL-1β protein concentrations induced by AuSNAs or lipid complexed DNA. (D) IL-6 protein concentrations induced by AuSNAs or lipid complexed DNA.

secreted, than the same DNA transfected by a lipid-based transfection agent[37]. This result shows that SNAs will unlikely induce innate immune response and be more compatible with living systems.

A detailed mechanistic study by Choi and Wu *et al* demonstrates that SNAs enter these cells by scavenger receptor A (SR-A) and caveolae-mediated endocytosis pathways[34, 35], where the three-dimensional architecture of SNAs selectively engages these receptors and lipid-raft
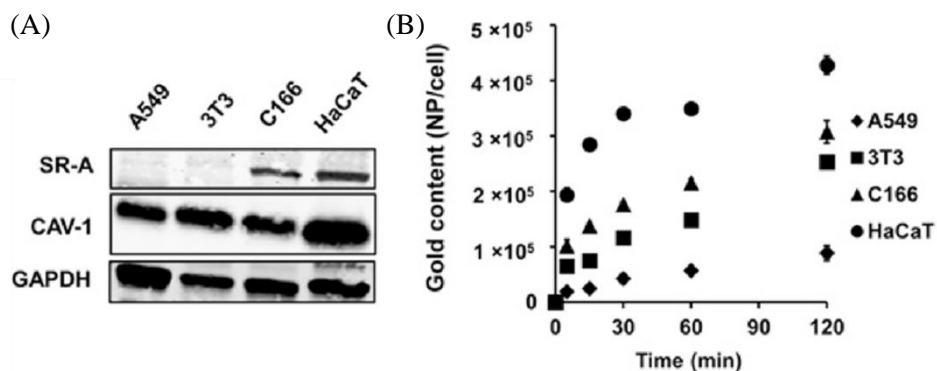
Figure 1.9 Correlation of the amount of SR-A and caveolae with cellular uptake of SNAs in A549, 3T3, C166, and HaCaT cells. (A) The amount of SR-A and caveolae expressed by A549, 3T3, C166, and HaCaT measured by Western Blot. (B) Differential uptake of SNAs into these four cell lines.

proteins, leading to efficient cellular uptake. Figure 1.9 shows a clear correlation between SR-A and caveolae expression level and cellular uptake among four cell lines. Figure 1.9 (A) shows A549 (adenocarcinomic human epithelial cells) and 3T3 (mouse fibroblast) express less SR-A and caveolae than C166 (mouse endothelial cells) and HaCaT (human keratinocytes), and Figure 1.9 (B) shows that SNAs endocytosed into A549 and 3T3 with a slower kinetics than C166 and HaCaT.

In a follow-up study, Wu *et al* shows that SNAs taken up by C166 cells undergo endocytic pathways that result in accumulation inside endosomes (Figure 1.10). The accumulation of SNAs inside endosomes poses a challenge in SNAs accessing cytosol, a place where gene
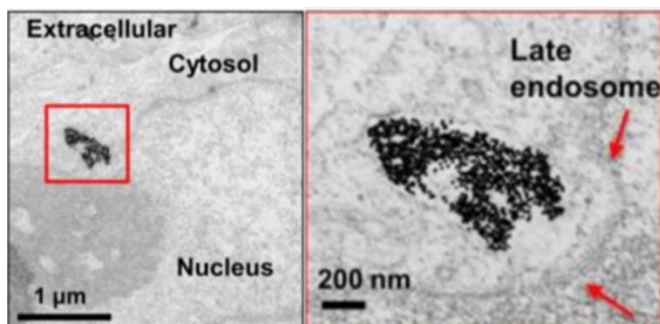
Figure 1.10 Accumulation of AuSNAs inside late endosome of C166 cells after 24 h treatment.

regulation via antisense or RNAi pathways occurs. This thesis will later elaborate on the rational design of SNA structures capable of improving endosomal escape. In Wu's work, it was also
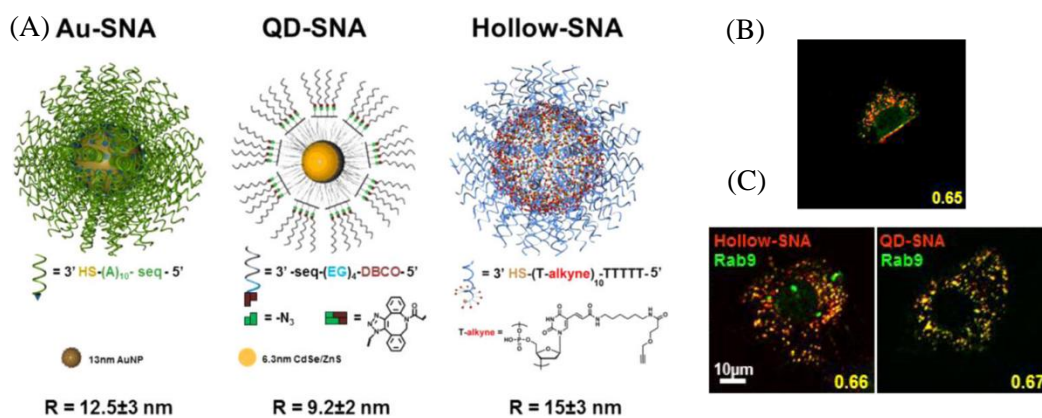
Figure 1.11 Intracellular fate of SNAs comprised of different core compositions. (A) SNAs synthesized from Au, CdSe/ZnS (quantum dot), and hollow nanoparticle core. (B) and (C) Endosomal accumulation of AuSNAs, QD-SNAs, and Hollow-SNAs in C166 cells after 4 h treatment.

demonstrated that cellular uptake of SNAs is likely independent of the identity of the chemical composition of the core materials. Figure 1.11 shows three types of SNAs made from Au, quantum dot, and hollow nanoparticle core end up accumulating inside endosomes of C166 cells after 4h treatment. This result indicates SNAs' cellular uptake profile is mainly dictated by the

oligonucleotide shell instead of the nanoparticle core, a property underlying the future development of biocompatible, organic SNAs.

The interplay between SNAs' three-dimensional oligonucleotide shell and SR-A leads to understanding how the loading density of SNAs affects cellular uptake First, it was shown that cellular uptake of SNAs highly correlates with surface loading density of oligonucleotides, as demonstrated by Giljohann[38] *et al* in Figure 1.12, that SNA cellular uptake into A549 cells increases as the surface loading density of oligonucleotide

Figure 1.12 The amount of SNA uptake into A549 cells correlates with surface loading density

increases from 20 strands/particle to 80 strands/particle. This observation points to the importance of maximizing oligonucleotide loading on the nanoparticle surface.
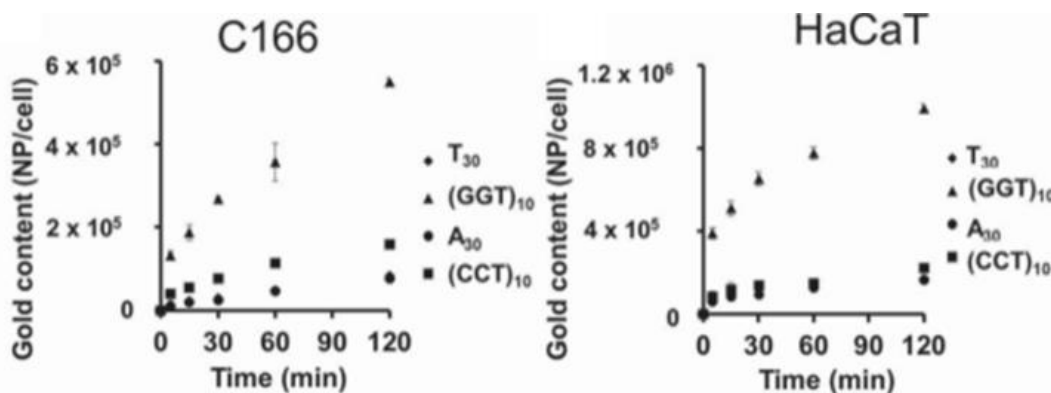
Figure 1.13 SNAs functionalized with different sequences exhibit differential but consistent uptake profile in C166 and HaCaT cells.

Second, Narayan *et al* illustrated that SNA cellular uptake is sequence-specific[39]. G-quadruplex is a high affinity binder to SR-A, and it was observed in Narayan's work that SNAs functionalized with poly(guanine) (poly-G) sequence exhibit the highest cellular uptake across C166, HaCaT, 3T3, and A549 (Figure 1.13) cells measured by inductively coupled plasma mass spectrometry (ICP-MS)

Lastly, Song *et al* studied cellular uptake of SNAs with respect to backbone modifications of oligonucleotides[40]. In this study, five SNAs were prepared with different backbone modifications of oligonucleotides, including regular DNA, locked DNA (L-DNA), RNA, 2'-methoxy-RNA (2'-OMe-RNA), and 2'-fluoro-RNA (2'-RNA). Flow cytometry (Figure 1.13A) and ICP-MS (Figure 1.14B) both show that SNAs bearing 2'-fluoro-RNA have the highest cellular uptake while SNAs bearing 2'-OMe-RNA have the lowest cellular uptake.

In addition to intracellular delivery of oligonucleotides, SNAs are also capable of accessing tissue of interest that is conventionally deemed hard to reach by traditional delivery

(A) (B)
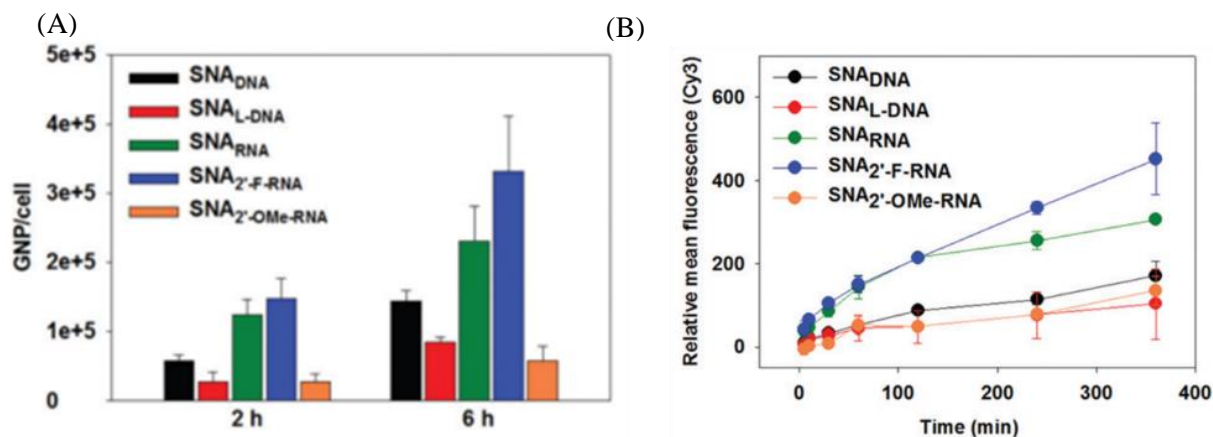
Figure 1.14 Differential uptake of SNAs made from backbone-modified oligonucleotides. (A) The mount of uptake measured by ICP-MS. (B) The amount of uptake measured by flow cytometry.

methods for macromolecular therapeutics, such as skin. Zheng *et al* demonstrated that topically applied AuSNAs were able to penetrate skin[41]. Figure 1.15 A shows vertical penetration of SNAs labelled by Cy5 into intact mouse skin. The SNAs bearing antisense sequences targeting epidermal growth factor receptor (EGFR) can silence it after skin penetration. This access to skin opens up possibility for transdermal drug delivery mediated by the SNA construct, which will potentially lead to a more localized, patient self-manageable therapy that exhibits less systematic side-effect. The application of SNAs in treating skin disease will be discussed in details in the later chapter of this thesis.
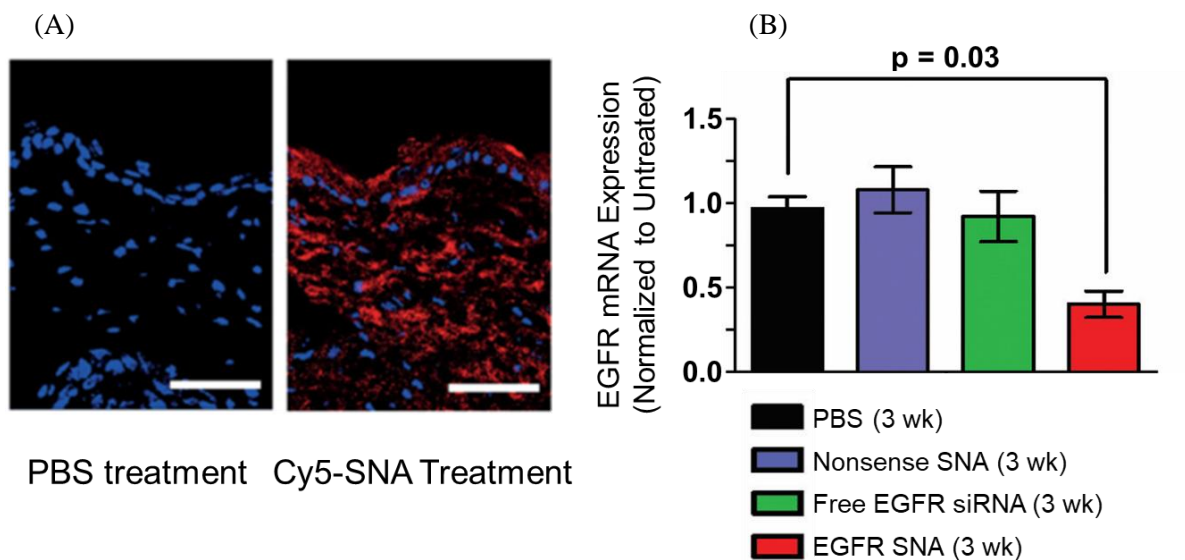
Figure 1.15 Topically applied AuSNAs penetrate mouse skin and effectively downregulate mRNA in skin cells. (A) Right: PBS treated mouse skin; left: Cy5-labeled AuSNAs treated mouse skin. Scale bar = 100 µm. (B) EGFR mRNA expression level after 3 weeks of topical treatment of AuSNAs targeting EGFR.

1.1.4 Modulating spherical nucleic acid properties by changing the core materials

(A)

(B)

(C)

(D)
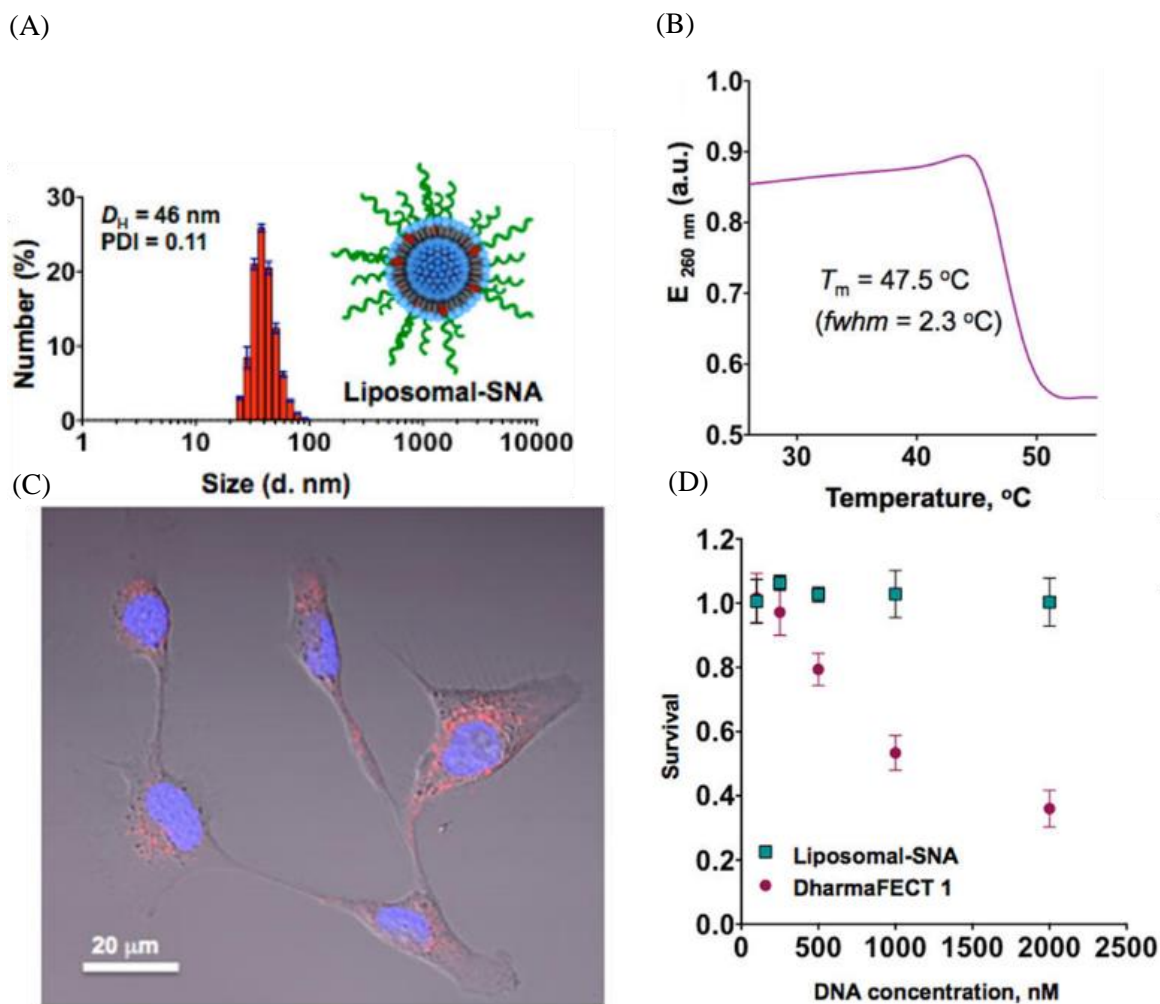
Figure 1.16 LSNAs with a narrow size distribution shows sharp melting transition, effective cellular uptake, and biocompatibility. (A) and (B) LSNA size distribution and melting profile. (C) and (D) Cellular uptake of LSNAs into SKOV3 cells and biocompatibility of LSNAs.

As Wu *et al* suggests in her work, intracellular fate of SNAs is mainly dictated by the oligonucleotide shell instead of the nanoparticle core. Indeed, SNAs comprising of Au, CdSe/ZnS, or hollow core mainly accumulated inside late endosomes after 4 h. This discovery leads to research efforts focused on modulating SNA properties and designing more biocompatible SNAs

by substituting Au nanoparticle core with benign nanoparticle cores that entail more functions. To this end, lipid-based SNA (liposomal SNAs, or LSNA) is one of the most benign core materials our group has developed so far. Bang *et al* demonstrated a facile preparation method to synthesize monodisperse LSNA with a hydrodynamic size of ~50 nm (Figure 1.16A). LSNAs retain the characteristic properties resembling AuSNAs, including sharp melting transition (Figure 1.16B), rapid cellular uptake (Figure 1.16C), and biocompatibility (Figure 1.16D). Not only lipid is a more clinically relevant material than Au, but the aqueous liposomal core of LSNAs can be utilized to encapsulate additional therapeutic cargos[42]. The application of LSNAs will be discussed in the following chapters.
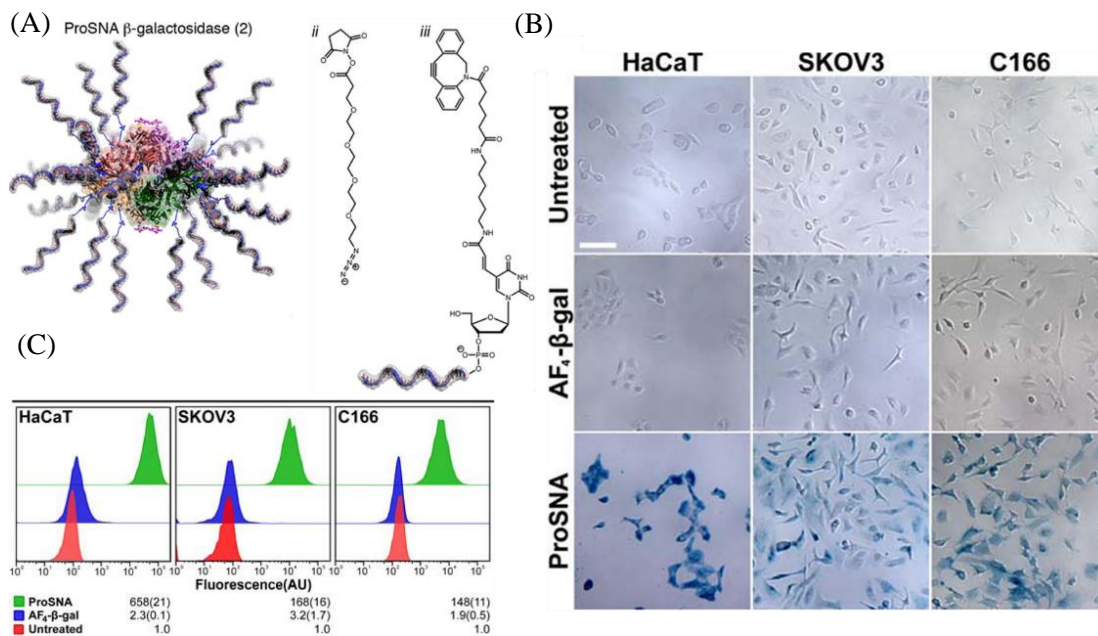
Figure 1.17 Synthesis scheme and biochemical properties of β-galactosidase ProSNAs. (A) Representation of β-galactosidase ProSNAs, (ii) amine-reacting azide-containing N-hydroxy succinimide linker, and (iii) cyclooctyne, dibenzocyclooctyne (DBCO)-modified DNA that can "click" to the linker. (B) Cellular uptake of ProSNAs and unmodified β-galactosidase into three cell lines. (C) Image-based enzymatic assay measuring intracellular activity of β-galactosidase delivered into three cell lines.

Another example of SNA with a unique core composition is protein SNA (ProSNA)[43]. Different from other SNAs with synthetic materials as the core composition, this novel class of SNAs comprised of a molecularly pure nanoparticle core (protein) representing a high degree of structural control and functional homogeneity. Brodin *et al* functionalized β-galactosidase with DNA strands via copper-free click chemistry that yields ~25 strands per protein (Figure 1.17A). Importantly, β-galactosidase ProSNAs freely enter HaCaT, SKOV3 (human ovarian cancer cells), and C166 cells, while naked, unmodified β-galactosidase shows minimal uptake into these cells in 12 h treatment at 0.1 nM β-galactosidase concentration (Figure 1.17C). In addition, β-galactosidase

ProSNAs remain catalytically active for hydrolysing the substrate of β-galactosidase, Xgal, as can be visualized by blue products throughout these three cell lines. Unmodified β-galactosidase does not have catalytic activity in these three cell lines as no hydrolysis products can be visualized (Figure 1.17B).

As demonstrated here, the SNA construct possesses a high degree of control over structure and function via the tunability of the core composition. I will further exploit this modularity in this thesis by creating a new class of SNAs comprised of a biodegradable and biocompatible polymeric material that holds potential for combination therapies.

1.2 Spherical nucleic acid-based gene regulation and immunomodulation therapies

The three-dimensional architecture of oligonucleotide shell residing on SNAs not only serve as a communicator for engaging SR-A in the process of endocytosis, but also can be functional for therapeutic purposes. In this part of the thesis, SNAs' applications in gene silencing and immunomodulation will be reviewed.

1.2.1 Spherical nucleic acid as a gene silencer
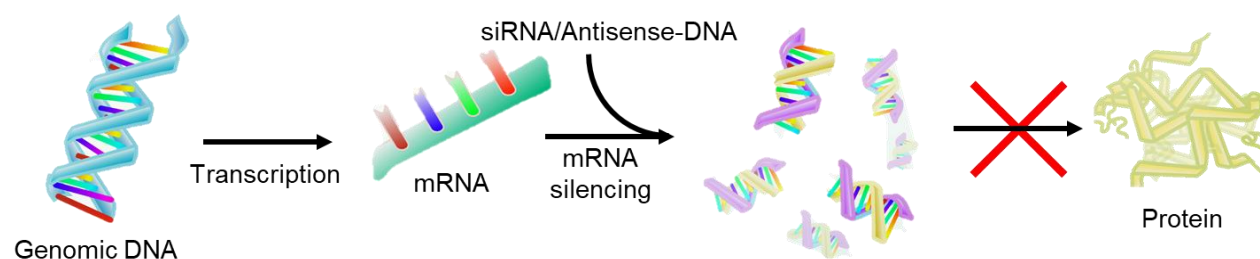
Figure 1.18 Schematic of gene regulation via siRNA- or antisense DNA-mediated cleavage of mRNA

Gene regulation is an important class of oligonucleotide-based therapy. In gene regulation, siRNA or antisense DNA are introduced to cleave the target mRNA substrate, and thus the protein of interest can be silenced in a sequence-specific manner (Figure 1.18). The molecular mechanism of RNAi and antisense DNA-mediated knockdown is different, but they face similar delivery challenges, therefore, this thesis will consider these two pathways rather interchangeably. The advantage of gene regulation therapy is that in principal, it can turn down any gene of interest following a set of design rules to design siRNA or antisense DNA, including those targets deemed "undruggable" by traditional small molecule drugs[4, 5, 44, 45]

To achieve the desired therapeutic outcome, siRNA and antisense DNA need to be delivered into cells. As chapter 1.1.1 has reviewed, most siRNA and antisense DNA intracellular delivery methods are either ineffective or toxic. SNAs bearing siRNA or antisense DNA as a functional entity can freely cross cell membranes with minimal toxicity and immunogenicity. The first example of gene regulation by SNAs was demonstrated by Rosi *et al* with 13 nm Au
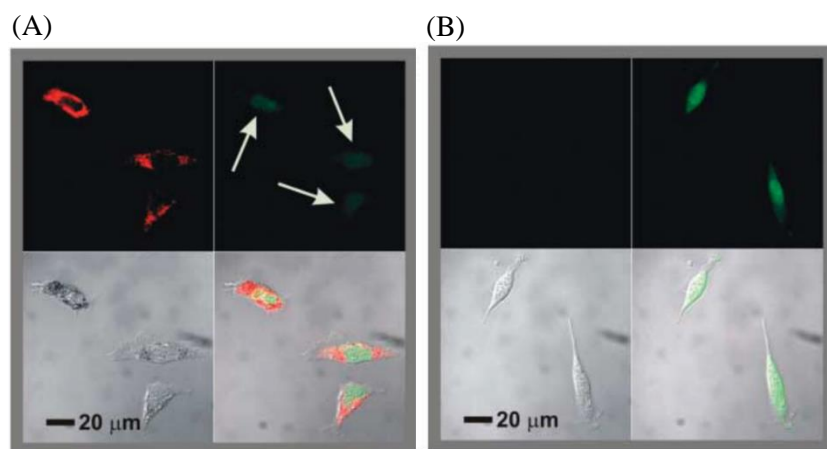
Figure 1.19 Intracellular EGFP silencing of C166 cells by AuSNAs. (A) Confocal image of C166-EGFP cells treated with AuSNAs targeting EGFP. (B) Confocal image of C166-EGFP cells treated with scrambled AuSNAs.

nanoparticles functionalized with antisense oligonucleotides capable of silencing enhanced green fluorescence protein (EGFP) in C166-EGFP cells. Cells treated with these AuSNAs show ~20% decrease in EGFP expression level compared to scrambled AuSNAs (Figure 1.19 A and B)[46].

Follow-up research efforts focus on utilizing the gene silencing capability of SNAs in more clinically relevant models. Jensen *et al* demonstrates that AuSNAs bearing siRNA targeting Bcl2L12, a gene significantly implicated in glioblastoma (GBM), were able to knockdown Bcl2L12 in U87MG GBM cells (Figure 1.20A)[47]. In addition, systemically delivered AuSNAs were able to penetrate blood brain barrier (BBB) (Figure 1.20B) and accumulated six-fold more in tumour-bearing brain tissues than normal brain tissues (Figure 1.20C), suggesting SNAs

infiltration into tumour-bearing tissues may be facilitated by compromised BBB. Furthermore, these AuSNAs were able to silence Bcl2L12 *in vivo* and result in tumour weight reduction and improved survival in a xenograft mouse model compared with scrambled AuSNA treatment (Figure 1.20D). In this work, the distribution half-life of AuSNAs is calculated to be ~ 1 minute while the elimination half-life is ~ 8.5 hours.
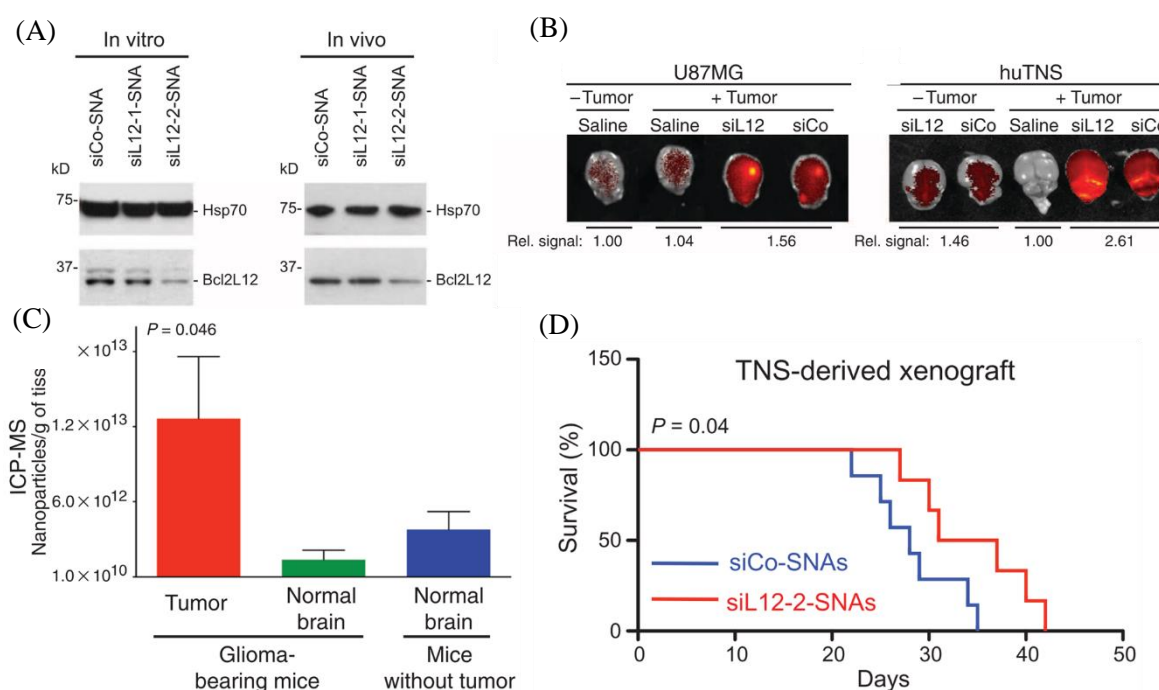
Figure 1.20 Silencing of Bcl2L12 by AuSNAs leads to improved therapeutic outcomes of GBM. (A) Knockdown of Bcl2L12 *in vitro* and *in vivo* by AuSNAs. (B) IVIS imaging of brains with or without U87MG or huTNS. Yellow indicates increased accumulation of AuSNAs labelled by Cy5.5. (C) Accumulation of SNAs measured by ICP-MS in brains with or without GBM. (D) Survival curve of TNS-derived xenorgraft mouse model treated with AuSNAs targeting Bcl2L12 or control AuSNAs.

Our group has also spent efforts on evaluating whether SNAs comprised of a benign nanoparticle core composition were able to knock down disease related genes. Banga *et al* demonstrated that LSNAs bearing DNA capable of silencing epidermal growth factor receptor 2

(*HER2*) mRNA can downregulate *HER2* protein by ~85% in SKOV3 cells (Figure 1.21 A and D)[42]. Young *et al* designed a hollow core SNA by oxidatively removing the Au nanoparticle with I$_2$. The hollow core SNAs bearing anti-EGFP sequences were able to enter cells, exhibit sharp melting transition, and downregulate EGFP mRNA to the similar degree to AuSNAs (Figure 1.21B and E)[48]. In another work, Zhang *et al* demonstrated a brushed polymeric micelle SNAs comprised of polycaprolactone was able to down regulate EGFP (Figure 1.21 C and F)[49]. All of these studies point to the central function of the densely packed, radially oriented oligonucleotide shell that leads to SNAs' characteristic intracellular properties, while the nanoparticle core can be chosen based on specific applications.
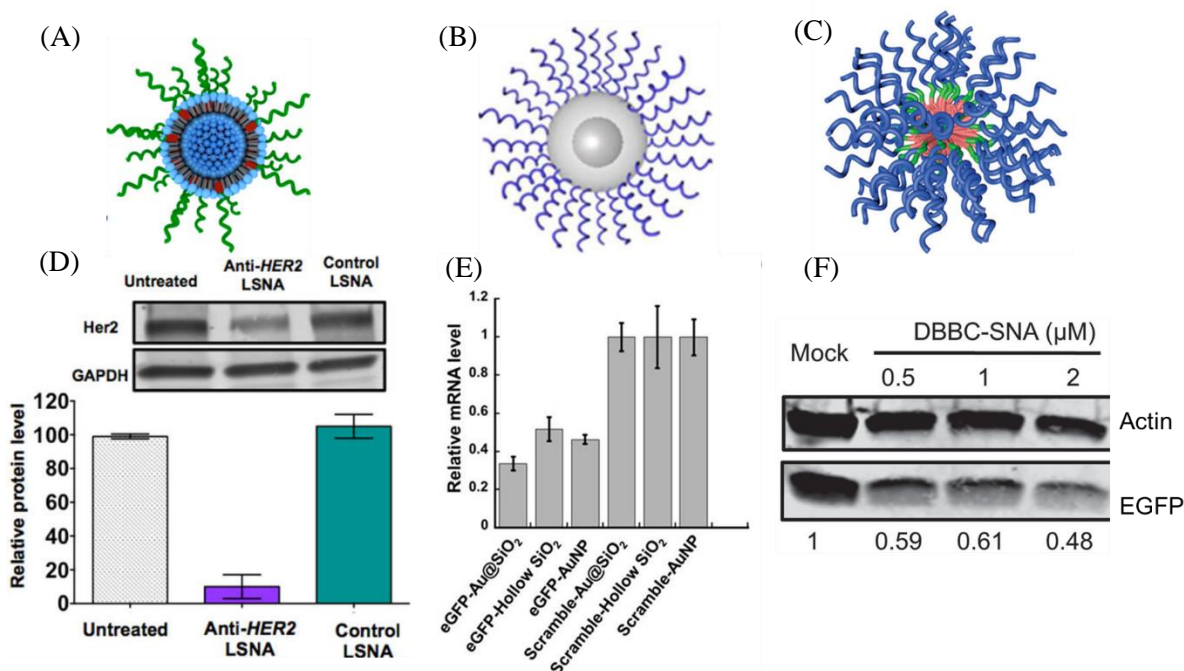
Figure 1.21 SNAs comprised of benign core compositions that show gene knockdown. (A) LSNAs prepared by inserting a tocopherol-modified DNA into lipid bilayer of a liposome nanoparticle core. (B) Hollow core SNAs prepared by etching away the Au nanoparticle core with I_2. (C) DNA-brushed polymeric SNAs prepared by self-assembly of DNA-PCL conjugates. (D) knockdown of *HER2* in SKOV3 cells by LSNAs bearing HER2-targeting antisense DNA measured by qPCR and Western blot. (E) Knockdown of EGFP in C166 cells with hollow core SNAs measured by qPCR. (F) Western blot showing knockdown of EGFP by DNA-brushed SNAs in C166-EGFP cells.

One interesting application is to regulate mRNA located inside the nucleus. For this purpose, Sprangers *et al*[50] exploited the dynamic nature of the LSNA construct and a Ras-related nuclear (RAN) protein-mediated pathway[51] for importing phosphorothioate (PS) oligonucleotides into the nucleus. Nuclear-retained metastasis associated lung adenocarcinoma transcript 1 (Malat1)

was chosen as the target in the study due to its prevalence in several cancers. LSNAs prepared
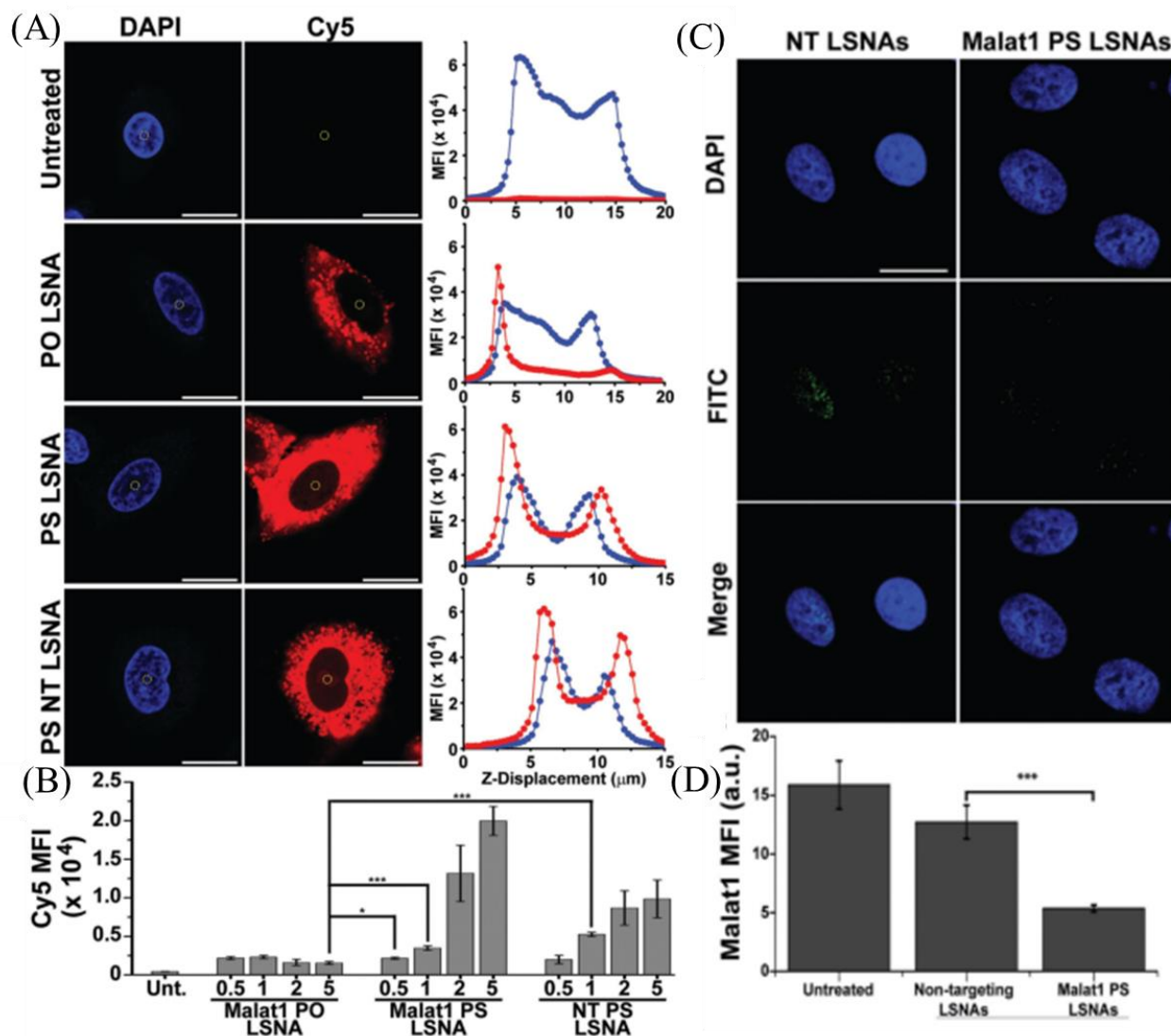
Figure 1.22 Co-localization of PS DNA and PO DNA with the nucleus and their downregulation of Malat1 inside the nucleus. (A) Co-localization measurement of DNA with backbone modifications to the nucleus. The two peaks of blue curve define the edges of the nucleus and the red curves represent Cy5 fluorescence. The middle point of the blue curve represents the center of the nucleus. (B) Quantification of Cy5 MFI that co-localizes with the center of the nucleus (C) Downregulation of Malat1 demonstrated by fluorescence in situ hybridization (FISH) (D) Quantification of gene regulation by FISH.

with PS backbone modified antisense DNA has been shown to colocalize with the nucleus in A549 lung cancer cells (Figure 1.22 A and B) by confocal microscopy while PO LSNAs do not co-localize with the nucleus. A fluorescence in situ hybridization (FISH) assay suggests that after PS antisense enters the nucleus, it downregulates Malat1 (Figure 1.22 C and D).

1.2.2 Spherical nucleic acid as an immunomodulators

Another route of application for SNAs is to act as an immunomodulator. Based on the study conducted by Wu *et al*, SNAs endocytosed into cells primary accumulate inside endosomes, a cellular compartment where many immunomodulating toll-like receptors (TLRs) essential to pathogen recognition reside. Immunostimulatory SNAs (IS-SNAs) bearing CpG
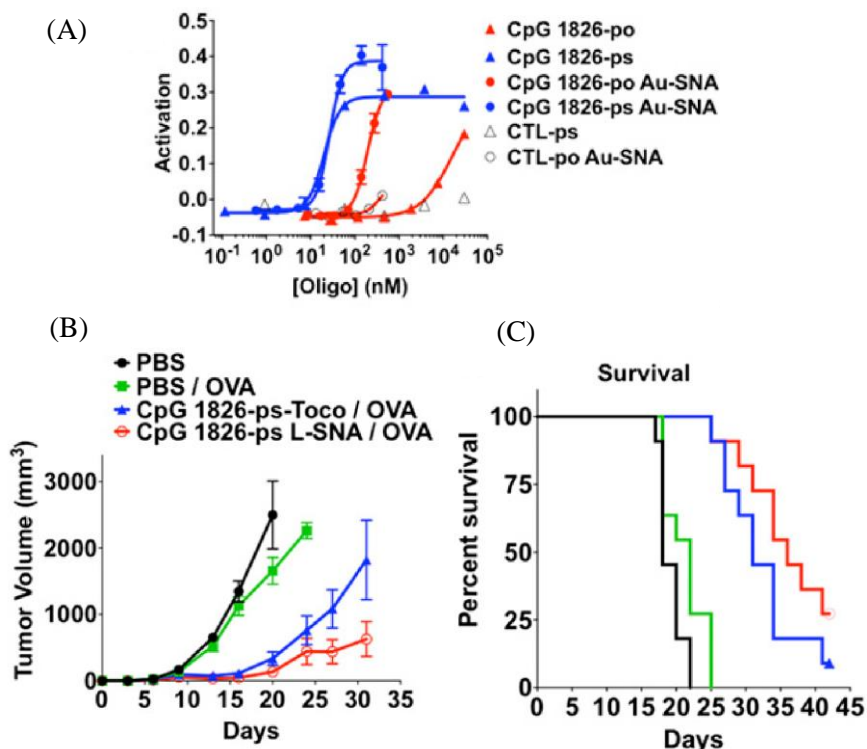
Figure 1.23 IS-SNAs capable of stimulating TLR9 were able to reduce tumor burden and improve survival rate. (A) IS-SNAs stimulating TLR9 in a sequence-specific and concentration dependent manner. (B) IS-SNAs as a vaccine reduce tumor volume in a statistically significant manner. (C) IS-SNAs improve therapeutic outcome in a E.G7-OVA transgenic mouse model.

motifs have been demonstrated to activate TLR9 in a sequence-specific manner (Figure 1.23A)[52]. Once SNAs were inside endosomes, the oligonucleotide shell resists nuclease degradation and act as a high affinity binder to these TLRs. The densely functionalized, highly orientated CpG shell of IS-SNAs shows significantly higher potency in agonizing TLR-9 than their linear counterpart

(Figure 1.23B). IS-SNAs carrying OVA antigen and CpG were capable of reducing tumour growth and doubling survival in an E.G7-OVA lymphoma model (Figure 1.23 B and C). Importantly, the LSNA co-delivering CpG and OVA antigen outperformed the mixture of tocopherol terminated CpG and OVA antigen, underscoring the effectiveness of the three-dimensional architecture of SNAs in engaging receptors.

In addition to activating TLRs, LSNAs were also able to selectively suppress TLRs. Ferrer *et al* showed that LSNAs bearing a TLR9 inhibitor, INH-18 or encapsulated with or a TLR4 inhibitor, TAK-242, were able to suppress the activity of TLR9 and TLR4 respectively in a concentration-dependent manner in HEK-Blue cells (Figure 1.24)[53]. SNAs supressed TLR4 or TLR9 in a more potent manner than free TAK-242 or linear INH-18 probably due to SNAs' superior cellular uptake into HEK-Blue cells.

(A)   (B)
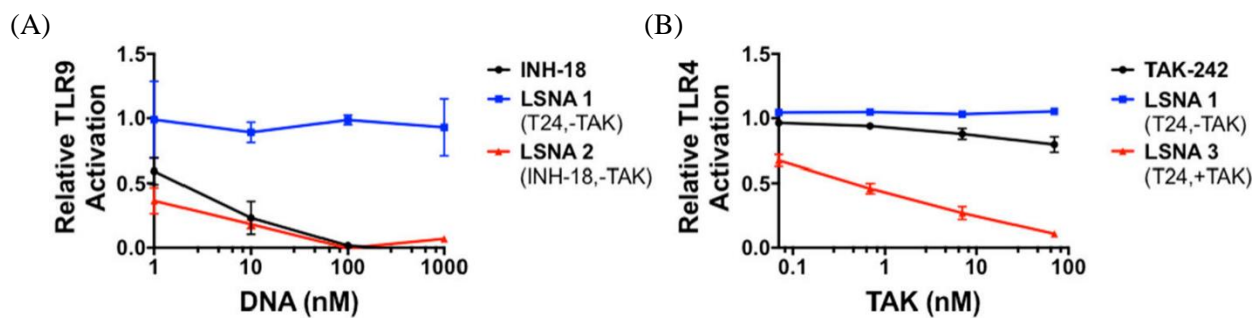
Figure 1.24 LSNAs suppressing TLR9 and TLR4 in HEK-Blue macrophages. (A) Activation of TLR9 of HEK-Blue macrophages after LSNA treatment. (B) Activation of TLR4 of HEK-Blue macrophages after LSNA treatment.

1.2.3 Spherical nucleic acids as a drug carrier

Being able to enter numerous cell lines provides the SNA the ability to deliver not only functional oligonucletiodes (siRNA, antisense DNA, immunostimulatory CpG), but also small molcule drugs that can induce cell cytoxicity. In this chapter, two such examples will be reviewed.

(A)

(B)
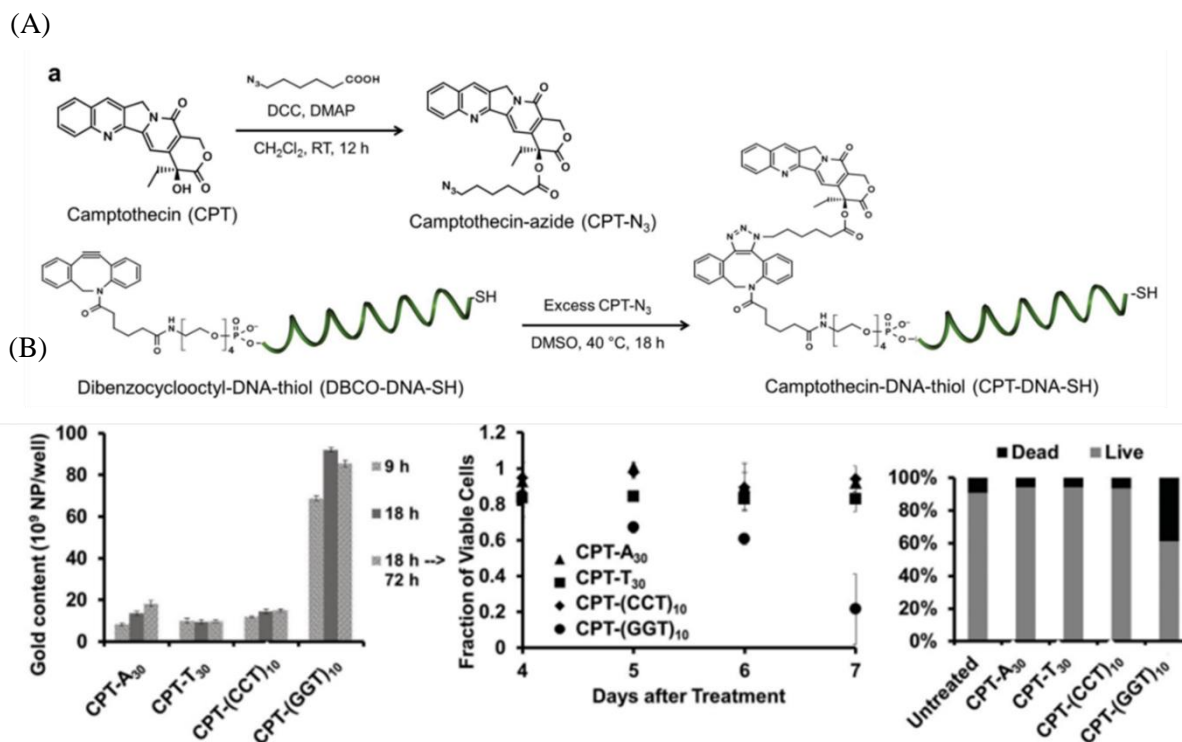
Figure 1.25 Conjugating camptothecin (CPT) leads to intracellular delivery and cytotoxicity. (A) Conjugatoin strategy for attaching CPT covalently to the periphery of a DBCO-terminated DNA. (B) Cellular uptake and cytotoxicity of CPT-AuSNAs.

Narayan *et al* demonstrated that camptothecin (CPT) can be delivered intracellularly to A549 lung cancer cells by conjugating it to the periphery of AuSNAs via copper-free click chemistry (Figure 1.25A)[39]. CPT-AuSNAs prepared with diferent nucleic acid sequences exhibit differential uptake to A549 cells, leading to varying toxicity with GGT sequence showing the highest toxicity (Figure 1.25B).

In an earlier study, Dhar *et al* shows that c,c,t-[Pt(NH$_3$)$_2$Cl$_2$(OH)(O$_2$CCH$_2$CH$_2$CO$_2$H)] (**1**) conjugated to peripheral amine-terminated oligonucleitodes (Figure 1.26A) could enhance the therapuetic outcome in certain cell lines[54]. Notably, IC$_{50}$ of Pt-AuSNAs is lower than native cisplatin in all four cell lines tested (Figure 1.26B). IC$_{50}$ of Pt-AuSNAs is less than one-tenth of
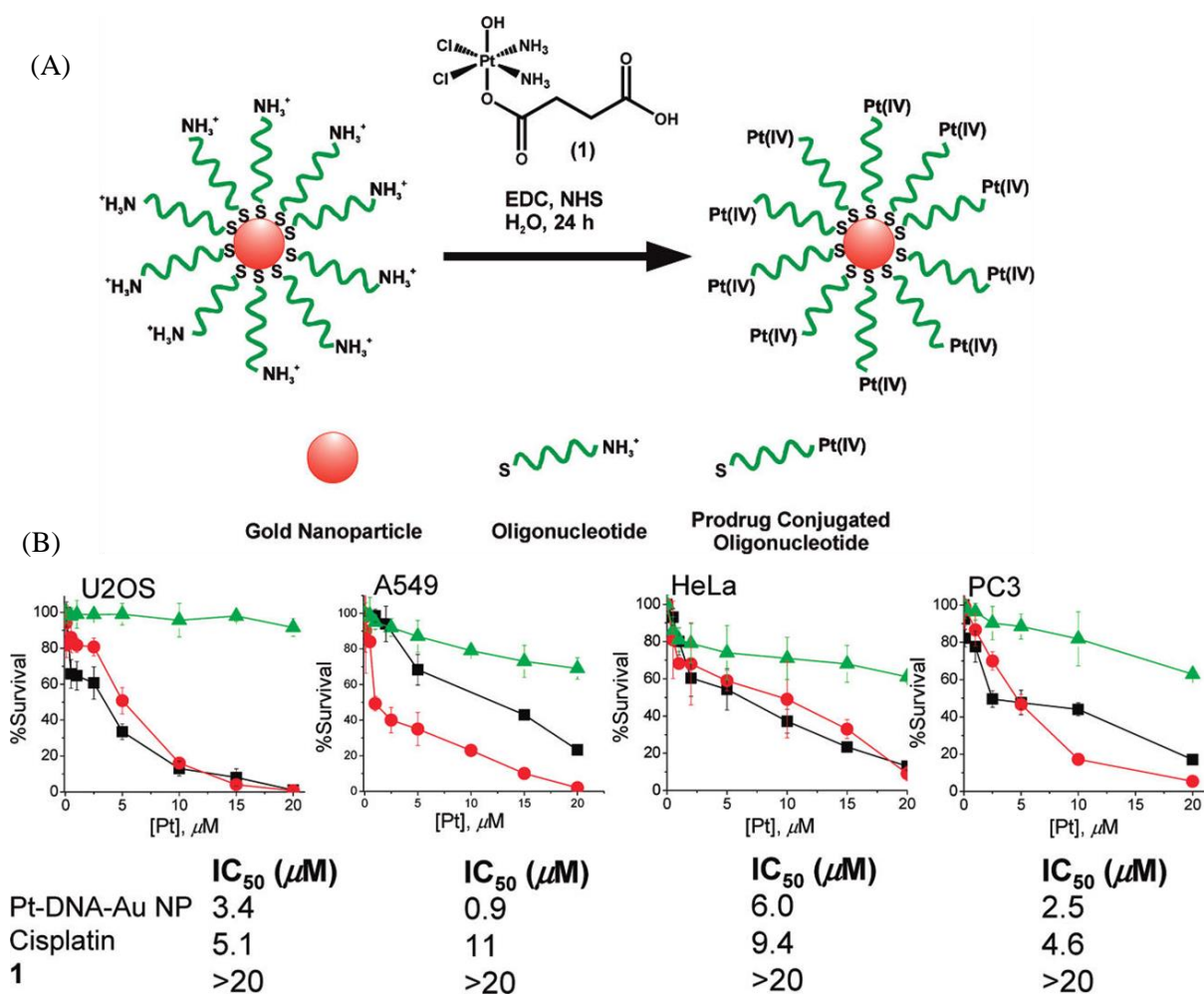
Figure 1.26 Conjugation of cisplatin prodrug, compound 1 to AuSNA and its cytotoxicity in four cancer cell lines. (A) AuSNAs bearing amine-terminated oligonucleotides were covalently attached to compound 1 via EDC coupling. (B) Cytotoxicity of Pt-AuSNAs in four cancer cells compared with native cisplatin and cisplatin prodrug, compound 1.

that of native cisplatin in A549 cells, probably due to the fact that A549 is considered hard to

transfect.

CHAPTER TWO

ATTUNATING ABNORMAL SCARS WITH LIPOSOMAL SNAS AND AUSNAS

2.1   Summary

Scarring is a natural wound closure process. Many incidents that create wounds can lead to scarring, and scar management has been a pressing health issue for the globe[55-58]. In many cases, keloid and hypertrophic scars, resulting from exessive dermal fibroblast proliferation and colleagen fiber deposition, form after wound-creating injuries. These abnormal scars are asthetically unplesant, painful, and pyschologically stressful. While there has been many attempts to develop abnormal treatments, the challenge is that there does not exist a user-friendly abnormal management method that can effectively attenuate abnormal scar formation[59-62].

The molecular mechanism behind abnormal scarring is extremely complicated. Transforming growth factor beta 1 [63-67] (TGFβ1) is a class of cytokines significantly implicated in the abnormal scar formation that can lead to hyperactivity of myofibroblasts. While there has been interest in academia and industry to develop scar management by altering the TGFβ signaling pathway, such efforts are mostly unsuccessful, mainly due to the poor permeability of skin and ineffective manipulation of the TGFβ signaling pathway[61, 68, 69].

Our group has previously shown that AuSNAs can freely enter 100% of keratinocytes, the major epidermal skin cell *in vitro,* within two hours. In additional, topically applied AuSNAs were able to penetrate human skin equivalents and intact mouse skins. Those topically applied AuSNAs were also able to knockdown epidermal growth factor receptor (EGFR)[41] in skin cells after topical treatment.

In this chapter, a non-invasive, SNA-mediated delivery of antisense DNA targeting TGFbeta1 is introduced. AuSNAs and LSNAs capable of knocking down TGFbeta1 *in vitro* were

prepared and characterized. TGFbeta1 knockdown *in vivo* with a rabbit ear hypertrophic scar

model and scar histology analysis will also be discussed in this chapter.

2.2 Introduction

Scar management has evolved into a pressing issue worldwide. Scaring is a part of wound healing process to restore tissue integrity after wound-forming injuries. It is reported that ~7 million people get burn injuries per year and over 232 million surgies are performed world-wide[55, 70], most of which result in scars. Normal scarring in the wound healing process exhibits an elegant balance among fibroblast proliferation, cytokine screction, as well as collegan fiber deposition and degradation. Any genetic predisposition or mismanagement of wound may perturb molecular and signaling pathways in scarring and lead to abnormal scars, including keloid and hypertrophic scars, characterized by exessive secretion of growth factors and collagen fiber deposition. These abnormal scars form frequently after wound-creating injuries, with incidence rates of 91% following burn injuries and 70% after sugeries[55]. Abnormal scars are deeply aesthetically unpleasant, painful, and create psychological stress. Patients seeking scar medication likely make frequent visits to doctor for invasive scar management, resulting in losing vaulable time and expensive medication cost.

Despite the need for advancing scar management, the current abnormal scar management methods are suboptimal. For instance, surgical removal of scars results in a recurrence rate of more than 50%, sometimes with an even larger scar reforming. Injection of corticosteroids is a popular treatment for abnormal scars, which proves effective in certain scerions with cryotherapy or surgery but also accompanies a high recurrence rate (9-50%)[55-57, 64, 71]. More importantly, these treatments are adminstered in an invasive manner that needs the supervision of a medical professional. Silicone or hydrogel sheets have also been utilized for scar care, but in-depth clincal

studies found that these methods could relive the scar pain but were unable to reduce or remove scars.

To develop a user-friendly scar treatment, transdermal delivery of topically applied drugs targeting molecules implicated in abnormla scarring is an attractive route due to its minimized systematic toxicity and potential to be administered by patient themselves. Unforatunately, access to skin has proven a significant challenge and is normally reserved for a limited number of hydrophobic small molecule drugs. For example, penetration of drugs larger than a few hundred daltons into skin has been shown extremely difficult[61]. An alternative approach is to silence genes and proteins implicated in abnormal scar formation via antisense pathways. However, non-invasive skin delivery of oligonucletides posed a challenge due to their large size and susceptibility to nuclease degrdation.

To delivery antisense oligonucleotide through skin, we have previously shown that the spherical nucleic acid (SNA) construct holds great promises. The SNA construct consists of a nanoparticle core with a densely functionalized oligonucleotide shell. SNAs have been shown to resist DNase degradation and have been shown to enter numerous cell lines via receptor-mediated endocytosis. In addition, SNAs are capable of penetrating into mouse skins and human skin equivalent. and are able to suppress gene expression of skin cells[72]. In this work, we hypothesize that two SNA constructs, AuSNAs (SNAs comprised of a Au nanoparticle core) and LSNAs (SNAs comprised of a liposome nanoparticle core) bearing antisense oligonucleotides targeting mRNA encoding growth factor 1 (TGFβ1), a cytokine heavily implicated in the abnormal scarring

process are able to suppress TGFβ1 protein expression level *in vivo* and improve scar histology

with a rabbit ear hypertrophic scar model.

2.3   Results

2.3.1 SNA characterizations

AuSNAs and LSNAs were chosen for the regulation of TGFβ1 expression level because AuSNAs are the prototypical SNA construct that is most-well characterized, and LSNAs comprised of a biocompatible lipid material that exhibits the most promising potential in clinical translation. Antisense oligonucleotides were adapted and modified from published studies and screened for their ability to knockdown TGFβ1 mRNA in rabbit fibroblast (Rab9), human keloid fibroblasts (KF), and human hypertrophic scar fibroblasts (HSF) by qRT-PCR. Sequence No.6 (Appendix 1) was chosen since it shows the most potent downregulation of TGFβ1 mRNA and
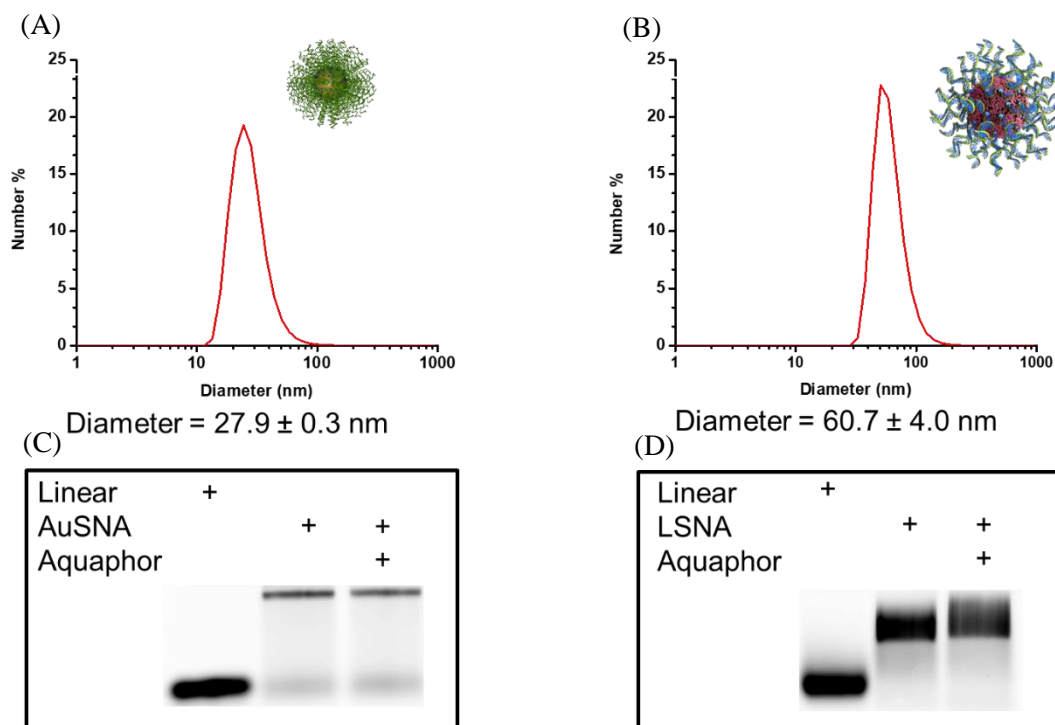
Figure 2.3.1 Characterizations of AuSNAs and LSNAs. (A) hydrodynamic diameter of AuSNAs (B) hydrodynamic diameter of LSNAs (C) agarose gel electrophoresis of AuSNAs mixed with Aquaphor (D) agarose gel electrophoresis of LSNAs mixed with Aquaphor

the fact that this sequence is homologous to both rabbit and human, potentially making clinical translation easier from rabbit ear model to human clinical trials.

AuSNAs and LSNAs bearing the antisense oligonucleotides targeting TGFβ1 were prepared by previously described methods[42, 73]. The hydrodynamic diameter of AuSNAs and LSNAs, determined by dynamic light scattering (DLS) was 27.9 ± 0.3 nm and 60.7 ± 4.0 nm (Figure 2.3.1A), respectively. Each AuSNA and LSNA particle was functionalized with ~168 and ~100 strands of antisense oligonucleotides, determined by UV-vis spectroscopy. To increase the viscosity of the AuSNAs and LSNAs solutions for downstream topical treatment, AuSNAs and LSNAs solutions were mixed 1:1 wt with a commercially available ointment, Aquaphor. To test the structural integrity of AuSNAs and LSNAs mixed with Aquaphor, the SNA and Aquaphor mixtures were incubated at 25ºC for 24 hours and resolved by the agarose gel electrophoresis. Figure 2.3.1B suggests that no extra band or mobility shift has been observed for SNAs mixed with Aquaphor for 24 h, indicating both SNA constructs were structurally stable after mixing with Aquaphor.

2.3.2 Cellular uptake of AuSNAs and LSNAs into normal and scar fibroblasts

One characteristic of SNAs is their ability to freely enter cells via receptor-mediated endocytosis pathway. To evaluate AuSNA uptake into Rab9, HSF, and KF, inductively coupled plasma mass spectrometry (ICP-MS) was employed to quantify the number of AuSNAs associated with these cell lines. As can be seen from (Appendix 2), the amount of AuSNAs uptake into KF and HSF cells are different and shows a time-dependent uptake profile, with uptake into KF cells the most, probably due to different amount of SR-A and caveola expressed by these cells. Figure 2.3.2 demonstrates that Cy3 labeled AuSNAs enter both HSF and Rab9 cells with a punctate distribution pattern, characteristic of cellular uptake via the endocytic pathway.

To evaluate uptake of LSNAs into Rab9, KF, and HSF cells, the oligonucleotide was labelled with Cy5 for fluorescence quantification measured by flow cytometry. Appendix 3A shows that endocytosis of LSNAs into Rab9 cells lasts for at least 24 h and are both concentration and time-dependent. It can be seen from Figure Appendix 3 B and C that free oligonucleotides do not enter
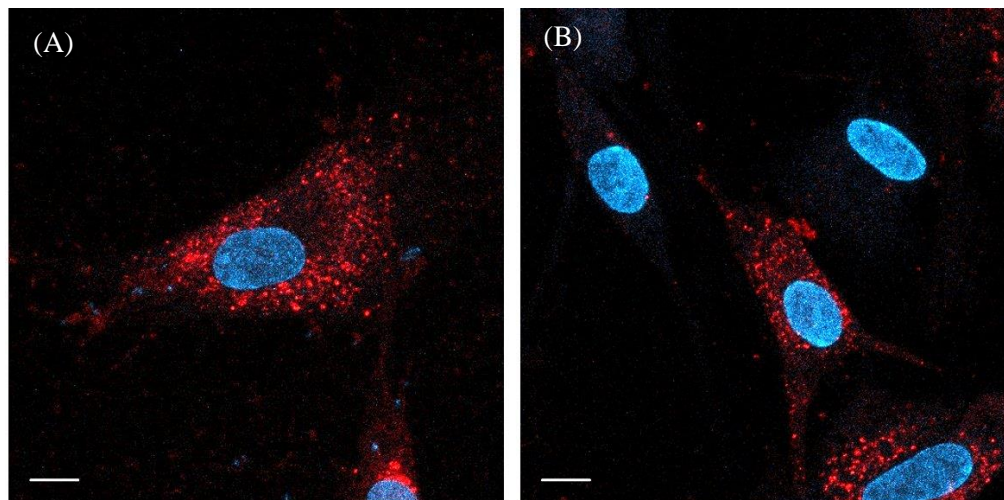
Figure 2.3.2 AuSNAs uptake into HSF cells (A) and Rab9 cells (B). Scale bars = 20 µm

KF and HSF cells while SNAs can enter them freely. This uptake study, along with previously published results from our group, reaffirms our claim that arranging linear oligonucleotides into a three-dimensional structure is essential for rapid cellular uptake into different cell lines.

2.3.3 Downregulation of TGFβ1 protein expression *In Vitro*

After confirming both SNA's structural integrity and ability to enter normal and scar fibroblasts, we tested our hypothesis that both AuSNAs and LSNAs were able to downregulate TGFβ1 *in vitro*. First, Rab9 was incubated with 1.0 µM TGFβ1 AuSNAs and LSNAs (by DNA) at 37ºC for 72 h before the cells were lysed for protein expression analysis. Western blot result (Figure 2.3.3)
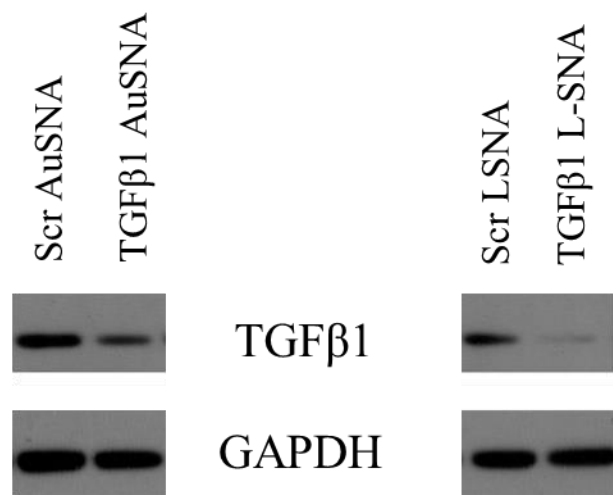
Figure 2.3.3 Regulating TGFβ1 in Rab9 cells by LSNAs and AuSNAs

indicates that both AuSNAs and LSNAs were able to downregulate TGFβ1 expression level in
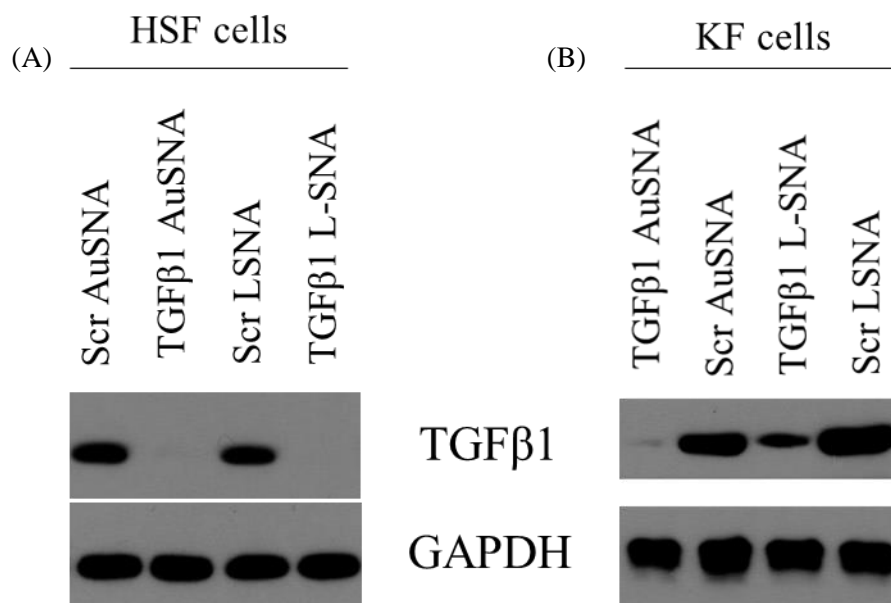
Figure 2.3.4 Regulating TGFβ1 protein expression level in human-derived primary HSF (A) and KF (B) cells.

normal rabbit fibroblasts. Second, human-derived scar primary fibroblasts, HSF and KF, were also treated with TGFβ1 AuSNAs and LSNAs. These two cell lines were tested because they represent the two primary scar phenotypes. Remarkably, both SNA constructs totally abolished TGFβ1 in HSF cells (Figure 2.3.4A). In addition, both AuSNAs and LSNAs were able to suppress TGFβ1 expression in KF (Figure 2.3.4B). Consistent with the knockdown results, TGFβ1 LSNAs were able to inhibit proliferation of Rab9 cells as compared to scrambled LSNAs ($P < 0.01$ at 96 hours, Appendix 4). Since the TGFβ1 targeting sequence was designed to be homologous to both human and rabbit, a specificity control was performed to ensure the knockdown is species specific. Mouse fibroblasts (NIH 3T3) were treated with AuSNAs and LSNAs followed by western blot analysis, and no change in TGFβ1 expression level was observed (Appendix 5). These observations point to the importance of the design rules employed in the sequence design in our SNA construct and prove that these AuSNAs and LSNAs are clinically relevant.

Taken together, the *in vitro* knockdown experiments support our hypothesis that AuSNAs and LSNAs were able to reduce TGFβ1 expression level in a sequence- and species-specific manner via the antisense silencing pathway. Interestingly, the knockdown effect is most pronounced in hypertrophic scar fibroblasts, possibly due more elevated TGFβ1 expression level (Appendix 6), making us confident of our *in vivo* knockdown experiments with a rabbit hypertrophic scar ear model.

2.3.4 Regulating TGFβ1 protein expression *In Vivo* with a hypertrophic rabbit ear model

To evaluate whether these AuSNAs and LSNAs were able to knockdown TGFβ1 protein expression *in vivo* as a topically applied formulation, we chose to investigate the potency of these

Treatment Scheme
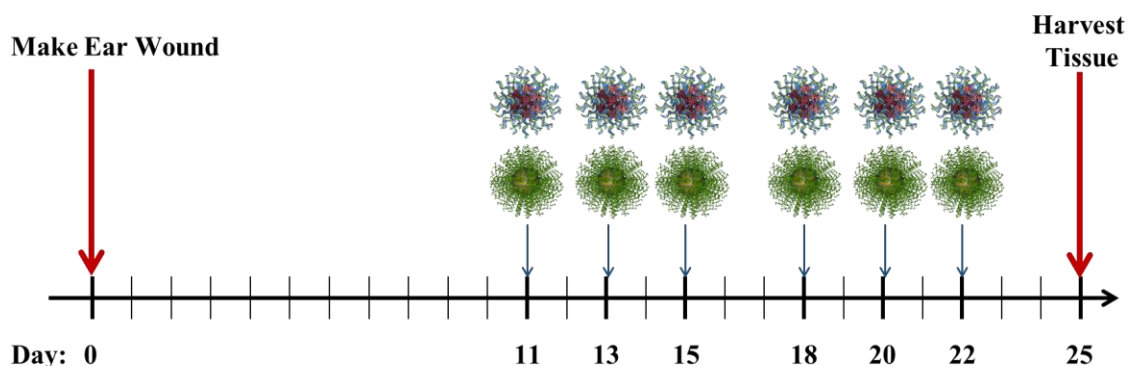
Figure 2.3.5 Treatment scheme of rabbit ear scars.

SNAs regulating TGFβ1 protein in a well-established rabbit ear hypertrophic scar model. Hypertrophic scars were created on the rabbit ear by a well-trained animal medical profession, and rabbits were treated humanely. SNAs (500 nM, 10 µl) were thoroughly mixed with Aquaphor (1:1 wt) and topically applied to the wound sites on the rabbit ear every other day with the first application on day 11 (Figure 2.3.5), when the wound is visibly closed. Rabbits were sacrificed, and scar tissues were harvested and prepared for western blot analysis and histology analysis at day 30.

Figure 2.3.6A is a representative western blot image evaluating TGFβ1 expression with histone (H3) as an internal control. Untreated and vehicle (Aquaphor)-treated rabbit ears did not show noticeable change in TGFβ1 expression level. Both TGFβ1 AuSNA and LSNA treatments were able decrease the TGFβ1 expression level to the similar amount as the unwounded rabbit ear. We note that AuSNAs and LSNAs carrying a scrambled sequence showed protein expression level different than untreated group. We speculate that the non-specific binding is due to the incorporation of three locked nucleic acids into the antisense sequence. To quantify the TGFβ1
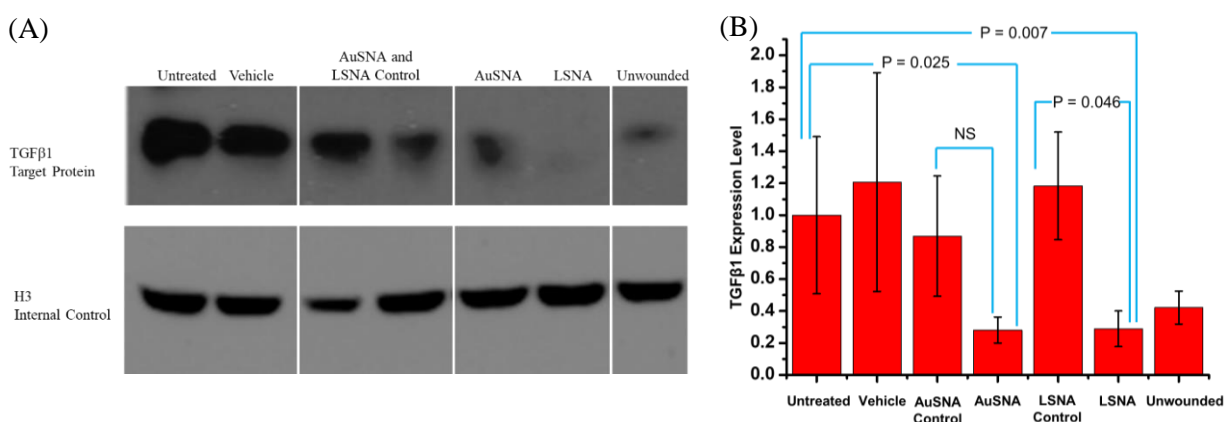
Figure 2.3.6 Assessment of SNAs regulating TGFβ1 expression level *in vivo.* (A) Representative western blot image of various treatment conditions. Upper band: TGFβ1; lower band: histone 3 (H3). (B) Composite protein expression level quantified by ImageJ.

protein level change, all of samples (N=6) were analyzed by western blot followed by band intensity quantified with Image J to derive a composite protein expression statistic. Protein expression level of each treatment group was normalized to the untreated and expressed as average ± standard error of the mean (SEM). As Figure 2.6B shows, both AuSNAs and LSNAs bearing the antisense sequence were able to downregulate TGFβ1 expression level compared to untreated control groups (P = 0.025 and 0.007 for AuSNAs and LSNAs, respectively), returning the TGFβ1

expression level to that of the unwounded, healthy groups. We observed that effect of targeting-AuSNAs and scrambled AuSNAs do not differ significantly despite the obvious difference in their average (more than 80% protein expression for scrambled AuSNAs while less than 30% for targeting AuSNAs).

2.3.5 Downregulation of TGFβ1 protein expression results in scar histology improvement

After confirming our SNA constructs were able to suppress the TGFβ1 protein expression level *in vivo*, we further evaluated whether the reduction of TGFβ1 protein leads to improvement of scar histology. For this purpose, scar elevation index (SEI) was chosen as a quantitative measure of scar histology. Briefly, harvested rabbit ear scar tissues were sectioned into a 5 µm thick slice followed by hematoxylin and eosin stain (H&E staining). H&E staining allows one to visualize cells and collagen by coloring them blue and pink, respectively. The scarring area is normally identified by a dense and circular collagen deposition pattern (Figure 2.3.7A) while the normal healthy tissue is characterized by a one-directional collagen deposition pattern with relatively large space between collagen fiber bundles (Figure 2.3.7B). SEI was measured by first defining the epidermis scarring area and the dermal area beneath it and then taking the ratio between them
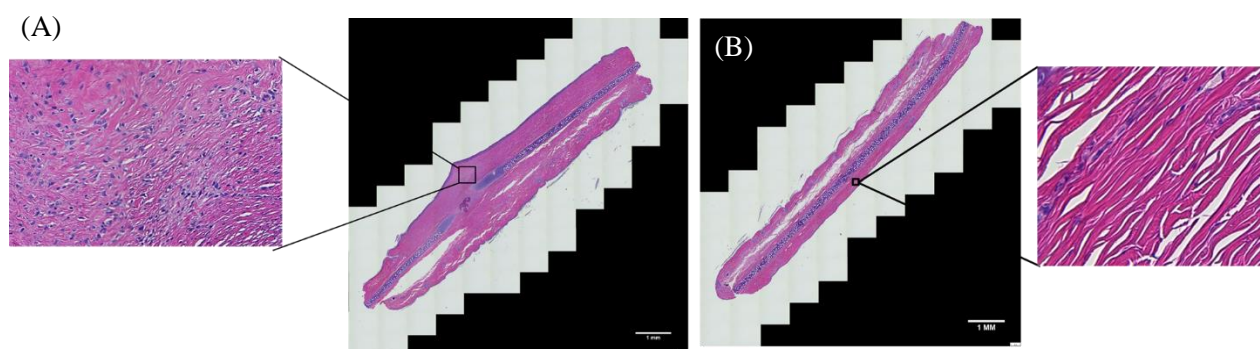
Figure 2.3.7 Representative H & E scar and healthy skin images (A) Zoom-in scarred tissue image (B) Zoom-in healthy skin image.

(A)   (B)
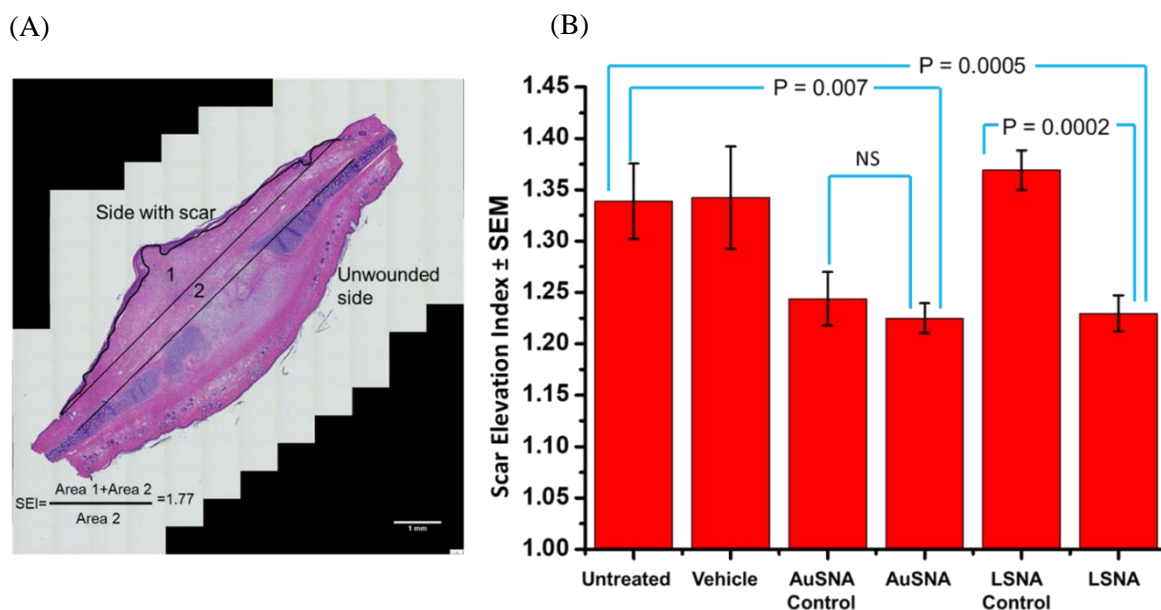
Figure 2.3.8 Scar elevation index (SEI) measurement of scar or healthy rabbit ear tissues. (A) Graphic definition of SEI. (B) Composite SEI of different treatment groups. SEI was expressed as average ± standard error of the mean

(Figure 2.3.8A). For a healthy tissue, SEI equals one. An effective treatment of abnormal scar will be able to decrease SEI compared to untreated group. SEI was calculated as average ± SEM (N=6) for all of rabbit ear samples. Figure 2.3.8B shows that consistent with western blot analysis of TGFβ1 protein expression, both TGFβ1AuSNAs and LSNAs were able to decrease SEI of scarring tissues to ~1.22 from ~1.32 of untreated tissue with P=0.007 for AuSNAs and P=0.0005 for LSNAs, respectively. We note that scrambled AuSNAs were also able to decrease SEI based on our data, an observation consistent with western blot analysis of TGFβ1 protein expression. We speculate that this might be due to the ability of Au nanoparticles to inhibit the growth and proliferation of fibroblasts.[74]

Furthermore, trichrome staining was employed to analyze the change of collagen fiber morphology induced by different treatment conditions. Trichrome staining is a three-color staining
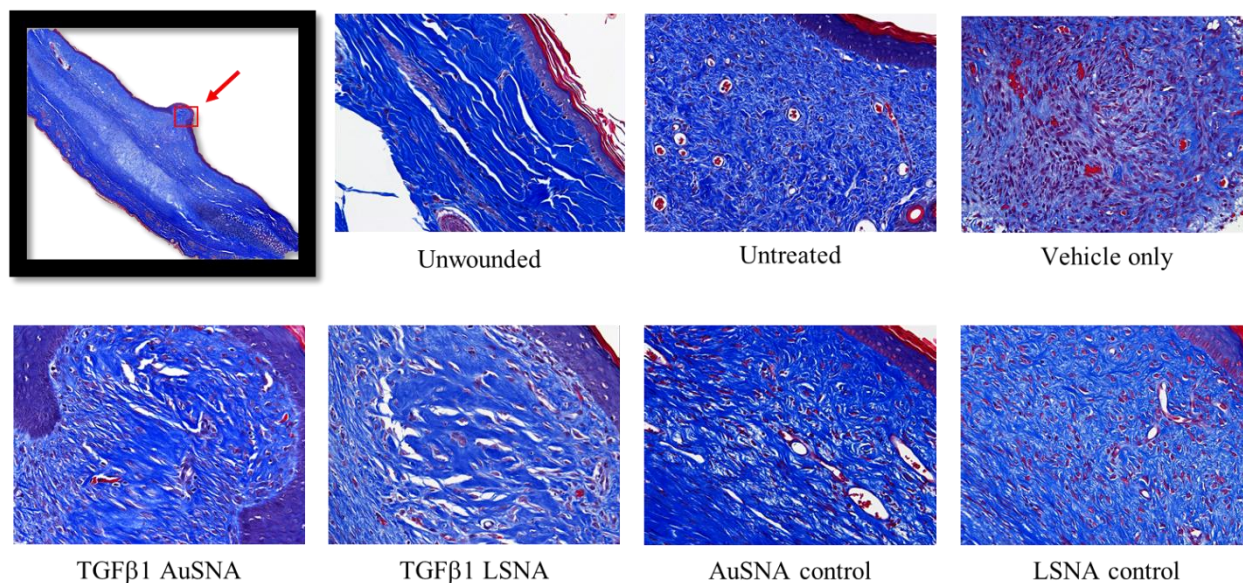
Figure 2.3.9 Masson's trichrome staining of rabbit scar ear tissues with different treatment conditions. Red arrow points to where approximately the zoom-in image was taken.

method that allows for the visualization of collagen fibers. The advantage of trichrome staining is showing enhanced contrast for collagen fibers and its ability to distinguish cells from connective tissues. Briefly, tissue samples were sectioned into 5 µm slices followed by a one-step Masson's trichrome staining protocol. Collagen fibers were stained blue and skin cells, such as keratinocytes, as well as muscle tissues, were stained pink. Figure 2.3.9 is a panel of trichrome staining for different treatment conditions. Qualitatively, untreated scar tissue has extremely dense collagen fiber deposition while healthy tissue has more sparse collagen fiber deposition. The TGFβ1 LSNA- and AuSNA-treated scars have seen a reduction in the local density of collagen fiber deposition and circular orientation of collagen fibers. Taken together, both quantitative and qualitative assessment point to the potential use of SNAs as a topical treatment that enables reduction of abnormal scars.

2.4 Conclusion

Abnormal scar management has posed a significant challenge for the biomedical community. While there exists effective scar treatments, the majority of them need to be administrated by a medical profession in an invasive manner, such as needle injection. This chapter summarizes our efforts to topically deliver anti-TGFβ1 DNA with the AuSNA and LSNA nanoconjugates. Rational design of anti-TGFβ1 homologous to human and rabbit TGFβ1 enables potent silencing *in vitro* in both healthy rabbit fibroblasts and human-derived scar fibroblasts. *In vivo* results indicate that TGFβ1 AuSNAs and LSNAs were able to suppress TGFβ1 in a rabbit ear hypertrophic scar model. Following our observation that both nanoconjugates were able to silence TGFβ1 *in vivo*, we have also observed scar histology improvement, measured by scar elevation index and qualitatively demonstrated by trichome staining.

This work further illustrates the ability of SNA nanoconjugates to penetrate tissues and silence a scar-related gene. This proof-of-concept study could serve as the foundation for treating fibrosis-related diseases such as lung fibrosis or liver fibrosis, given TGFβ1 is significantly implicated in those diseases.

2.5 Experimental methods

Oligonucletiode synthesis: all of oligonucletiodes were synthesized either on a Mermaid 12 Synthesizer or a Applied Bio (ABI). Universal controlled pore glass (CPG) was pruchased from ChemGenes. All other DNA related reagents and thiol-modified CPG were pruchased from Glen Research. After solid-phase synthesis, oligonucletiodes were cleaved from CPG with aqueous ammonium hydroxide (28-30%, Sigma Aldrich) for 16 hours at room temperature or a 1:1 Vol mix of aqueous ammonium hydroxide with methyl ammine for 2 hours at room temperature. Oligonucleotides were purified by reverse phase high performance liquid chromatography (RP-HPLC) with a Microsorb C18 column. After HPLC purification, the molecular weight of oligonucleotides was determined by a matrix-assisted laser desorption/ionization time of flight mass spectrometer (MALDI-TOF) (Bruker). Oligonucleotides used in this study were tableted in (Appendix 6).

AuSNA preparation: 13 nm citrate-capped Au nanoparticles were prepared using the Frens method (ref) that results in a stock of Au nanoparticle solution with a concentration of ~ 10 nM. To prepare control or targeting AuSNAs, 500 molar equivalent of thiol-modified TGFβ1-control or targeting sequences were added to AuSNA solution with 0.1% Tween 20 as a stabilizing surfactant. The mixture was briefly sonicated and shaken for 1 h at 300 r.p.m. Then at each 30 minutes interval, NaCl was added to the solution to increase salt concentration of the solution to 0.05 M, 0.1 M, 0.2 M, 0.3 M, 0.4 M, and 0.5 M. After last NaCl addition, the AuSNAs were washed with a 100KDa Amicon spin filter for 4 times at 5000 g. AuSNAs concentration was determined by a Uv-vis spectrophotometer.

**LSNA preparation*:* liposomal nanoparticle was prepared following a modified freeze-thaw method. Briefly, 1,2-dioleoyl-sn-glycero-3-phosphocholine (DOPC) dissolved in chloroform was purchased from Avanti. 4 mL of 25 mg/ml DOPC was evaporated overnight and resuspended in 1X HEPES-buffered saline (HBS). The DOPC solution was then frozen in liquid nitrogen and then thawed at room temperature for 5 times to break multilamellar vesicles. The resulting liposome solution was then extruded through a 200 nm polycarbonate membrane (T&T Scientific) for 3 times at 0.5 mL/min and 2 mL/min, followed by additional extrusions through a 50 nm membrane for 3 times at 0.5 mL/min and 30 times at 1 mL/min on an automated extruder (Unitronics). To prepare LSNAs, 100 molar equivalents of tocopherol-modified oligonucleotide was incubated with liposomes overnight at room temperature under 500 rpm.

Hydrodynamic size measurement: hydrodynamic diameter of nanoparticles and SNAs were measured by a Zetasizer (Malvern Nano ZS) utilizing dynamic light scattering with a 660 nm laser source. As-synthesized particles were diluted 1:100 with nanopore water before measurement.

Measurement of oligonucleotide loading of AuSNAs and LSNAs: to measure the number of strands chemically attached to Au nanoparticles, AuSNAs were first diluted to 10 nM by Au and then dissolved with equal volume of KCN. The mixture was incubated until AuSNAs were fully dissolved. The A_{260} absorbance of oligonucleotides was measured by a Uv-vis spectrophotometer, and then the concertation of oligonucleotides was determined by Beers' law with extinction coefficients of each oligonucleotide. The number of strands of LSNAs were estimated to be ~100 as no purification was needed.

Stability study of AuSNAs and LSNAs in Aquaphor: Equal weight of Cy3-labeled AuSNAs and LSNAs were mixed with Aquaphor respectively and then incubated for 24 h at room temperature. Equal volume of sample was loaded to a 1% agarose gel and run with 100 V for 20 minutes with 1X TBE buffer. The agarose gels were imaged with a Cy3 laser excited at 550 nm on a gel imager (Typhoon 5).

Confocal microscopy: cells were seeded into a confocal dish and allowed to adhere. They were then treated for fluorescently-tagged DNA SNAs for 12 hours in Opti-MEM media at a 100 nM by fluorescently-tagged DNA. The cells were then washed and subsequently fixed using a 3.7% formaldehyde solution in PBS for 10 minutes. The cells were then stained with a DAPI nuclear stain and finally imaged with confocal microscopy.

Cell culture: Rab9, KF, and HSF cells were cultured with DMEM or MEM Medium supplemented with 10% fetal bovine serum (FBS) and 1% Pen Strep (Invitrogen). Cells were maintained in 37ºC with 5% CO_2.

Extract primary keloid fibroblasts: Fresh patient biopsy was washed well with saline, and incubated with dispase protease overnight at 4ºC to separate dermis from epidermis. Dermis was then washed 3 times with PBS before minced. Minced dermis was then air dried before incubating with 0.05% trypsin/1mM EDTA for 8 hours at 37oC to separate fibroblasts. Separated fibroblasts were allowed to grow in human dermal fibroblast media for about a week before tissue debris was removed and passaged. Fibroblast media was changed every two days to maintain nutrients for extracted fibroblasts.

RNA expression analysis by qRT-PCR: To evaluate TGFβ1 mRNA expression level, Rab9 fibroblasts were seeded into 96-well plates and allowed to adhere overnight. Antisense sequences against

TGFβ1 were added to the cells at a concentration of 1 μM in Opti-MEM and with a transfection reagent. After a 12 hour incubation, the media was changed to MEM with 10% fetal bovine serum and 1% penstrap. To quantify gene expression, total RNA was extracted from cells plated in 96-well plates using the RNeasy 96 well plate kit per the manufacturer's protocol. RNA was subsequently reverse transcribed to generate cDNA using the High-Capacity cDNA reverse Transcription Kit. cDNA was mixed with Roche's Lightcycler 480 Probe Master Mix along with probes and primers (per manufacturer's protocol). GAPDH was used as a housekeeping gene with the primers and probes generated in house using the following sequences: Forward - 5'- CAA GGT CAT CCA TGA CAA CTT TG -3', Reverse - 5'- GGG CCA TCC ACA GTC TTC T -3', Probe – 5' - HEX – ACC ACA GTC CAT GCC ATC ACT GCC A - BHQ1. All other primers/probes were obtained from Life Technologies. qRT-PCR was performed on a Roche Lightcycler 480 and the relative abundance of each mRNA transcript was normalized to GAPDH expression.

Animal experiments: New Zealand white rabbits were used for this study. Four, 7 mm punch wounds were made on the front of each rabbit ear. The wounds extended down to the cartilage of the ear. The wounds were allowed to heal for approximately two weeks, or until all of the wounds were closed. After the wounds were closed, the resulting scars were topically treated with 20 μL of a 500 nM SNA-in-Aquaphor mixture (1:1 wt). There were 8 experimental conditions in total, and each rabbit had a scar which was treated with one of those conditions. This treatment was repeated three times a week for six weeks. After completion of treatment, the rabbits were sacrificed, and the treated scars were punched out of each ear. An additional punch was taken from an unscarred region of each ear to represent the untreated group. The punch biopsies were then cut into near semi-circles, with one half a bit larger than the other in order to include the entire scar

center. The half with the scar center was formalin fixed and paraffin embedded (FFPE) in order to be used for subsequent histological analysis. The other portion was lysed in order to perform subsequent Western blot analysis.

Scar elevation index (SEI) measurement: Harvested scar tissues were sectioned into 5 µm slice at the Northwestern Mouse Histology and Phenotyping Laboratory, followed by H&E staining. H&E stained tissue samples were embedded onto a glass slide. Light microscopy image was taken using a fluorescent microscope (Leica DM6B Widefield) with 10X magnification. Determination of scar area was performed under the supervision of two dermatology doctors from Northwestern in Image J.

Trichrome staining and imaging: Harvested scar tissues were sectioned into 5 µm slice at the Northwestern Mouse Histology and Phenotyping Laboratory, followed by trichrome staining. Trichrome-stained tissue samples were embedded onto a glass slide. Light microscopy image was taken using a fluorescent microscope (Leica DM6B Widefield) with 10X magnification.

Western blotting to evaluate protein expression *In Vitro*: Fibroblast cells were treated with or without various nanoparticles or their relative controls for 72 hrs before lysed in RAPI buffer. The concentration of total protein of the lysates was determined by Pierce BCA protein assay kit (Thermo Scientific). 120 µg total protein of the whole cell lysates from each treatment condition was loaded onto 10% SDS-PAGE mini-gel, transferred onto the nitrocellulose membrane, and probed with anti-TGF□1 antibody (AbCam), CTGF (AbCam), or collagen I (AbCam). GAPDH antibody (Abcam) was used to ensure the equal loading of total protein from each group.

Western blotting to evaluate protein expression *In Vivo:* Rabbit ear tissues were lysed in RAPI buffer and further disrupted by a tissue homogenizer (Omni International) with ceramic beads (Omni International, 1.4 mm Ceramic) for 20 minutes, twice. The concentration of total protein of the whole tissue lysates was determined by Pierce BCA protein assay kit (Thermo Scientific). 50 µg total protein of the whole cell lysates from each treatment condition was loaded onto 10% SDS-PAGE mini-gel, transferred onto the nitrocellulose membrane, and probed with anti-TGFβ1 antibody (AbCam), CTGF (AbCam), or SMA (AbCam). Anti-H3 antibody (Abcam) was used to ensure the equal loading of total protein from each group.

CHAPTER THREE

PLGA SPHERICAL NUCLEIC ACIDS

3.1 Summary

AuSNAs and LSNAs have been demonstrated for their applications in gene regulation and immunomodulation in various animal models. In the previous chapter, I have shown again that AuSNAs and LSNAs can be utilized as an intracellular gene regulator to silence a key gene involved in abnormal scar formation. LSNAs are currently the most clinically advanced SNA constructs due to biocompatibility of lipid materials.

To further leverage the unique biochemical properties of the SNA construct, one must ask fundamental questions as to how SNAs, especially how the oligonucleotide shell defining the SNA, behave in a physiologically relevant environment. This question is very important since most SNAs' properties origin from the three-dimensional oligonucleotide shell. The interaction between oligonucleotide shell and proteins dictate how long the shell can remain intact, which will in turn determine the time scale during which an SNA can will possess SNA-like properties.

To this end, lipid-based nanoparticles have been shown to be rather dynamic in protein rich environments. Indeed, studies on the stability of LSNAs suggest that the oligonucleotide shell that defines LSNA falls apart very rapidly, with a half-life of only a few minutes. While a dynamic construct may have its own advantages in certain scenarios, it poses great challenge in studying how biological systems interact with the construct. The second challenge that LSNAs face is the difficulty with which a hydrophobic drug can be encapsulated inside the liposome due to the aqueous core of liposomal nanoparticle.

This chapter details efforts to prepare and characterize a class of novel SNAs comprised of a biodegradable and biocompatible polymer, poly(lactic-co-glycolic) (PLGA). The properties of

PLGA-SNAs will be discussed and the stability of the oligonucleotide shell residing on PLGA

nanoparticles will be compared to LSNAs in a protein rich environment.

3.2 Introduction

Gene regulation via the RNA interference (RNAi) or antisense pathways has hold great promise to silence disease-related genes[6]. In principal, any mRNA substrates could be downregulated by small interference RNA (siRNA) or antisense oligonucleotide following the Watson and Crick base pairing with certain design rules[4, 5, 44, 45]. The ability of oligonucleotides to selectively bind to specific mRNA substrates greatly expands disease targets that can be potentially abolished, including targets previously deemed undruggable by traditional small molecule drugs and protein therapeutics. Unfortunately, intracellular delivery of oligonucleotides across cell membranes has proven a challenging task[75]. The negatively charged oligonucleotide backbone generates unfavorable electrostatic repulsion with cell membranes, and the relatively large size of oligonucleotides impedes diffusion-based transport across cellular membranes. In short, naked, linear oligonucleotides do not enter cells without lipid or polymeric transfection agents, most of which proves to be very toxic.

Spherical nucleic acids (SNAs) are a class of synthetic biomaterials consisted of a nanoparticle core with a shell of densely functionalized oligonucleotides. Despite their highly negatively charged surface and large size, the three-dimensional oligonucleotide shell that defines SNA can engage scavenger receptors A (SR-A) and be endocytosed via endosomal pathways. The three-dimensional oligonucleotide shell not only serve as a transport binder to SR-A, but can also be a functional unit inside the cells. Indeed, SNAs have been shown capable of potent gene regulation via both RNAi and antisense pathways. Recently, our group has also demonstrated that

SNAs were able to engage with Toll-like receptors (TLRs) residing inside endosomes that were able to stimulate immune response.

One important characteristic of SNAs is that the nanoparticle cores are compositionally tunable. Since the introduction of SNA in 1996, SNAs comprised of inorganic cores (Au, QD, silica) have been prepared. To further design clinically relevant SNA constructs, one would want a nanoparticle core made from biodegradable materials that has a track record of being FDA-approved. To this end, liposomal SNAs comprised of an organic liposomal nanoparticle core has been prepared. They have shown to enter cells and silence gene of interest, such as HER2 and TGFβ1 demonstrated in the previous chapters of this thesis. However, to further enrich the properties of the SNA construct, LSNAs face a few intrinsic limitations. First, lipid-based nanoparticles are structurally dynamic especially in a protein rich environment[76]. Indeed, studies on the stability of LSNAs suggests that their half-life in 10% fetal bovine serum is only a few minutes[76]. This potentially makes LSNA lose its unique structures and functions in systematic use. Second, it is challenging to encapsulate a hydrophobic drug inside liposomes due to the aqueous core residing inside liposome nanoparticles[77]. Third, the drug release profile of liposome is generally considered hard to control and difficult to tune.

With the goal to address these challenges and to further enrich the properties of the SNA construct, a biodegradable, biocompatible polyester, PLGA, was utilized to form the nanoparticle core for this new class of SNAs. PLGA was chosen to be the base materials for SNA because (i) it can decompose into lactide acid and glycolide acid that are metabolized by human body[78-80] and has a successful history of being FDA-approved sutures[81-86], biodegradable implants, and

microparticles (ii) it has a T_g above 37ºC[87-89], making the polymer chain movement rather limited under physiological conditions and potentially a more stable construct, and (iii) PLGA has been demonstrated capable of delivering hydrophobic small molecule and macromolecule drugs with tunable release kinetics[90-92].

In this chapter, I will demonstrate a facile preparation method for synthesizing PLGA-SNAs. We hypothesize that PLGA-SNAs exhibit biochemical properties diagnostic of the SNA construct, with the added benefit of being a more stable biodegradable structure with tunable drug release profiles. This chapter also serves as a transition to my next chapter, which will further build on some of the properties unique to PLGA-SNAs, such as co-delivery of drugs and tunable controlled release of encapsulated therapeutic agents.

3.3 Results

3.3.1 PLGA-SNA preparation and characterization

PLGA nanoparticles were prepared by a modified nanoprecipitation method (Figure 3.3.1). Briefly, 12.5 mg mixture of PLGA (10 mg)/PLGA-PEG-N$_3$ (2.5 mg) was dissolved in 5 mL acetonitrile. PLGA-PEG-N$_3$ polymer was utilized for downstream DNA functionalization. The mixture was added dropwise to a beaker containing 20 mL nanopure water. The PLGA-PEG-N$_3$ nanoparticles were formed under a nucleation growth process termed nanoprecipitation[91, 93-95]. Mechanistically, supersaturate PLGA droplets form after acetonitrile gets into contact with water. Nucleation growth occurs for the locally concentrated, supersaturated PLGA to gain thermodynamic stability. It can be seen from (Appendix 7) that PLGA nanoparticles with different

Figure 3.3.1. Preparation of PLGA-PEG-N$_3$ nanoparticles and PLGA-SNAs via nanoprecipitation and copper-free click chemistry

Figure 3.3.2 Dynamic light scattering (DLS) measurement of as-prepared PLGA-PEG-N3 nanoparticles and PLGA-SNAs.

sizes can be prepared by adjusting the polymer concentration and the type of solvent. 50 nm PLGA nanoparticles were the desired diameter due to their ability to penetrate the tumor environment and ability to enter cells[96].

The nanoparticles were concentrated using an Amicon spin filter unit (size cutoff = 100 K) followed by sizing with dynamic light scattering (DLS) and atomic force microscopy (AFM). DLS shows that as-prepared PLGA-PEG-N_3 nanoparticles have a hydrodynamic diameter of ~50 nm. (Figure 3.3.2). The nanoparticle concentration was then determined by a Nanoparticle Tracking Analysis (NTA) system. Based on the nanoparticle concentration, the surface azide can be approximated by a method described by Zhang *et al* [97]. To convert PLGA-PEG-N3 nanoparticles to PLGA-SNAs, strands of oligonucleotides terminated with dibenzocyclooctyne (DBCO) was

added to PLGA-PEG-N$_3$ nanoparticles and incubated for 72 h at 25ºC via copper-free click

chemistry due to its fast kinetics and biorthogonal reactivity. After 72 h, unreacted

oligonucleotides were washed away by passing them through an Amicon Filter unit with a size

cutoff of 100 K. PLGA-SNAs were analyzed by 1% agarose gel electrophoresis (Appendix 8).

PLGA-SNAs and linear DBCO-DNA exhibits different electrophoretic mobility due to their

different size and charge. DLS measurement (Figure 3.3.2) of purified PLGA-SNAs indicates a 15

nm size shift larger than the unfunctionalized PLGA-PEG-N$_3$ nanoparticles, a size consistent with

a 20-mer oligonucleotides. Furthermore, the size of PLGA-SNAs was measured by AFM, which
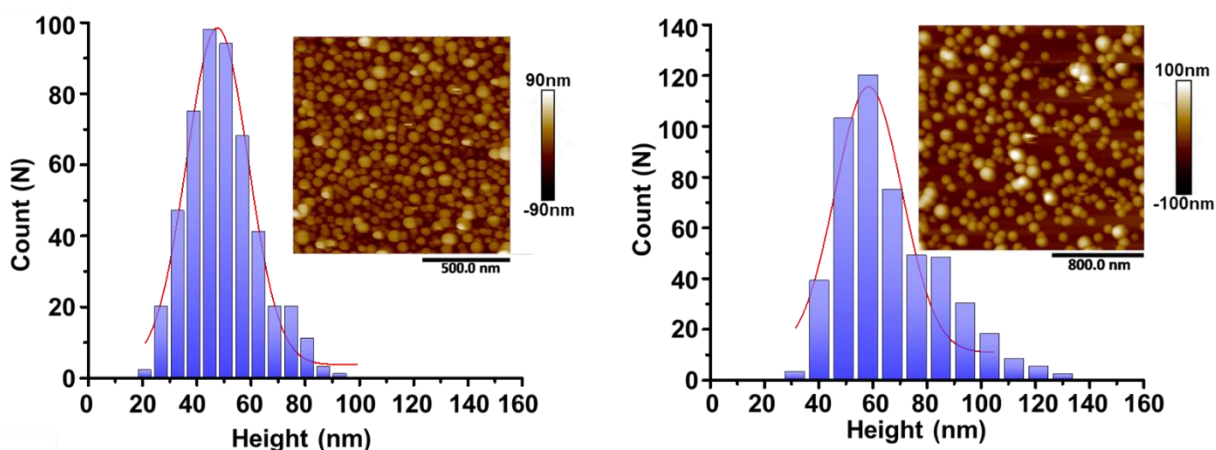
Figure 3.3.3 AFM image and size distribution of PLGA-PEG-N$_3$ nanoparticles and PLGA-SNAs

provides quantitative size distribution. Compared to unfunctionalized PLGA-PEG-N$_3$

nanoparticles, PLGA-SNAs imaged by AFM show a similar size shift as DLS, further suggesting

surface functionalization is successful (Figure 3.3.3).

Surface loading of oligonucleotides dictates many SNAs' biochemical properties, so being

able to quantify the number of strands per particle is essential to predicting the properties of PLGA-

SNAs. To determine surface loading of PLGA-SNAs, a batch of PLGA-SNAs were prepared with

Cy5-labeled T_{20} oligonucleotides. After purification, 20 µl PLGA-SNAs were first freeze-dried and then fully dissolved in NaOH. The oligonucleotide concentration can then be measured by fluorescence microscopy. The nanoparticle concentration can be determined by a Nanoparticle Tracking Analysis system (NTA). Each 65 nm PLGA-SNA has ~200 oligonucleotide strands, resulting in a surface density of 5.2 pmole/cm^2. Comparing with other SNA constructs, this surface loading is smaller than AuSNAs (~30 pmole/cm^2) but greater than the most clinically advanced liposomal SNAs (LSNAs, ~3.2 pmole/cm^2).

3.3.2 Structure-property relationships of PLGA-SNA

One advantage of utilizing PLGA as the core for the SNA construct is being able to control the release of therapeutic agents encapsulated inside. Indeed, studies in other groups have shown that co-delivery of chemotherapy agents with nucleic acids has been shown to increase therapeutic efficacy[98]. However, encapsulating both hydrophobic and hydrophilic drugs in one nanoparticle often leads to poor drug-loading efficiency[99], complicated preparation processes[91], and an increase in nanoparticle size[100]. The PLGA-SNA construct provides the benefits of spatially compartmentalizing a chemotherapy drug and therapeutic oligonucleotides in one entity, so the
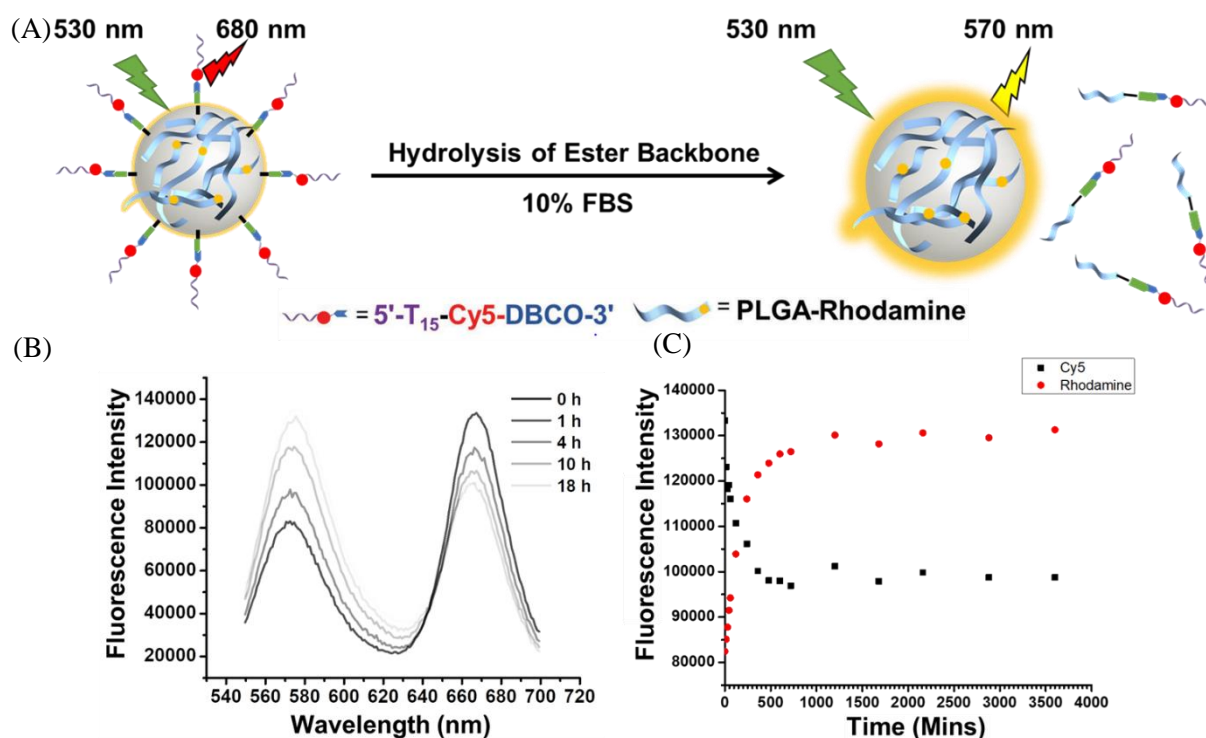
Figure 3.3.4 Schematic of release of oligonucleotide shell that results in changes in FRET signal. (A) Cartoon image showing the preparation of FRET PLGA-SNAs. (B) Rhodamine and Cy5 fluorescence as a function of time. (C) Kinetics of FRET signal changes over time for monitored as Rhodamine and Cy5 fluorescence

loading and drug release profile of nucleic acids and encapsulated drugs can be independently tuned. We hypothesize that the drug release profiles of encapsulated drugs can be adjusted by changing the chemical composition of PLGA, but the degradation of the oligonucleotide shell that defines SNA would remain relatively consistent for different formulations.

To test this hypothesis, Förster resonance energy transfer (FRET) PLGA-SNAs with rhodamine-labelled PLGA and Cy5-labeled oligonucleotide (Figure 3.3.4A) were prepared to investigate the oligonucleotide shell degradation in a protein rich environment. Three batches of FRET PLGA-SNAs, comprised of PLGA with different chemical compositions and molecular weight (Figure 3.3.6), were incubated in 10% fetal bovine serum (FBS). The solution of FRET PLGA-SNAs were excited at rhodamine excitation wavelength (λ_{ex} = 530 nm), and emission from rhodamine and Cy5 was monitored from 550 nm to 700 nm. When oligonucleotides were released from nanoparticle surface, the rhodamine fluorescence (λ_{em} = 573 nm) increased while Cy5 (λ_{em} =
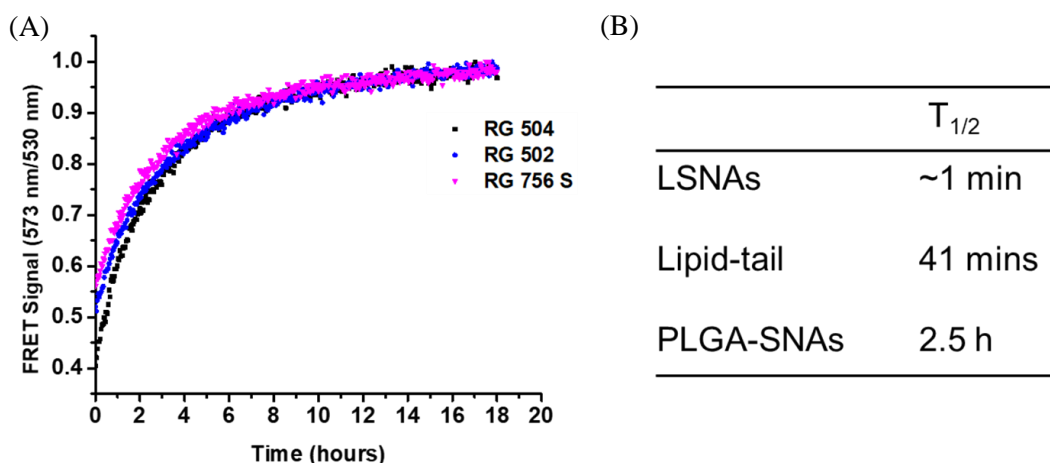
Figure 3.3.5 Kinetics of release of oligonucleotide shell of PLGA-SNAs as compared to other SNA constructs (A) PLGA-SNA oligonucleotide release as a function of different PLGA polymer (B) Comparison between PLGA-SNAs and other SNA constructs

Formulation	PLA:PGA	M.W (Da)	Terminal Capping	K_{obs} [s^{-1}]	Half-life [95% Confidence Interval, h]
RG 502	50:50	7000-17000	Ester	$(7.4 \pm 0.1) \times 10^{-5}$	2.6 – 2.7
RG 504	50:50	38000-54000	Ester	$(8.8 \pm 0.1) \times 10^{-5}$	2.1 – 2.2
RG 756 S	25:75	76000-115000	Ester	$(8.3 \pm 0.1) \times 10^{-5}$	2.3 – 2.4

Figure 3.3.6 Chemical compositions and degradation parameters of three PLGA-SNAs formulations synthesized

670 nm decreased) (Figure 3.3.4B). The release profiles of all three PLGA-SNAs were similar (Figure 3.3.5A); fitting the data to a first-order kinetics indicate that PLGA-SNAs exhibit half-lives of more than 2 h and K_{obs} ranging from 7.4×10^{-5} to 8.8×10^{-5} s^{-1} (Figure 3.3.5B and Figure 3.3.6). These parameters suggest that PLGA-SNAs are almost 100-fold more stable than the most clinically advanced LSNAs and three times more stable than the lipid-tail SNAs[76]. The increased stability is likely due to covalent bond that grafts DNA to PLGA surface and intrinsically higher stability of polymeric nanoparticles compared to liposomes. The nuclease resistance of oligonucleotide shell on PLGA nanoparticle has been compared to that of linear DNA. Consistent with our previous observation[101], PLGA-SNAs show enhanced nuclease resistance against DNase I. Figure 3.3.7 shows nucleic staining of intact SNA or linear DNA after incubation with DNase I for 15, 30, and 120 minutes. It can be seen that there is much more intact SNA band left than linear DNA, quantified with the band intensity located on the bottom of the gel. This might be due high local salt concentration surrounding the SNA particles that potentially deactivates the enzymatic activity of DNase I. The enhanced stability of oligonucleotide shell is likely to make this construct more advantageous in certain situations, potentially improving therapeutic efficacy in systematic use.
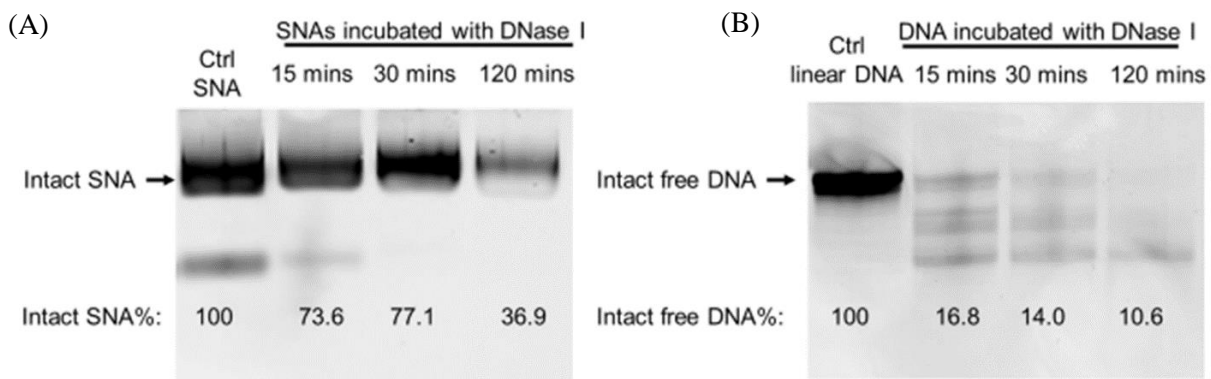
Figure 3.3.7 Comparison of stability of oligonucleotide on the PLGA nanoparticle surface to that of linear DNA. Intact oligonucleotides were stained with SYBR Gold and band intensity was quantified with Image J. (A) Degradation of PLGA-SNAs incubated with DNase I over 2 h. (B) Degradation of linear DNA incubated with DNase I over 2 h.

Next, we investigated the drug release from PLGA-SNAs by utilizing coumarin 6 as a fluorescent model drug. To encapsulate coumarin 6 into PGLA-SNAs, 0.5% (w/w) coumarin 6 was co-dissolved with PLGA in acetonitrile, and the mixture was dropwise added into water to form PLGA-PEG-N_3 nanoparticles that encapsulate coumarin 6. The drug encapsulated nanoparticles were converted to PLGA-SNAs via the procedure described above. The percent release of coumarin 6 is determined relative to the initial amount loaded. (Figure 3.3.8) shows differential release coumarin 6 from three formulations, with RG502 having the fastest release kinetics due to smaller molecular weight[88, 102-104]. So far, we have seen there is a significant difference in drug release for different PLGA-SNA formulations while the differences in the release of oligonucleotide shell is marginal. This points to different release mechanism concerning the encapsulated drugs and oligonucleotide shell: the drug release is a complicated process that involves diffusion, ester backbone hydrolysis, and bulk erosion and surface erosion, giving rise to different

(A)

10% FBS

• = **Coumarin 6**

(B)
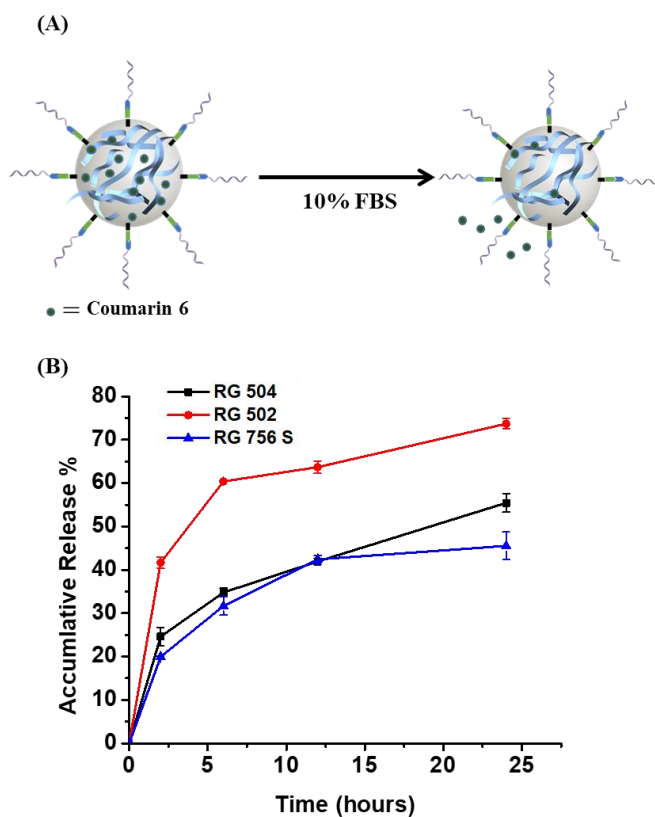
Figure 3.3.8 Drug release of coumarin 6 from PLGA-SNAs. (A) schematic of release of coumarin 6 from PLGA-SNAs in serum containing environment. (B) Release profile of PLGA-SNAs prepared from three formulations

degradation kinetics and release profiles by changing the PLGA chemical compositions. On the other hand, the oligonucleotide release is uniform for each formulation since the chemistry utilized to attach nucleic acid to the nanoparticle surface is identical. This result suggests that the governing mechanism for oligonucleotide release is by hydrolysis of the PLGA ester backbone.

3.3.3 Intracellular functions of PLGA-SNAs

To evaluate the potential of PLGA-SNA as a therapeutic formulation, we prepared PLGA-SNAs with Cy5-labeled T_{20} and quantified their cellular uptake in a Raw-Blue macrophage reporter cell line. Consistent with other SNA constructs, PLGA-SNAs enter these macrophages without transfection agent (Figure 3.3.9). After PLGA-SNAs were endocytosed, they exhibited a concentration- and time-dependent uptake profile. Noticeably, PLGA-SNAs enter cells much more efficiently than their phosphorothioate (PS) backbone-modified linear counterpart, especially at early time points. This indicates the rapid cellular uptake kinetics of the SNA construct as compared to linear strands, especially at early time points. Phosphorothioate (PS) backbone-modified CpG was utilized in this because they exhibit nuclease resistance and potentially more potential binding to receptors.

(A)

(B)
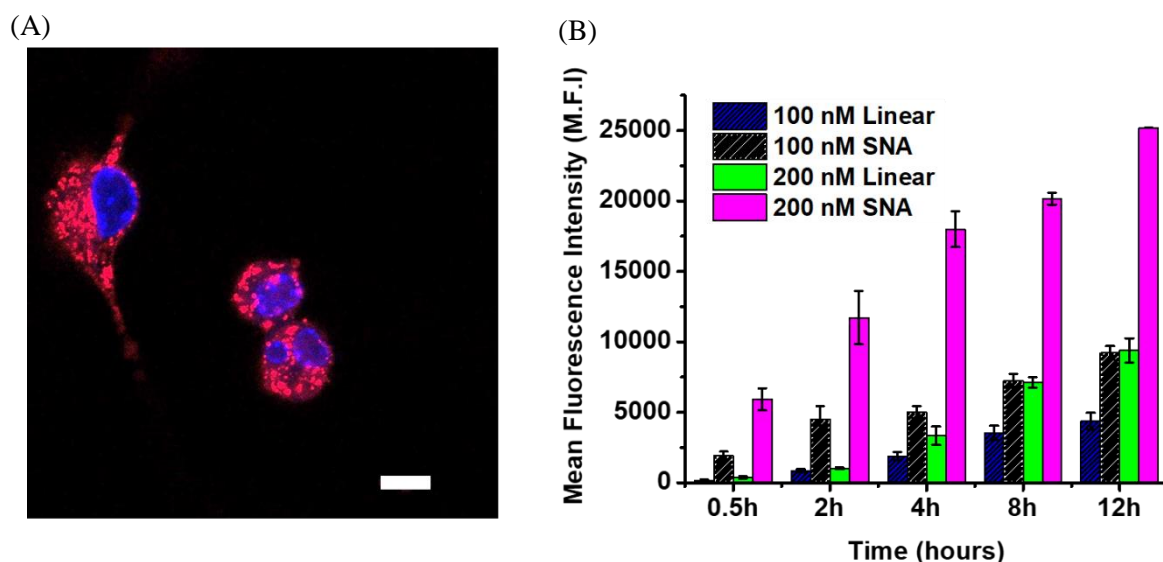
Figure 3.3.9 Cellular uptake Cy5-labeled PLGA-SNAs into Raw-Blue macrophages. (A) Confocal image of PLGA-SNAs inside Raw-Blue macrophages. Red: Cy5 labelled oligonucleotide; blue: DAPI stained nucleus. Scale bar = 10 µm (B) Quantify cellular uptake by flow cytometry.

After confirming the cellular uptake of PLGA-SNAs, we further evaluated the therapeutic function of PLGA-SNAs bearing a CpG motif capable of engaging endosomal TLRs. The activation of TLR9 in Raw-Blue macrophages leads to NF-κB activation. This process results in secretion of secreted embryonic alkaline phosphatase (SEAP) that can be colorimetrically by a Quanti-blue assay. Figure 3.3.10 shows that activation of TLR by PLGA-SNAs is sequence- and concentration-dependent manner. The efficacy of PLGA-SNAs outperformed linear PS CpG, probably due to superior cellular uptake of the SNA construct. Note that PS oligonucleotide is a class of drugs with a successful record of being FDA-approved, so outperforming PS oligonucleotide provides confidence for the clinical prospect of this construct. This class of new SNA constructs are non-toxic over a wide range of concentration (Appendix 9), supporting our hypothesis that SNAs comprised of benign, biodegradable, biocompatible materials such as PLGA will be clinically relevant and more friendly towards medical translation.
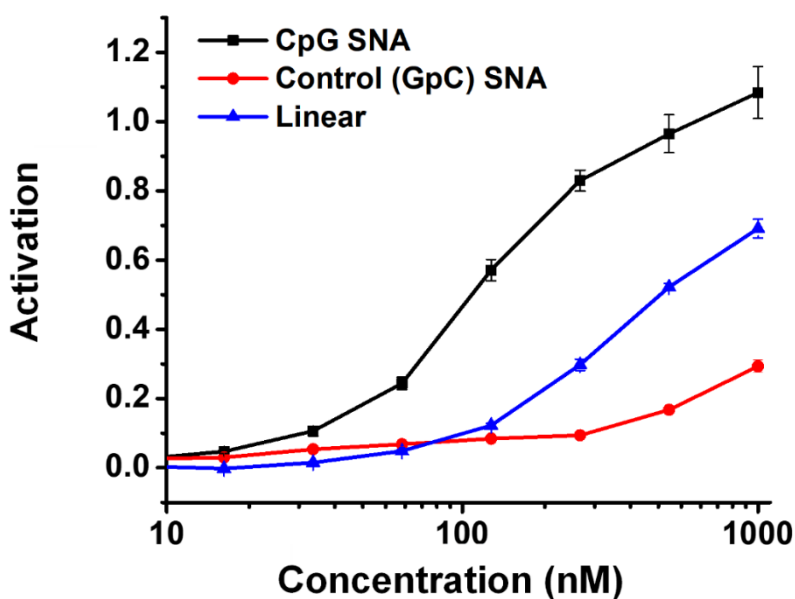
Figure 3.3.10 Activation of TLR9 in Raw-Blue macrophages by PLGA-SNAs bearing a CpG motif. secreted embryonic alkaline phosphatase (SEAP) was quantified by a Quanti-blue assay.

3.4 Conclusion

The premise of the SNA construct offering an improved therapeutic outcome relies on the three-dimensional oligonucleotide shell that defines an SNA. The oligonucleotide shell has been shown responsible for SNAs' rapid cellular uptake and resistance to nuclease degradation. One challenge that most clinically advanced SNA construct, liposomal SNAs (LSNAs) has been facing, is their intrinsic dynamic nature. In 10% serum containing medium, the oligonucleotide shell of LSNAs falls apart within minutes. The loss of oligonucleotide shell potentially causes loss of those unique biochemical properties characteristic of SNAs. While Meckes *et al* have demonstrated an alternative strategy for improving the stability of LSNAs, there is more room more increasing the stability of LSNAs.

Inspired by a diverse chemical composition of the polymeric materials, I have chosen to create a class of novel SNAs comprised of benign, biocompatible, and biodegradable polymer nanoparticle cores. PLGA was chosen for this purpose due to its successful track record of being utilized as biomedical devices and a T_g above physiological temperature, which suggest the chain movement of the polymer nanoparticle is limited. Indeed, the stability of the oligonucleotide shell of PLGA-SNAs exhibit a half-life that is 100-fold longer than LSNAs, with added benefits such as controlled drug release of the encapsulated therapeutic agents. It turns out that the release profile of the encapsulated drugs can be independently controlled by varying the molecular weight of PLGA, while the release profile of the oligonucleotide shell remains the same for different formulations. This provides an additional handle for synergizing the therapeutic windows of the encapsulated cargo with the conjugated nucleic acids.

In addition, it is important to compare core compositions, attachment chemistries, and surface loading across different SNA constructs and relate their functions to their structure. A few SNA constructs comprised of biocompatible materials have been chosen for such a comparison to inform future SNA design (Appendix 10).

3.5 Experimental methods

Oligonucleotide synthesis: Oligonucleotides were synthesized on solid-phase DNA synthesizer (Applied Biosystems) according to manufacture's recommendations. Universal controlled glass pore (CPG) was purchased from ChemGenes. All other special phosphonamidites and reagents were purchased from Glen Research.

Oligonucleotide purification: as-synthesized oligonucleotides were cleaved from CPG support by incubating with 2 mL ammonium hydroxide solution for 16 h at room temperature. The solution containing oligonucleotides was air-dried using a nitrogen gun and filtered. The solution was then injected into a reverse-phased high performance liquid chromatography (RP-HPLC) with a Microsorb C18 column (Agilent Technologies). The oligonucleotides were purified by running a mobile phase (buffer A: 3% triethylammonium acetate (v/v)/ buffer B: acetonitrile) at 15 mL/minutes ramping from 100% A. The purified oligonucleotides were then analyzed by Matrix Assisted Laser Desorption/Ionization Time-of-Flight mass spectrometer (MALDI-TOF).

PLGA-PEG-N$_3$ nanoparticle preparation: PLGA-PEG-N$_3$ nanoparticles were prepared by a modified nanoprecipitation method. 10 mg PLGA (Sigma-Aldrich) and 2.5 mg Poly(lactide-co-glycolide)-b-Poly(ethylene glycol)-Azide copolymer (PLGA-PEG-N$_3$, MW ~ 30,000:5,000 Da; Akina AI091) was dissolved in acetonitrile. The mixture was added dropwise into a beaker containing 20 mL nanopore water under rapid stirring to initiate the precipitation process. The nanoparticle solution was the stirred for 3 h to allow the evaporation of acetonitrile. The nanoparticle solution was then concentrated by using an Amicon filter unit (size cutoff = 100 K) at a spin speed of 800 g for 15 minutes.

PLGA-SNAs surface functionalization: the concentration of as-prepared PLGA-PEG-N$_3$ nanoparticles was analyzed by a Nanoparticle Tracking System (NTA). PLGA-PEG-N$_3$ nanoparticles were diluted 1:15000 and 1:30000 in nanopore water and injected to NTA by an automated syringe pump. NTA measurement was performed as a duplicate with a 633 nm laser, and PLGA-PEG-N$_3$ nanoparticle concentration was determined by the NTA software. The number of polymer per particle was estimated by a method previously described by Zhang et al[97], and 800 molar excess of DBCO-DNA was added to PLGA-PEG-N$_3$ nanoparticles in 1X PBS/0.3% poloxamer. The reaction was incubated at 25ºC for 72 h followed by purification with Amicon Filter (size cutoff = 100 K).

Determination of surface loading: 50 µl of as-prepared Cy5-labeled PLGA-SNAs was lyophilized and then fully dissolved in 0.1 M NaOH. The solution was then neutralized by Tris-HCl (pH=7.4, Sigma-Aldrich). Then the concentration of Cy5-labeled oligonucleotide attached to PLGA-SNAs was measured by quantifying the Cy5 fluorescence (630 nm/ 670nm) against a standard curve of an identical Cy5-labeled linear oligonucleotide on a plate reader (Synergy H4 Hybrid Reader, BioTek). SNA particle concentration was determined by the NTA as described above.

Agarose gel electrophoresis: 100 mg agarose (Sigma-Aldrich) was dissolved in 100 ml 1X TBE and heated in a microwave for 70 seconds. Gel running samples were prepared by mixing 13.5 µl PLGA-SNAs or linear oligonucleotides with 1.5 µl glycerol to make the final concentration of glycerol 10%. The gel was run for 30 minutes for 100 V and then imaged by a gel imager (Typhoon GE).

Nuclease resistance assay: To compare the stability of free DNA with PLGA-SNAs against nuclease degradation, phosphodiester free oligonucleotides and PLGA-SNAs ([DNA]=10 µM; 2 µl of 10 X reaction buffer (ThermoFisher), 10 mM tris, 2.5 mM $MgCl_2$, and 0.5 mM $CaCl_2$) were subjugated to DNase I (2 µl, 2000 units/ml, ThermoFisher) degradation for 15, 30, and 120 minutes, respectively. The reactions were quenched at each desirable time point by adding 2.2 µl of 10% SDS. The reaction products were analyzed by agarose gel electrophoresis as described above and the band intensity of each individual time point was quantified and normalized to intact sample.

Imaging of NP with atomic force microscope (AFM): AFM images were performed in liquid phase aiming to measure pristine non-dried NPs heights. For this purpose, modified overnight Si/SiO_2 surface with the 1mM (3-Aminopropyl)triethoxysilane (Sigma-Aldrich) from EtOH was chosen as the most suitable substrate capable of adhering PLGA-SNA nanoparticles electrostatically. Initially, NP samples were 100X diluted in DI water and drop cast on the substrate for 10 minutes. Next, samples were rinsed with DI water (300 µl) without letting them dry and placed in AFM setup. AFM images were recorded with the ScanAsyst fluid probes having spring constant of 0.7 N/m and tip radius of 2 nm. All visualizations were done with the fixed applied force of 1 nN, where the heights of 500 individual NPs from each sample were measured manually for histograms plots.

Stability assay: The FRET PLGA-SNAs were prepared using the same method as PLGA-SNAs, except 1 mg PLGA-Rhodamine was incorporated (AV027 Akina) incubated in 1X PBS with 10 % vol FBS. The FRET signal of the Cy5-Rhodamine pair was excited at 530 nm with 5

nm slit and collected from 550 nm to 700 nm with 5 nm slit on a fluorolog (Horiba) . To ensure the FRET signal reached equilibrium, 0.2 M NaOH was added to destroy the NPs at the last time point.

Synthesis of coumarin 6 encapsulated PLGA-SNAs and drug releasing kinetics: Coumarin 6 encapsulated PLGA-SNAs are synthesized with aforementioned method, except that 0.1%, 0.5% or 1% (w/w) coumarin 6 was co-dissolved with PLGA in acetonitrile. To measure the encapsulation efficiency, coumarin 6 (50 µl) loaded PLGA-SNAs were lyophilized and then extracted with acetonitrile (100 µl). The drug loading was then measured by measuring the fluorescence intensity of coumarin 6 (excitation/emission=488/520) on a 96-well plate (Biotek). To measure the drug release kinetics, coumarin 6 encapsulated PLGA-SNAs (100 µl) is dialyzed in a dialysis tube (size cutoff=20000 Da) against buffer (2L; 10% vol% FBS in 1X PBS). At each desired time interval, PLGA-SNAs solution was taken out and lyophilized. Coumarin 6 was then extracted acetonitrile (100 µl). The drug release was evaluated by measuring the fluorescence intensity of coumarin 6 (excitation/emission=488/520) on a 96-well plate.

Cell culture studies: RAW-Blue™ (InvivoGen) cells expressing all Toll-like receptors (TLRs) excluding TLR-5 purchased from cultured and passaged as recommended by the manufacturer.

Confocal microscopy: ~500,000 RAW-Blue cells seeded on a cell culture dish (FD3510-100, World Precision Instruments) were incubated with Cy5-tagged PLGA-SNAs (100 nM DNA) in serum containing growth medium (DEME supplemented with 10% fetal bovine serum (FBS)) for an hour. Cells were washed by 1X PBS (1 ml) three times. Washed cells were then fixed with

4% paraformaldehyde for 5 minutes. Fixed cells were washed with 1X PBS for three times and were stained with DAPI (BioRad) according to manufacturer's recommended protocol. Confocal microscopy analysis of those cells was carried out with a Zeiss LSM 810 inverted laser-scanning confocal microscope (Carl Zeiss, InC., USA). DAPI was excited at 350 nm and its emission was collected at 450 nm. The Cy5 tag was excited at 640 nm and its emission data was collected at 680 nm.

Flow cytometry experiments: ~100,000 Raw-Blue cells plated on a 96-well plate were incubated with Cy5-tagged PLGA-SNAs or a Cy5-tagged free oligonucleotide (100 nM and 200 nM by DNA) for 0.5 h, 2 h, 4 h, 8 h, and 12 h. At the end of each treatment, cells were washed with 1X PBS for three times and then fixed using 4% paraformaldehyde for 5 minutes. Single suspension cells were created by scratching the bottom of each well aggressively for 5 minutes. The mean fluorescence intensity (M.F.I) of Cy5 was recorded by a flow cytometer equipped with a High Throughput Sampler (HTS) (BD LSRFortessa 6-Laser, BD Sciences, US). The experiment was performed in triplicate and error was calculated as the standard error of the mean.

Cytotoxicity studies: The cell viability of Raw-Blue cells was determined using the 3-(4,5-dimethylthiazol-2-yl)-2,5-diphenyltetrazolium bromide (MTT) assay (Sigma Aldrich). Cells were seeded in a 96-well plate at a density of 50,000 cells per well. After overnight incubation, cells were treated with PLGA-SNAs with DNA concentrations ranging from 10 nM to 2 µM. After treatment with PLGA-SNA (12 h), the cell culture medium was replaced with fresh cell culture medium (100 µl) and 12 mM MTT solution (10 µl) was added to every single well in the plate which was incubated for 4 h at 37°C. Then 100 µl of solubilizing buffer (100 µl; SDS 10% in 0.01

M HCl) were added to the wells and the plate was incubated for 4 h at 37°C. After incubation, the absorbance was measured at 570 nm using Biotek Synergy H4 Hybrid Reader. Cell viability was normalized to the untreated control, i.e., (Asample/Auntreated control)*100 and plotted as a percentage of cell viability. The experiment was performed in triplicates and the error was calculated as standard error of the mean.

PLGA-SNAs activating TLR9: Raw-Blue cells were seeded on a 96-well plate at a seeding density of ~100,000/each well. Seeded cells were incubated with PLGA-SNAs bearing TLR9-activating oligonucleotide or control sequence or linear TLR9-activating oligonucleotide overnight. All oligonucleotides used in this experiment was phosphorothioate back-bone modified. The level of TLR9 activation was then evaluated by a Quanti-Blue assay (InvivoGen, USA) according to manufacturer's recommendation. TLR9 activation was recorded in triplicate on a 96-well plate reader (Biotek) and is normalized to the untreated cells.

CHAPTER FOUR

ENHANCING GENE REGULATION WITH PLGA-SNAs

4.1 Summary

As previous chapters have introduced, gene regulation holds great promise due to highly specific Watson and Crick base pairing. In principle, small interference RNA (siRNA) or antisense DNA should be able to downregulate any genes of interest if siRNA or antisense DNA were carefully designed to follow certain design rules. In reality, being able to downregulate a certain gene of interest faces much more challenge than one would expect. First, systematically delivered siRNA or DNA need to be protected from nuclease degradation in the blood since the circulatory half-life of naked siRNA or DNA is less than 5 minutes and serum degradation half-life of them is less than 1 minute[105]. Second, naked siRNA or DNA do not enter cells by themselves. Lastly, after siRNA or DNA enter the target cells primarily via endocytosis, they need to escape from endosomes to gain cytosolic access in order to silence the target mRNA[106-110].

Spherical nucleic acid (SNA) constructs have been shown to effectively enhance nuclease resistance of oligonucleotides attached compared to the linear counterparts, probably by increasing the local salt concentration[73]. Most surprisingly, the highly negatively charged, bulky nanoparticles are able to enter more than 70 cell lines via scavenger receptor-A (SR-A) mediated endocytosis[35, 111]. Previous work in our group has shown that silencing of mRNA, such as human epidermal growth factor receptor 2 (HER2)[42], epidermal growth factor receptor (EGFR)[41], etc. However, one prerequisite that SNA constructs face in order to knockdown mRNA more effectively is to access cytosol, a challenge that most nanoparticle-mediated gene regulation would face[109, 112]. The knockdown would be more potent if we could find a way to universally increase endosomal escape efficiency. In this chapter, I further build on the study illustrated in the previous

chapter and create a PLGA-SNA structure capable of co-delivering cell penetrating peptide (CPP) and siRNA, a strategy that I will elucidate in this chapter that shows promises in enhancing gene regulation induced by SNAs.

4.2 Introduction

Gene regulation therapies via RNA interference (RNAi) or RNase H-mediated cleavage of disease-associated mRNA have provided a promising alternative to traditional small molecule or protein therapeutics. Due to highly specific Watson and Crick base pairing of nucleic acids, small interference RNA (siRNA) or antisense oligonucleotides of 19-23 base pairs (bps) can, in principle, silence any mRNA substrates of interest. This modularity at the molecular level has greatly expanded the number of disease targets that can be abolished, including the ones that traditionally deemed "undruggable" or "hard to drug" by small molecule and protein therapeutics.

Despite decades of efforts in advancing gene regulation therapies and success in clinical translation of a few oligonucleotide drugs, challenges in effectively delivering therapeutic oligonucleotides to specific site of interests are still impeding the further development of nucleic acid-based therapeutics. One of the most significant challenges in the delivery of oligonucleotides is to transport them across cellular membranes into the cells; naked, unmodified nucleic acids do not enter cells due to their relatively large size and negatively charged backbone. In addition, naked oligonucleotides exhibit a rapid degradation half-life of less than 1 minute, rendering them impotent in systematic use.

Spherical nucleic acids (SNAs) are a class of synthetic bio-nanoconjugates possessing unique properties that hold promise to overcome the above-mentioned challenges. For example, SNAs can be actively transported across cellular membranes via scavenger receptor A-mediated endocytosis. In serum, the three-dimensional oligonucleotide shell defining the SNA construct exhibits much slower nuclease degradation rate than SNAs' linear counterparts probably due to

high local salt concentration that deactivates nuclease. After SNAs enter the cells, the multi-valent, oligonucleotide shell can selectively bind to immunostimulatory ligands (TLRs) to initiate downstream immune-activation or mRNA substrates to mediate gene silencing, making them lead compounds in both immunomodulation and gene regulation therapies.

To further capitalize on SNAs' capacity to effect gene regulation, SNAs endocytosed into cells need to escape from endosomes, a challenge that universally applies to almost all nanoparticle-mediated gene silencing. One strategy to achieve this goal is to co-deliver an auxiliary agent capable of facilitating endosomal escape with a functional siRNA. To realize this strategy, a hydrophobic cell penetrating peptide termed Endoporter[107, 113, 114], was chosen as the auxiliary endosomal escaping agent due to its prevalent literature precedence. For co-delivering two therapeutic entities (siRNA and Endoporter) within one SNA, one would want the SNA to compartmentalize these two therapeutic cargos so that the release profiles can be independently controlled. For this purpose, PLGA-SNAs were an ideal candidate to encapsulate Endoporter because of the demonstrated capability of PLGA to encapsulate hydrophobic cargo and well-established controlled drug release profiles of PLGA nanoparticles.

4.3 Results

4.3.1 Preparation and characterization of Endoporter-loaded PLGA-SNA

To prepare Endoporter-encapsulated PLGA-SNAs, a modified nanoprecipitation method was utilized. Briefly, 12.5 mg PLGA/PLGA-PEG-N$_3$ (poly(lactide-co-glycolide)-b-poly(ethylene glycol)-azide) was co-dissolved with varying weight percent (1%-5%, w/w) of Endoporter in acetonitrile (Figure 4.3.1). The solution was then slowly injected into a beaker containing 20 mL nanopore water under rapid mixing to afford ~60 nm Endoporter-encapsulated PLGA-PEG-N$_3$ nanoparticles. Colloidal stability of Endoporter-encapsulated PLGA-PEG-N$_3$ nanoparticles is assessed by dynamic light scattering (DLS) when loaded with different weight percent of Endoporter under different ionic strength. Appendix 11 shows little size change has been observed for different Endoporter loading and ionic strength, indicating that as-prepared Endoporter-
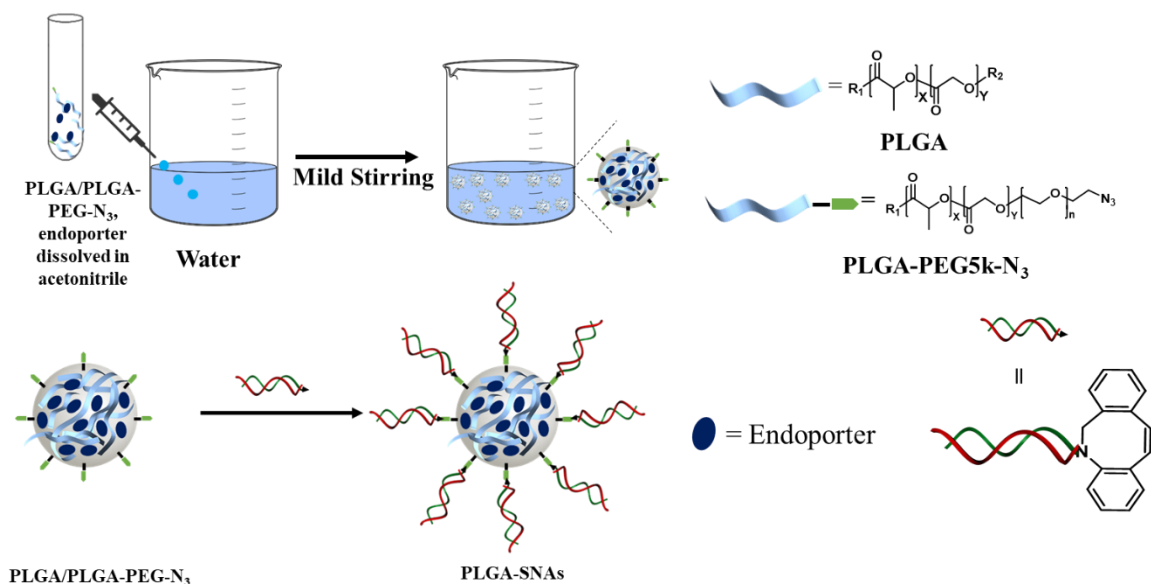
Figure 4.3.1 Preparation of PLGA-PEG-N$_3$ nanoparticles and Endoporter-loaded PLGA-SNAs via a modified nanoprecipitation method followed by copper-free click chemistry

encapsulated PLGA-PEG-N$_3$ nanoparticles are tolerant of higher Endoporter loading and ionic strength reflected by NaCl concentration.

We hypothesize that conversion of Endoporter-encapsulated PLGA-PEG-N$_3$ nanoparticles will make the particles even more stable due to electrostatic stabilization effect of oligonucleotides. Surface functionalization of PLGA-PEG-N$_3$ nanoparticles was achieved by previously described methods. The concentration of PLGA-PEG-N$_3$ nanoparticles was determined by a Nanoparticle Tracking Analysis system (NTA), and 1 molar equivalent of dibenzocyclooctyne (DBCO)-terminated siRNA was incubated with PLGA-PEG-N$_3$ nanoparticles for 24 h with 0.3% (v/v) poloxamer. Interestingly, contrary to our hypothesis and previous study that surface functionalization could make the particles more stable, Endoporter-encapsulated PLGA-SNAs are more susceptible to Endoporter loading and ionic strength of the solution. Appendix 12 shows that 5% Endoporter initial feed amount with 125 mM NaCl concentration readily causes an aggregate as demonstrated a size enlargement by DLS and the opaqueness of the SNA solution. The cause of such instability and aggregation may come from a combination of increased ionic strength in solution and increased hydrophobic cargo loading. These two factors make PLGA-SNAs interface with the aqueous solution less energetically favorable. Another likely cause is that the negatively charged siRNA bridges the positively charged particles, leading to precipitations from the solutions, despite the use of poloxamer as a surfactant. In order to prepare colloidally stable SNAs

suitable for downstream biological applications, the initial feed of Endoporter has been decreased to 3% for all the following experiment.

After formulation optimizations, the Endoporter-encapsulated PLGA-SNAs were prepared with 3% initial Endoporter loading, followed by surface functionalization described above. The size of particles increased from 73 nm (PDI = 0.25) to 89 nm (PDI = 0.22) (Figure 4.3.2), consistent

(A)

(B)

(C)

	Diameter (nm)	PDI	siRNA/ particle	Endoporter/ particle
Endo-PLGA	72.5	0.25	N/A	N/A
Endo-PLGA SNA	89.0	0.22	130	820

(D)
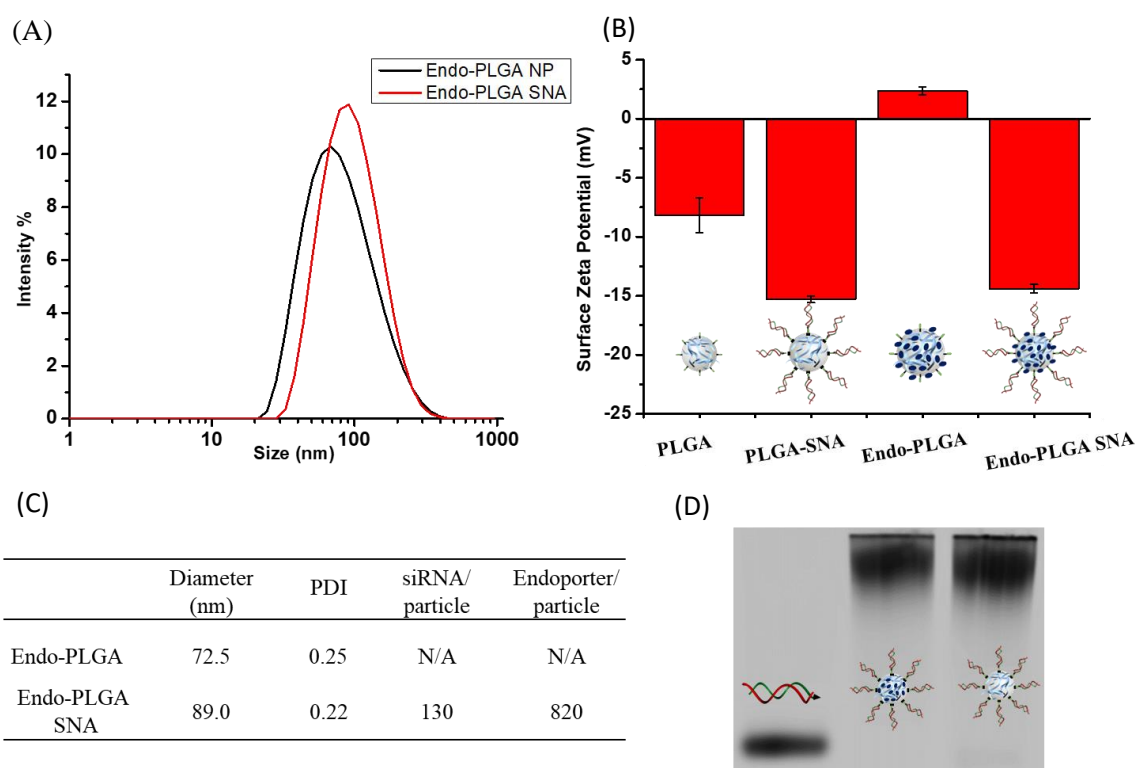
Figure 4.3.2 Characterization of Endoporter-loaded PLGA-SNAs with 3% initial Endoporter feed amount. (A) Dynamic light scattering (DLS) diagram shows size of as-prepared Endoporter-loaded PLGA-PEG-N$_3$ nanoparticles and Endoporter-loaded PLGA-SNA after surface functionalization. (B) Surface zeta-potential of PLGA-PEG-N$_3$ nanoparticles, PLGA-SNAs, Endoporter-loaded PLGA-PEG-N3 nanoparticles, and Endoporter-loaded PLGA-SNAs. (C) Table showing the diameter, PDI, number of siRNA/particle and Endoporter/particle for Endoporter-loaded PLGA-PEG-N3 nanoparticles and Endoporter-loaded PLGA-SNAs. (D) Agarose gel electrophoresis of linear siRNA and Endoporter-loaded PLGA-SNAs

with the length of a 21 bp siRNA sequence. PLGA nanoparticles without any load shows a surface Zeta potential of ~-7.5mV due to the negatively charged carbonyl group. PLGA-SNAs without loads exhibit an even more negatively charged surface potential due to immobilization of siRNA. The encapsulation efficiency for Endoporter-loaded PLGA nanoparticles and Endoporter-loaded PLGA-SNAs was $(31.7 \pm 6.4)\%$ and $(24.6 \pm 1.6)\%$, respectively. Interestingly, the Endoporter-loaded PLGA-PEG-N_3 exhibits a slightly positive surface Zeta potential, indicating a portion of Endoporter has been electrostatically adsorbed to the surface of PLGA-PEG-N_3 nanoparticles. Indeed, the surface zeta potential becomes more positive (Appendix 13) when increasing amount of Endoporter was loaded. After surface functionalization, the surface charge dropped to the similar level as PLGA-SNAs, suggesting that the positive charge of surface-bounded Endoporter has been masked by the siRNA shell, a favorable characteristic that could potentially minimize nonspecific toxicity from positively charged particles[115].

4.3.2 Release kinetics of Endoporter-loaded PLGA-SNA

Next, we evaluated our hypothesis whether Endoporter-loaded PLGA-SNAs were capable of releasing Endoporter in a controlled and tunable manner. For this purpose, we prepared FRET Endoporter-loaded PLGA-SNAs (FELPS) by labelling Endoporter with Cy5 and incorporating small amount of rhodamine-labelled PLGA. Cy5 signal ($\lambda_{em} = 675$ nm) can be detected by exciting at rhodamine excitation wavelength ($\lambda_{ex} = 520$ nm) while no FRET signal was observed for PLGA-SNAs prepared with only rhodamine-labelled PLGA (Appendix 14). To elucidate the structure-property relationships of this construct, we asked two questions: (i) how fast Endoporter is released from the particles under endosomal pH and (ii) whether we can fine tune the release profile by
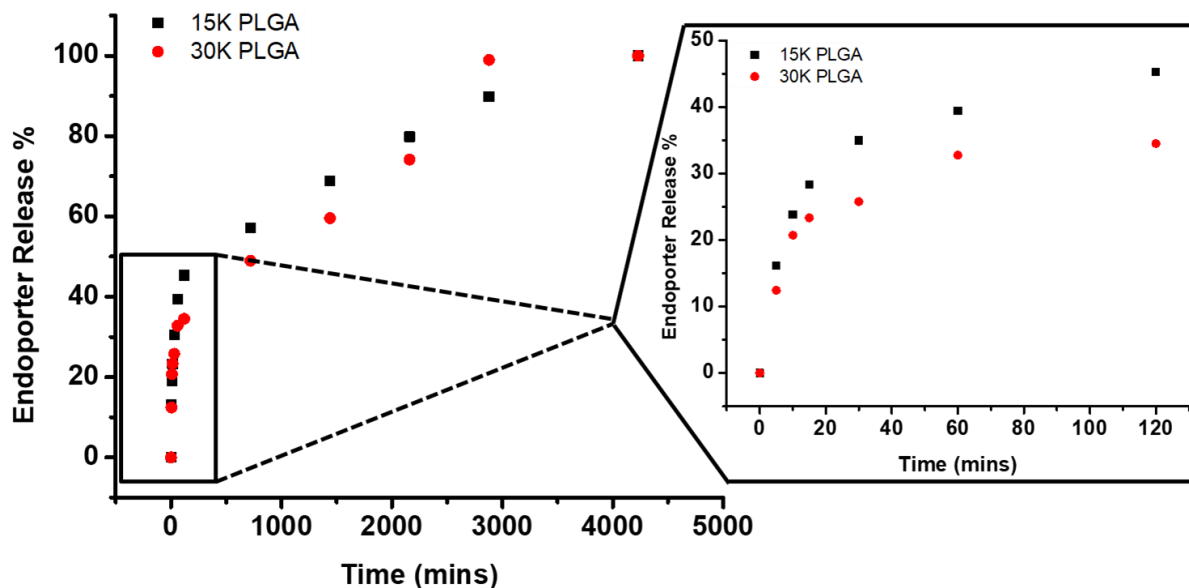
Figure 4.3.3 Endoporter release profile of PLGA-SNAs prepared from 15K PLGA and 30K PLGA. Black square: 15K PLGA; red dot: 30K PLGA.

changing the chemical composition of PLGA. To answer both questions, FELPS made from

PLGA with different molecular weights were incubated at pH 5.0 simulating endosomal conditions and kept at 37º. Cy5 signal from exciting at rhodamine wavelength was monitored. The change of Cy5 signal at each individual time point was used as a reference to calculated release of Endoporter by normalizing to the difference of fluorescence signal between initial and final time point. It was observed that FELPS prepared from PLGA with both molecular weights (15K and 30K) fully released Endoporter in 72 h. In both formulations, release of Endoporter occurred primary within the first 2 h (~45% and 30% for 15K and 30K, respectively), indicating a burst release profile arising from surface-bounded Endoporter, a property characteristic of PLGA and polymeric nanoparticle release. Compared the release of FELPS made from 15K PLGA to that of FELPS made from 30K PLGA, the release from FELPS made from 15K PLGA is faster throughout 72 h except for last time point. The slower release of larger molecular weight composition is consistent with literature and might be due to stronger interaction between the polymer chain and Endoporter. To assess whether this trend holds true for different formulations, two more FELPS were prepared with more PEG contents aiming to further improve colloidal stability. Despite the burst release from FELPS has accelerated for these FELPS prepared from lower PEG content within 2 h, the FELPS made from lower PEG contents exhibit similar trends in release kinetics, where low molecular weight PLGA gives lower Endoporter release rate.

4.3.3 Intracellular functions of Endoporter-loaded PLGA-SNAs

Lastly, we evaluated the intracellular functions of Endoporter-loaded PLGA-SNAs to knockdown isocitrate dehydrogenase (IDH1) due to its significance in glioblastoma (GBM). U87
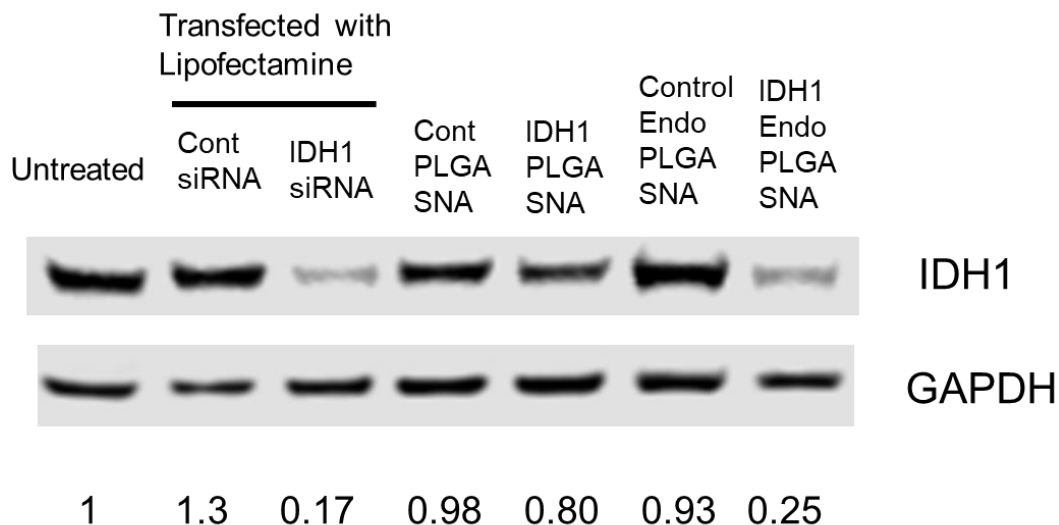
Figure 4.3.4 GBM U87 cells treated with Endoporter-loaded PLGA-SNAs targeting IDH1. [siRNA]=300 nM; treatment time=72 h. GAPDH was chosen as a housekeeping protein.

GBM cells were treated with Endoporter-loaded PLGA-SNAs for 72 h before the cells were harvested for protein expression analysis. Figure 4.3.4 shows that IDH1 PLGA-SNAs have only a modest knockdown of ~20%, probably due to the fact that most PLGA-SNAs were inside endosomes. Co-delivery of Endoporter with siRNA by Endoporter-loaded PLGA-SNAs shows an enhanced knockdown of ~75%, indicating that loading of Endoporter could increase knockdown efficiency. Lastly, we tested whether IDH knockdown exhibits a dose-dependent pattern. U87 cells were treated with Endoporter-loaded PLGA-SNAs at 1 µM, 2 µM, and 4 µM (by Endoporter). The knockdown of IDH1 increased from ~20% to 70% (Appendix 15). One concern for delivering these membrane destabilizing peptides is their cytotoxicity. To assess the cytotoxicity of Endoporter-loaded PLGA-SNAs, U87 cells were treated with Endoporter-loaded PLGA-SNAs

ranging from 2 µM to 10 µM (by Endoporter). No apparent toxicity was observed across these concentrations (Appendix 16).

4.4 Conclusion

This chapter details efforts to overcome one of the main challenges in nanoparticle-mediated gene silencing, access to cytosol. SNAs enter cells through the endocytic pathways, which leads to accumulation inside endosomes. While SNAs show potent gene regulation in certain cells, we have seen that the gene silencing is cell- and sequence-dependent. This leads us to come up with an approach that can potentially increase gene regulation universally across different cell lines and different target genes. Specifically, a cell-penetrating-peptide (CPP) was loaded onto PLGA-SNAs as an auxiliary agent to help siRNA escape from endosome. A systematic formulation study was performed to address aggregation caused by unfavorable charge-charge interaction. In addition, this is the first time that we demonstrate that the SNA construct, comprised of a benign, biodegradable, biocompatible core material, can release loaded macromolecule in a tunable and controlled manner. Lastly, we have shown that Endoporter-loaded PLGA-SNAs can knockdown IDH1 in a more potent manner than IDH1 PLGA-SNAs.

4.5 Experimental methods

Oligonucleotide synthesis: oligonucleotide synthesis was performed on a MMermade 12 DNA synthesizer (MM12). Glass controlled pore (GPC) support was purchased from ChemGenes. Reagents used for oligonucleotide synthesis was purchased from Glen Research. Oligonucleotides were synthesized according to manufacturer's recommendation. As-synthesized oligonucleotides were cleaved from GPC support by incubation with ammonium hydroxide (Sigma-Aldrich, 38%-40%). The solution containing oligonucleotides were dried by a nitrogen gun followed by injecting into a reverse-phased high-performance liquid chromatograph (RP-HPLC). with a Microsorb C18 column. After HPLC purification, DMT group of purified oligonucleotides was removed with 20% (v/v) acetic acid followed by ethyl acetate extraction. The molecular weight of oligonucleotides was determined by a matrix-assisted laser desorption/ionization time of flight mass spectrometer (MALDI-TOF) (Bruker).

Preparation of PLGA-PEG-N$_3$ nanoparticles and Endoporter-loaded PLGA-SNAs: PLGA-PEG-N$_3$ nanoparticles were prepared via a previously described method. Briefly, 12.5 mg mixture of PLGA (7000-17000, Resomer® RG 502 H, Sigma-Aldrich) and PLGA-PEG-N$_3$ (Akina) dissolved in 5 mL acetonitrile was added dropwise to a beaker containing 20 mL water under rapid stirring. The weight ratio PLGA and PLGA-PEG-N$_3$ is adjusted in the specific experiments described in the manuscript. To prepare endoporter-loaded PLGA-SNAs, 3% endoporter was co-dissolved with polymer mixture in acetonitrile. The concentration of endoporter-loaded PLGA-PEG-N$_3$ was determined by a Nanoparticle Tracking Analysis system (NTA, Malvern, NanoSight

NS300). One-molar equivalent DBCO-terminated siRNA was added to endoporter-loaded PLGA-PEG-N$_3$ nanoparticles and incubated for 24 h under 25ºC in 1X PBS/0.3 (v/v) poloxamer.

Dynamic light scattering (DLS) and surface zeta potential measurement: as-prepared nanoparticles were diluted 1:100 for both DLS and surface zeta potential measurement that is performed with Zetasizer (Malvern zetasizer nano zs)

Agarose gel electrophoresis: 100 mg agarose (Sigma-Aldrich, molecular biology grade) was dissolved in 100 mL 1X TBE and microwaved for 70 seconds. A typical loading sample contains ~1 µM analyte (by siRNA concentration) and 1.5 µL glycerol (5%). The gel was run at 100 V for 30 minutes and was stained with SYBR Gold nucleic acid gel stain (Invitrogen). The membrane was then imaged by a gel imager (GE Typhoon) using SYBR Gold channel (λ_{ex} = 495 nm and λ_{em} = 537 nm).

Quantification of siRNA duplex loading: To quantify the number of antisense strands functionalized to the Endo-Porter encapsulated PLGA-SNA, previously described method was modified. Briefly, 20◻l of Endo-Porter encapsulated PLGA-SNAs (in 1◻ PBS, 0.3% (v/v) Poloxamer 188) were resuspended in 130◻l of 8M Urea and heated to 45 °C for 20 min to dehybridize the antisense strands from the DBCO modified sense strands, which would remain on the PLGA-SNA. Then the solution was centrifuged 10 min at 8000 ◻ g. To confirm that the supernatant contained only the antisense siRNA strands, the supernatant was washed with RNase free 5 times water using Amicon filter (0.5 ml, size cut off= 3K) for 25 min at 14000 ◻ g to remove the 8M urea, poloxamer 188 and PBS salt. Then, MALDI-TOF analysis was performed to confirm that the supernatant contained only the antisense strands. The concentration of antisense strand

was measured by Quant-iT OliGreen assay (Thermo Fisher). Briefly, portion of the supernatant (25 □l) that contains 130 □l 8M urea and 20 □l 1□PBS, 0.3% (w/v) poloxamer 188 was analyzed by mixing with OliGreen reagent in a clear bottom black 96-well plate and fluorescence was measured using a BioTek Synergy Microplate Reader with excitation/emission wavelengths of 480 nm/520 nm. The concentration was determined based on standard curves of known antisense RNA concentrations incorporating same concentrations of Urea, PBS salt and poloxamer 188 compared to the analyte.

Quantification of Endoporter loading: To measure the encapsulated Endo-Porter concentration, Endoporter encapsulated PLGA-SNAs in 1□ PBS, 0.3% (v/v) Poloxamer 188 (50 µL) were lyophilized first. Then the lyophilized pellets were suspended in 0.2 M NaOH (50 µL) and incubated in 60 °C for 20 min to fully dissolve the nanoparticle core. 0.2 M Tris-HCl (50 µL) was then added to neutralize the solution and followed by adding DMSO (100 µL) to fully solubilize the Endo-Porter peptide. The concentration of Endo-Porter was measured against a standard curve with known concentration of Endo-Porter incorporating same concentrations of PBS salt, Polamxer 188, NaOH, Tris-HCl and DMSO. Then the Endo-Porter concentration was measured using PierceTM 660nm Protein Assay Reagent (Thermo Fisher) measuring the absorbance at 660nm in a clear bottom black 96 well plate (Biotek synergy plate reader).

Drug release kinetics: 3% (w/w) Cy5-labelled endoporter (M.W = 4400 Da; Northwestern Peptide Core) was incorporated into PLGA-PEG-N$_3$ using previously described methods, except that 1 mg rhodamine-PLGA was incorporated. 50 µL Cy5-labelled endoporter PLGA-SNAs were added to 1450 µL pH 5.0 1X PBS buffer at 37ºC. The solution was excited at 520 nm and FRET

signal (Cy5) was recorded from 550 nm to 700 nm on a FluoroLog Spectrophotometer (HORIBA). The Cy5 signal was recorded at each specific time point until 72 h, when concentrated HCl was added to ensure no noticeable change in Cy5 fluorescence will occur. The drug release at each time point (t) was calculated as $\frac{F(initial)-F(t)}{F(initial)-F(final)} * 100\%$.

Toxicity assay: The cell viability of U87 cells was determined using PrestoBlue® Cell Viability reagent (Thermo Fisher). Cells were seeded in a clear bottom black 96-well plate at a density of 10,000 cells per well. After overnight incubation, cells were treated with Endo-Porter encapsulated PLGA-SNAs and Endo-Porter with different Endo-Porter concentrations. After treatment for 72 hours, effects of Endo-Porter on cell viability was measured following the manufacturer's protocol. Briefly, after the washing the wells with 1□PBS, the plate was filled with 90 µL of DMEM + 10% FBS + 1% pen-strap and 10 µL of 10 □ PrestoBlue® reagent. The plate was then incubated at 37°C for 2 h followed by measuring the fluorescence of the plate with excitation/emission wavelengths of 560 nm/590 nm. After subtracting the average fluorescence values of the no-cell control wells, the cell viability was normalized to the untreated control and plotted as a percentage of cell viability. The experiment was performed in triplicates and the error was calculated as standard error of the mean.

Knockdown of IDH1: To assess the gene knockdown activity of Endo-Porter encapsulated PLGA-SNAs, U87 cells were seeded in a 12-well plate at a density of ~200000 cells per well. After overnight incubation, Endo-Porter encapsulated IDH1 PLGA-SNAs were treated to the cells for 72 hbased on different Endo-Porter concentrations based on Endo-Porter concentration encapsulated to the SNA. The cells were also treated with Endo-Porter encapsulated control

PLGA-SNA, un-encapsulated IDH1 and control PLGA-SNA. As a positive control and negative control, linear IDH1 siRNA duplex and linear control siRNA duplex was transfected Lipofectamine RNAiMAX (Thermo Fisher). IDH1 knockdown effect was determined by Western blot.

Western blotting: Protein lysates were extracted using radioimmunoprecipitation assay buffer (RIPA buffer) with Halt Protease Inhibitor cocktail that contains 1 X protease and 1 X phosphatase inhibitor (Thermo Fisher). 30 □g of protein sample per sample was separated using 4-12% SDS-PAGE (Life technologies) in 100 V, 70 min. Then protein gel was transferred to nitrocellulose membrane (Life Technologies) using iBlot® 2 Gel Transfer Device (Life Technologies). Then the membranes were blocked with Odyssey® Blocking Buffer (Li-COR) in room temperature for 1 h and were incubated overnight at 4°C with the following antibodies: rabbit anti-IDH1(Cell Signaling Technology, 1:1000 dilution) and mouse IgG1 anti-HSP70 (BD biosciences, 1:2000 dilution). After the blots were washed with 1□ PBS with 0.1% Tween-20 three times for 5 min, the membranes were incubated with IRDye® 800CW-conjugated goat anti-rabbit secondary antibody (Li-COR, 1:2000 dilution) and IRDye® 800CW-conjugated goat anti-mouse IgG1 secondary antibody (Li-COR, 1:2000 dilution) for 1 h. Then the membranes were washed with 1□ PBS with 0.1% Tween-20 three times for 5 min. To remove, residual Tween-20, the membrane was rinsed in deionized water three times before scanning. Then the blot image was acquired using Odyssey® CLx Imager (Li-COR) at 169 □m resolution in the 800nm fluorescence channel. Then the band intensity of the blot was quantified by Image J (reference needed)

normalized to the untreated control group. All Western blots were performed in triplicates and the error was calculated as standard error of mean.

CHAPTER FIVE

CONCLUSIONS AND FUTURE DIRECTIONS

5.1 Summary

The SNA construct has advanced the field of gene regulation therapies and immunomodulation in past decades, and there is no reason to believe that it will stop doing so. In this chapter, I will outline three future ideas built upon my scar attenuation and PLGA work.

The first future direction is to use the SNA to attenuate fibrosis diseases. This application is a natural extension from scar attenuation due to many overlapping genetic and molecular causes between these two diseases.

The second future direction is to study spatial distribution of SNAs bearing different oligonucleotide inside real human skin. This is important as there are >200 skin diseases with known genetic cause. Being able to probe the kinetics of SNA penetrating skin and localization of the SNAs at the cellular level is paramount to inform the future development targeting these skin diseases.

The third future direction is to evaluate the possibility of using drug-loaded PLGA-SNAs as a combination therapy. As previous chapters demonstrated, one advantage of using PLGA-SNAs is their ability to tune the drug release profile independent of siRNA release. This provides the opportunity to synergize the drug effect of encapsulated agents with siRNA knockdown.

5.2 SNAs targeting fibrosis

Fibrosis has created significant social health burdens. In the U.S, there are over 200,000 new liver fibrosis (cirrhosis) and over 30,000 lung fibrosis cases[116]. Some of the fibrosis is fetal; patients diagnosed with idiopathic pulmonary fibrosis, for example, only have a median survival time of 3-5 years[66]. It has become a leading death cause in the globe and a financial burden of $2 billion in the U.S alone[117]. Fibrosis disease is defined by inflammation of local tissue, overactivation of myofibroblasts, and an imbalance between extracellular matrix (ECM) secretion and breakdown[66, 118]. Abnormal scar can be considered a specific sub-type of fibrosis that secretes excessive collagen on the skin. Therefore, abnormal scarring and fibrosis share overwhelmingly similar genetic and molecular causes.

Central to fibrosis is upregulation of growth factors (PDGF, TGFβ), cytokines (IL-13, IL-12, TGFβ1), and recognition of pathogen by pattern recognition receptors (Toll-like receptors) (ref). The secretion of these cytokines and chemokines promotes the generation of myofibroblasts, which in turn secret over-abundant ECM proteins and tissue inhibitor of metalloproteinase 1 (TIMP1). TGFβ1 is considered as the "master regulator" of fibrosis that orchestrates most of signaling pathways pertaining to fibrosis via canonical smad and non-smad pathways[118].

Liver fibrosis is the primary fibrotic phenotype that people are diagnosed with. Passively targeting liver provides a unique opportunity for SNA constructs since systematically injected SNAs primarily accumulate in the liver and spleen, with small portions in the lung[47].

To realize this potential, siRNA or antisense oligonucleotide sequences homologous to human and mouse capable of knocking down TGFβ1 will first be screened by qRT-PCR with

transfection agents in human or mouse liver fibroblasts. The ability to find homologous sequences would make this work more clinically relevant. Different modes of chemical modifications for oligonucleotides, such as phosphorothioate (PS) backbone modification, locked nucleic acids (LNA), and 2'-O-methyl gapmers should be incorporated in various combinations. These modifications can potentially increase nuclease resistance and increase binding affinity of the targeting sequence. The sequences that show the most potent downregulation will be chosen to functionalize particles. Liposomal SNAs (LSNA) and PLGA-SNAs will be utilized as the primary constructs for this purpose because they are the biocompatible and biodegradable constructs among all SNAs with a track record of being taken into clinics. TGFβ1 gene silencing and protein downregulation induced by LSNA and PLGA-SNAs will be then evaluated in human and mouse fibroblasts via qRT-PCR and Western Blot, respectively.

After establishing the LSNAs and PLGA-SNA constructs capable of silencing TGFβ1 *in vitro*, their efficacy will be evaluated *in vivo* in a CCL4-induced liver fibrosis mouse model[119]. To evaluate the *in vivo* efficacy of SNA treatment, various SNA concentration will be administered intravenously with eight repeated injections within a month. After a month, the mouse will be sacrificed, and liver tissue will be harvested for analysis. Whole RNA and protein will be extracted from tissues, and expression level of TGFβ1 will be assessed via qRT-PCR and Western blot. To investigate whether SNA treatment can improve fibrosis histology, liver tissue will be sectioned, imbedded, and H&E stained followed by calculating the fibrosis score by a trained professional doctor.

Lastly, the survival of SNA-treated mice, SNA scrambled-treated mice, and non-treatment group will be compared to evaluate whether SNA can improve life expectancy of fibrosis bearing mice.

5.3 Assessing spatial localization of SNAs in skin

The diverse population of cells residing inside skin provides a great opportunity for transdermal drug delivery. For example, fibroblasts are the main cell type responsible for abnormal scar formation by differentiating to myofibroblasts and increasing collagen deposition. Keratinocytes, account for over 90% of cells in skin, are primarily responsible for secreting TNF-α that leads to autoimmune disease such as psoriasis. In addition to these two skin cells, skin also has a wide range of immune cells, opening up potential opportunities for topical vaccination[120-122].

A challenge with developing transdermal drug delivery is to cross skin barrier. Epidermal layer of skin consists of four layers, stratum corneum, stratum granulosum, stratum spinosum, and stratum basale. These layers are highly lipophilic and inhibit exogenous substance from entering the skin. Therefore, skin is traditionally deemed impermeable to macromolecule drugs with molecular weight of more than a few hundred Dalton and is reserved for small molecule drugs[59, 61]. Surprisingly, recent studies on spherical nucleic acids (SNAs) have shown that not only SNAs were able to enter cells but can also penetrate intact mouse skin and human explants. The exact mechanism for SNAs entering skin is not well understood. SNAs penetrating skin can also suppress certain key genes implicated in diseases such as EGFR[72] and TGFβ1 (described early).

One important question to ask is what skin cells take up SNAs and whether the distribution of SNAs inside skin is sequence-dependent. Being able to answer these two questions provides insight to inform future development of topical SNA treatment. Most previous studies utilize either mouse skin or human skin explants as model systems; these models do not perfectly reflect

characteristics of real human skin, such as thickness. In this study, real human skin will be used to simulate realistic therapeutic scenario. Due to the abundance of fibroblasts and keratinocytes, SNA distribution was first evaluated in these two cell types.

Real skin tissues are purchased from skin tissue banks and are sterilized in 10% (v/v) Ethanol upon arrival. Round-disk shape skin samples was obtained by punching the skin samples with 7 mm punch biopsy. To investigate what skin cells take up SNAs and whether SNA distribution is sequence-dependent, AuSNAs bearing GGT or poly-T were prepared and then mixed with a commercially available ointment (1:1 v/v), Aquaphor, to increase viscosity. 10 µL SNA (500 µM by particles) mixture was topically applied to the real human skin which was kept in a trans-well in DEME medium under 5% CO_2 for 72 hours. After the treatment, skin was dissociated with tissue digestion kit, which separates epidermis layers and dermis. This method has been optimized to produce approximately 2.5×10^4 viable epidermal cells and 6.7×10^5 viable dermal cells. The Cy5 signal was quantified using flow cytometry. The flow cytometry data
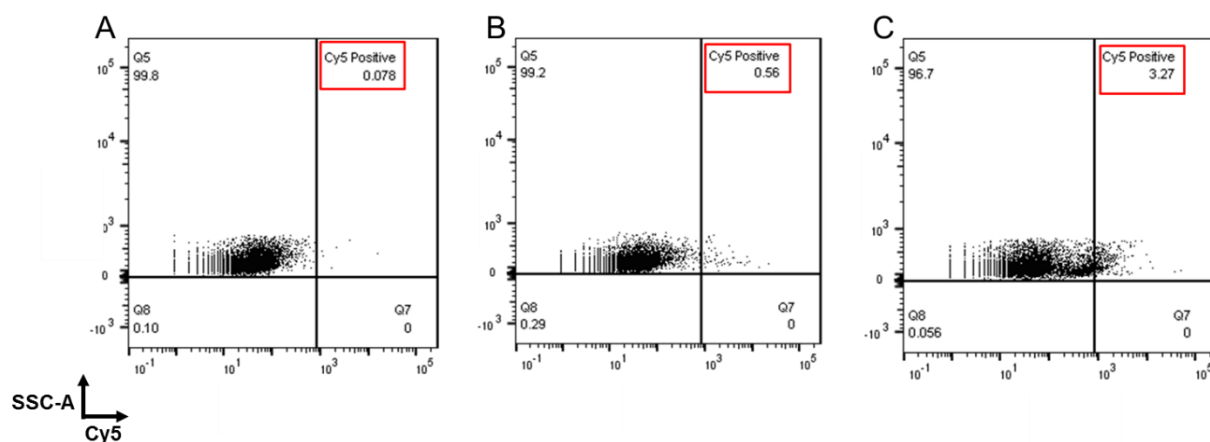
Figure 5.1 Time-dependent uptake of SNAs into the dermis. (A) Non-treated skin. (B) Skin treated with SNAs for 12 hours. (C) Skin treated with SNAs for 24 hours.

suggests that SNA penetration into dermis cells is time-dependent (Figure 4) over 24 hours, as evidenced by an increased population of Cy5-positive cells from 0.56% at 12 hours to 3.27% at 24 hours.

Next, we studied how the stratum corneum affects SNA skin penetration. The intact or stratum corneum-removed skin was treated with 500 nM Cy5-tagged poly-G SNAs. The amount of Cy5-positive dermis cells in the stratum corneum-removed sample significantly exceeds the stratum corneum-intact one at both 12 hours and 24 hours (Figure 5). These results indicate that

within a 24-hour treatment period, the stratum corneum is the main barrier to SNA entry into the dermis.

We have demonstrated that a reliable method has been developed to separate epidermis from dermis to form single skin cell suspension. In the next step, antibody-fluorophore conjugates
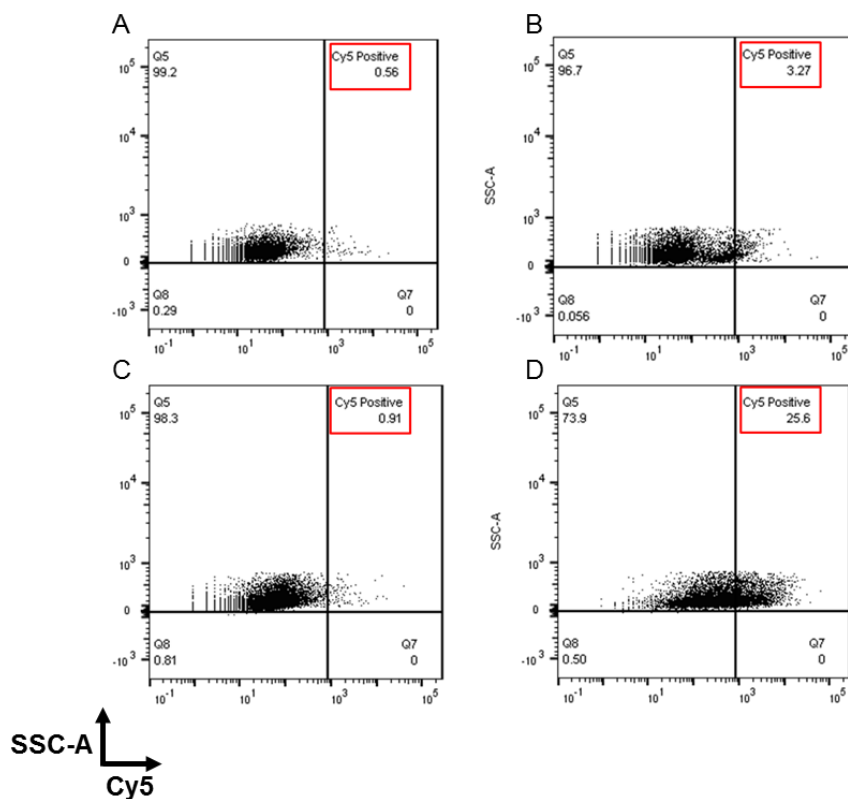
Figure 5.2 SNAs penetration into dermis in native skin or skin without stratum corneum. (A) stratum corneum intact skin treated for 12 hours. (B) stratum corneum intact skin treated for 24 hours. (C) stratum corneum removed skin treated for 12 hours. (D) stratum corneum removed skin treated for 24 hours.

capable of staining fibroblasts and keratinocytes will be utilized to quantify SNA distribution in these two cell types.

5.4 Engineering a versatile PLGA-SNAs combination platform for combination therapy

One of the main challenges in treating cancer is to circumvent chemoresistance of cancer cells to chemotherapy drugs. With combination therapy, it is possible to mitigate drug resistance of cancer cells before dosing chemotherapy drugs. Specifically, when a chemotherapy drug was co-delivered with antisense oligonucleotide against genes that desensitize cancer cells, enhanced killing of cancer cells was observed[98]. One challenge with this approach is the difficult with which both therapeutic agents need to be co-delivered within one nanocarrier. The second challenge for combination therapy is whether the temporal release of the two drugs can be tuned in a meaningful manner. One classic example that demonstrates the necessity for differential release is Shiladitya's work where a PLGA nanocell was synthesized, loaded with an anti-angiogenesis agent in the outer lipid shell and a chemotherapy drug in the PLGA NP core. The nanocell was able to generate a differential release profile between those two drugs, showing substantially improved tumor reduction[123]. To overcome the "undruggable" challenge of small molecule drugs, nucleic acid therapy can be utilized to regulate undruggable targets with superior efficiency and specificity. To obtain a spatiotemporal control over the release of two drugs and broaden the scope of disease targets, PLGA-SNAs will be a promising structure that can efficiently deliver nucleic acids to regulate disease associated genes followed by the controlled release of chemotherapy drugs from the PLGA NP core. The SNA construct also provides advantages for compartmentalizing these two therapeutic cargos so that the loading of these two drugs can be independently optimized. As demonstrated in previous chapters, PLGA-SNAs were capable of releasing loaded cargos in a

tunable manner, while the rate of release of oligonucleotide shell remains relatively constant for different PLGA formulations.

Glioblastoma (GBM) is one of the most aggressive forms of cancer with a median survival time of less than 15 months with current standard treatment by temozolomide (TMZ) in addition to radiotherapy (RT)[124]. One of the main factors that significantly reduces the efficacy of TMZ and RT treatment is chemoresistance of GBM cancer cells, primarily developed by a drug resistant gene called O^6-methylguanine–DNA methyltransferase (MGMT)[125]. Suppression of MGMT has been shown to correlate with a longer life span of GBM patients[124]. The illustration of the role of MGMT has promoted an interest in developing combination therapy for GBM, where inhibitors of MGMT and TMZ are administrated simultaneously. However, current combination therapies suffer from two drawbacks: first, combination therapies dosing different drugs sequentially in different vehicles makes it difficult to deliver the active components to the same location with favorable kinetics to maximize synergistic effect[126]. Second, certain targets cannot be neutralized by small molecule drugs due to lack of binding sites[5] To test the hypothesis that PLGA-SNAs can deliver more potent therapeutic outcome via compartmentalization of these agents, GBM will be utilized as the disease model. To engineer a combination therapy platform for GBM, the dual functional PLGA-SNA is designed as follows: small interference RNA (siRNA) duplexes that can knockdown MGMT will be conjugated to the surface of PLGA NPs while TMZ will be encapsulated inside the PLGA NP core. Administered PLGA-SNAs will sensitize GBM tumor cells by knocking down MGMT followed by eradicating tumors cells through a controlled release of TMZ. To engineer such dual functional PLGA-SNAs, I plan to encapsulate TMZ in PLGA NP

core and synthesize TMZ encapsulated PLGA-SNAs using the developed method from stage one. TMZ loading will be quantified by measuring the absorbance of TMZ at 328 nm with a UV-vis spectrometer. To obtain the differential drug release profile, TMZ encapsulated PLGA-SNAs will be synthesized with an equal molar ratio of BHQ 2-Cy 3 DNA as described in stage two of the proposal. The releasing profile of TMZ will be quantified over a course of 72 hours by measuring the absorbance of TMZ at 328 nm. As work from the Mirkin and Stegh group have shown, MGMT-targeting SNAs suppress MGMT most effectively within a window from 24 hours to 48 hours after administration (unpublished work). Therefore, it is essential to ensure a maximum TMZ release within 24-48 hours following administration. Exploiting the tunable release properties resulting from structural diversity of PLGA, I will engineer PLGA-SNAs with a maximum TMZ release within 24-48 hours from the polymer matrix by systematically changing the PLGA polymer structural characteristics such as the molecular weight, terminal end, and the molar ratio of PLA to PGA. After establishing a formulation for the release controlled PLGA-SNAs, I will test the efficacy of the particles in terms of MGMT knock down and cytotoxicity in vitro. MGMT knockdown and cytotoxicity will be evaluated by RT-qPCR and Prestoblue assay. After confirming the efficacy of PLGA-SNAs in vitro, future work will be focused on systematically administrating these PLGA-SNAs with Professor. Stegh's laboratory to use this combination therapy platform for treating GBM in vivo. This temporally controlled combination therapy platform can potentially be extended to other applications that benefit from the combination of gene regulation and chemotherapy.

REFERENCES

[1]   M. L. Stephenson, P. C. Zamecnik, *Proc. Natl. Acad. Sci. USA* **1978**, 75, 285.

[2]   K. M. Schoch, T. M. Miller, *Neuron* **2017**, 94, 1056.

[3]   C. Rinaldi, M. J. A. Wood, *Nat Rev Neurol* **2018**, 14, 9.

[4]   G. L. Verdine, L. D. Walensky, *Clin. Cancer Res.* **2007**, 13, 7264.

[5]   J. S. Lazo, E. R. Sharlow, *Annu Rev Pharmacol Toxicol* **2016**, 56, 23.

[6]   A. Fire, S. Q. Xu, M. K. Montgomery, S. A. Kostas, S. E. Driver, C. C. Mello, *Nature* **1998**, 391, 806.

[7]   R. W. Carthew, E. J. Sontheimer, *Cell* **2009**, 136, 642.

[8]   J. E. Wooldridge, Z. Ballas, A. M. Krieg, G. J. Weiner, *J Investig Med* **1996**, 44, A375.

[9]   G. J. Weiner, H. M. Liu, J. E. Wooldridge, C. E. Dahle, A. M. Krieg, *Proc. Natl. Acad. Sci. USA* **1997**, 94, 10833.

[10]   J. E. Wooldridge, Z. Ballas, A. M. Krieg, G. J. Weiner, *Blood* **1997**, 89, 2994.

[11]   P. S. Walker, T. Jakob, A. M. Krieg, M. C. Udey, J. Vogel, *J Investig Dermatol* **1998**, 110, 500.

[12]   T. L. Warren, B. S. Buikema, G. J. Weiner, *Blood* **1999**, 94, 61b.

[13]   D. M. Klinman, *Nat. Rev. Immunol.* **2004**, 4, 248.

[14]   T. Jakob, P. S. Walker, A. M. Krieg, M. C. Udey, J. C. Vogel, *J Immunol* **1998**, 161, 3042.

[15]   D. Yu, Q. Zhao, E. R. Kandimalla, S. Agrawal, *Bioorg Med Chem Lett* **2000**, 10, 2585.

[16]   M. Ghildiyal, P. D. Zamore, *Nat. Rev. Genet.* **2009**, 10, 94.

[17]   K. A. Whitehead, R. Langer, D. G. Anderson, *Nat. Rev. Drug Discov.* **2009**, 8, 129.

[18]   I. Dovydenko, I. Tarassov, A. Venyaminova, N. Entelis, *Biomaterials* **2016**, 76, 408.

[19]   D. Luo, W. M. Saltzman, *Nat. Biotechnol.* **2000**, 18, 33.

[20]   M. A. Ilies, U. Satyal, V. D. Sharma, *Control of Amphiphile Self-Assembling at the Molecular Level: Supra-Molecular Assemblies with Tuned Physicochemical Properties for Delivery Applications* **2017**, 1271, 1.

[21]   K. Tatiparti, S. Sau, S. K. Kashaw, A. K. Iyer, *Nanomaterials-Basel* **2017**, 7.

[22]   C. A. Mirkin, R. L. Letsinger, R. C. Mucic, J. J. Storhoff, *Nature* **1996**, 382, 607.

[23]   M. N. O'Brien, M. R. Jones, C. A. Mirkin, *Proc. Natl. Acad. Sci. USA* **2016**, 113, 11717.

[24]   M. R. Jones, N. C. Seeman, C. A. Mirkin, *Science* **2015**, 347.

[25]   J. H. Zhu, Y. Kim, H. X. Lin, S. Z. Wang, C. A. Mirkin, *J. Am. Chem. Soc.* **2018**, 140, 5061.

[26]   H. B. Wang, W. Xu, H. Zhang, D. W. Li, Z. Q. Yang, X. J. Xie, T. H. Li, X. G. Liu, *Small* **2011**, 7, 1987.

[27]   N. L. Rosi, C. A. Mirkin, *Chem. Rev.* **2005**, 105, 1547.

[28]   J. M. Nam, C. S. Thaxton, C. A. Mirkin, *Science* **2003**, 301, 1884.

[29]   R. Elghanian, J. J. Storhoff, R. C. Mucic, R. L. Letsinger, C. A. Mirkin, *Science* **1997**, 277, 1078.

[30]   J. J. Storhoff, R. Elghanian, R. C. Mucic, C. A. Mirkin, R. L. Letsinger, *J. Am. Chem. Soc.* **1998**, 120, 1959.

[31]   T. A. Taton, C. A. Mirkin, R. L. Letsinger, *Science* **2000**, 289, 1757.

[32]   S. J. Park, T. A. Taton, C. A. Mirkin, *Science* **2002**, 295, 1503.

[33]   D. S. Seferos, A. E. Prigodich, D. A. Giljohann, P. C. Patel, C. A. Mirkin, *Nano Lett.* **2009**, 9, 308.

[34]   C. H. Choi, L. Hao, S. P. Narayan, E. Auyeung, C. A. Mirkin, *Proc. Natl. Acad. Sci. USA* **2013**, 110, 7625.

[35]   X. A. Wu, C. H. Choi, C. Zhang, L. Hao, C. A. Mirkin, *J. Am. Chem. Soc.* **2014**, 136, 7726.

[36]   J. I. Cutler, K. Zhang, D. Zheng, E. Auyeung, A. E. Prigodich, C. A. Mirkin, *J. Am. Chem. Soc.* **2011**, 133, 9254.

[37]   M. D. Massich, D. A. Giljohann, D. S. Seferos, L. E. Ludlow, C. M. Horvath, C. A. Mirkin, *Mol. Pharm.* **2009**, 6, 1934.

[38]   D. A. Giljohann, D. S. Seferos, P. C. Patel, J. E. Millstone, N. L. Rosi, C. A. Mirkin, *Nano Lett.* **2007**, 7, 3818.

[39]   S. P. Narayan, C. H. Choi, L. Hao, C. M. Calabrese, E. Auyeung, C. Zhang, O. J. Goor, C. A. Mirkin, *Small* **2015**, 11, 4173.

[40]   W. C. Song, K. R. Kim, M. Park, K. E. Lee, D. R. Ahn, *Biomaterials science* **2017**.

[41]   D. Zheng, D. A. Giljohann, D. L. Chen, M. D. Massich, X. Q. Wang, H. Iordanov, C. A. Mirkin, A. S. Paller, *Proc. Natl. Acad. Sci. USA* **2012**, 109, 11975.

[42]   R. J. Banga, N. Chernyak, S. P. Narayan, S. T. Nguyen, C. A. Mirkin, *J. Am. Chem. Soc.* **2014**, 136, 9866.

[43]   J. D. Brodin, A. J. Sprangers, J. R. McMillan, C. A. Mirkin, *J. Am. Chem. Soc.* **2015**, 137, 14838.

[44]   S. Y. Wu, G. Lopez-Berestein, G. A. Calin, A. K. Sood, *Sci. Transl. Med.* **2014**, 6, 240ps7.

[45]   C. V. Dang, E. P. Reddy, K. M. Shokat, L. Soucek, *Nat. Rev. Cancer* **2017**, 17, 502.

[46]   N. L. Rosi, D. A. Giljohann, C. S. Thaxton, A. K. Lytton-Jean, M. S. Han, C. A. Mirkin, *Science* **2006**, 312, 1027.

[47]   S. A. Jensen, E. S. Day, C. H. Ko, L. A. Hurley, J. P. Luciano, F. M. Kouri, T. J. Merkel, A. J. Luthi, P. C. Patel, J. I. Cutler, W. L. Daniel, A. W. Scott, M. W. Rotz, T. J. Meade, D. A. Giljohann, C. A. Mirkin, A. H. Stegh, *Sci. Transl. Med.* **2013**, 5, 209ra152.

[48]   K. L. Young, A. W. Scott, L. L. Hao, S. E. Mirkin, G. L. Liu, C. A. Mirkin, *Nano Lett.* **2012**, 12, 3867.

[49]   C. Zhang, L. L. Hao, C. M. Calabrese, Y. Zhou, C. H. J. Choi, H. Xing, C. A. Mirkin, *Small* **2015**, 11, 5360.

[50]   A. J. Sprangers, L. Hao, R. J. Banga, C. A. Mirkin, *Small* **2017**, 13.

[51]   X. Liang, W. Shen, H. Sun, T. Prakash, S. T. Crooke, *Mol Biol Cell* **2013**, 24.

[52]   A. F. Radovic-Moreno, N. Chernyak, C. C. Mader, S. Nallagatla, R. S. Kang, L. L. Hao, D. A. Walker, T. L. Halo, T. J. Merkel, C. H. Rische, S. Anantatmula, M. Burkhart, C. A. Mirkin, S. M. Gryaznov, *Proc. Natl. Acad. Sci. USA* **2015**, 112, 3892.

[53]   J. R. Ferrer, J. A. Wertheim, C. A. Mirkin, *Bioconjug Chem* **2019**, 30, 944.

[54]   S. Dhar, W. L. Daniel, D. A. Giljohann, C. A. Mirkin, S. J. Lippard, *J. Am. Chem. Soc.* **2009**, 131, 14652.

[55]   T. S. Alster, T. B. West, *Ann. Plast. Surg.* **1997**, 39, 418.

[56]   C. I. Jacob, J. S. Dover, M. S. Kaminer, *J. Am. Acad. Dermatol.* **2001**, 45, 109.

[57]   A. Bayat, D. A. McGrouther, *Br. J. Hosp. Med.* **2006**, 67, 527.

[58]   D. Leventhal, M. Furr, D. Reiter, *Arch. Facial Plast. Surg.* **2006**, 8, 362.

[59]   L. Brown, R. Langer, *Annu. Rev. Med.* **1988**, 39, 221.

[60]   S. Mitragotri, *Nat. Rev. Immunol.* **2005**, 5, 905.

[61]   M. R. Prausnitz, R. Langer, *Nat. Biotechnol.* **2008**, 26, 1261.

[62]   T. Hsu, S. Mitragotri, *Proc. Natl. Acad. Sci. USA* **2011**, 108, 15816.

[63]   M. Eghbali, *Cardiovasc Pathol* **1993**, 2, 199.

[64]   D. A. Bettinger, D. R. Yager, R. F. Diegelmann, I. K. Cohen, *Plast. Reconstr. Surg.* **1996**, 98, 827.

[65]   G. R. Grotendorst, *Cytokine Growth Factor Rev* **1997**, 8, 171.

[66]   H. Ihn, *Curr Opin Rheumatol* **2002**, 14, 681.

[67]   J. A. Arnott, E. Nuglozeh, M. Rico, T. A. Owen, F. F. Safadi, S. Popoff, *Mol Biol Cell* **2004**, 15, 417a.

[68]   C. T. Laurencin, R. Langer, *Clin Lab Med* **1987**, 7, 301.

[69]   M. R. Prausnitz, V. G. Bose, R. Langer, J. C. Weaver, *Proc. Natl. Acad. Sci. USA* **1993**, 90, 10504.

[70]   G. G. Gauglitz, H. C. Korting, T. Pavicic, T. Ruzicka, M. G. Jeschke, *Mol. Med.* **2011**, 17, 113.

[71]   G. J. Goodman, *Dermatol. Surg.* **2000**, 26, 857.

[72]   D. Zheng, D. A. Giljohann, D. L. Chen, M. D. Massich, X. Q. Wang, H. Iordanov, C. A. Mirkin, A. S. Paller, *Proc. Natl. Acad. Sci. USA* **2012**, 109, 11975.

[73]   J. I. Cutler, E. Auyeung, C. A. Mirkin, *J. Am. Chem. Soc.* **2012**, 134, 1376.

[74]   N. Pernodet, X. H. Fang, Y. Sun, A. Bakhtina, A. Ramakrishnan, J. Sokolov, A. Ulman, M. Rafailovich, *Small* **2006**, 2, 766.

[75]   K. A. Whitehead, R. Langer, D. G. Anderson, *Nat. Rev. Drug Discov.* **2009**, 8, 516.

[76]   B. Meckes, R. J. Banga, S. T. Nguyen, C. A. Mirkin, *Small* **2017**.

[77]   S. Sur, A. C. Fries, K. W. Kinzler, S. B. Zhou, B. Vogelstein, *Proc. Natl. Acad. Sci. USA* **2014**, 111, 2283.

[78]   T. G. Park, *Biomaterials* **1995**, 16, 1123.

[79]   Y. M. Wang, H. Sato, I. Horikoshi, *J. Control. Release* **1997**, 49, 157.

[80]   H. K. Makadia, S. J. Siegel, *Polymers* **2011**, 3, 1377.

[81]   S. Fredenberg, M. Wahlgren, M. Reslow, A. Axelsson, *Int. J. Pharm.* **2011**, 415, 34.

[82]   F. Danhier, E. Ansorena, J. M. Silva, R. Coco, A. Le Breton, V. Preat, *J. Control. Release* **2012**, 161, 505.

[83]   E. Locatelli, M. C. Franchini, *J. Nanopart. Res.* **2012**, 14.

[84]   J. Nicolas, S. Mura, D. Brambilla, N. Mackiewicz, P. Couvreur, *Chem. Soc. Rev.* **2013**, 42, 1147.

[85]   H. Sah, L. A. Thoma, H. R. Desu, E. Sah, G. C. Wood, *Int. J. Nanomedicine* **2013**, 8, 747.

[86]   S. Sharma, A. Parmar, S. Kori, R. Sandhir, *Trac-Trend Anal Chem* **2016**, 80, 30.

[87]   R. A. Jain, *Biomaterials* **2000**, 21, 2475.

[88]   C. E. Astete, C. M. Sabliov, *J. Biomater. Sci. Polym. Ed.* **2006**, 17, 247.

[89]   M. L. Houchin, E. M. Topp, *J Pharm Sci* **2008**, 97, 2395.

[90]   H. Murakami, M. Kobayashi, H. Takeuchi, Y. Kawashima, *Int. J. Pharm.* **1999**, 187, 143.

[91]   T. Govender, S. Stolnik, M. C. Garnett, L. Illum, S. S. Davis, *J. Control. Release* **1999**, 57, 171.

[92]   J. H. Jeong, T. G. Park, *Bioconjug Chem* **2001**, 12, 917.

[93]   J. M. Barichello, M. Morishita, K. Takayama, T. Nagai, *Drug Dev. Ind. Pharm.* **1999**, 25, 471.

[94]   C. J. M. Rivas, M. Tarhini, W. Badri, K. Miladi, H. Greige-Gerges, Q. A. Nazari, S. A. G. Rodriguez, R. A. Roman, H. Fessi, A. Elaissari, *Int. J. Pharm.* **2017**, 532, 66.

[95]   H. A. Almoustafa, M. A. Alshawsh, Z. Chik, *Int. J. Pharm.* **2017**, 533, 275.

[96]   L. Tang, X. J. Yang, Q. Yin, K. M. Cai, H. Wang, I. Chaudhury, C. Yao, Q. Zhou, M. Kwon, J. A. Hartman, I. T. Dobrucki, L. W. Dobrucki, L. B. Borst, S. Lezmig, W. G. Helferich, A. L. Ferguson, T. M. Fan, J. J. Cheng, *Proc. Natl. Acad. Sci. USA* **2014**, 111, 15344.

[97]   L. Zhang, J. M. Chan, F. X. Gu, J. W. Rhee, A. Z. Wang, A. F. Radovic-Moreno, F. Alexis, R. Langer, O. C. Farokhzad, *ACS Nano* **2008**, 2, 1696.

[98]   A. M. Chen, M. Zhang, D. G. Wei, D. Stueber, O. Taratula, T. Minko, H. X. He, *Small* **2009**, 5, 2673.

[99]   X. Y. Xu, K. Xie, X. Q. Zhang, E. M. Pridgen, G. Y. Park, D. S. Cui, J. J. Shi, J. Wu, P. W. Kantoff, S. J. Lippard, R. Langer, G. C. Walker, O. C. Farokhzad, *Proc. Natl. Acad. Sci. USA* **2013**, 110, 18638.

[100]   N. Nafee, S. Taetz, M. Schneider, U. F. Schaefer, C. M. Lehr, *Nanomed-Nanotechnol* **2007**, 3, 173.

[101]   M. D. Massich, D. A. Giljohann, A. L. Schmucker, P. C. Patel, C. A. Mirkin, *ACS Nano* **2010**, 4, 5641.

[102]   M. Dunne, O. I. Corrigan, Z. Ramtoola, *Biomaterials* **2000**, 21, 1659.

[103]   C. Fonseca, S. Simoes, R. Gaspar, *J. Control. Release* **2002**, 83, 273.

[104]   M. L. Zweers, G. H. Engbers, D. W. Grijpma, J. Feijen, *J. Control. Release* **2004**, 100, 347.

[105]   S. Gao, F. Dagnaes-Hansen, E. J. B. Nielsen, J. Wengel, F. Besenbacher, K. A. Howard, J. Kjems, *Mol. Ther.* **2009**, 17, 1225.

[106]   I. M. Hafez, N. Maurer, P. R. Cullis, *Gene Ther.* **2001**, 8, 1188.

[107]   J. E. Summerton, *Therapeutic Oligonucleotides: Transcriptional and Translational Strategies for Silencing Gene Expression* **2005**, 1058, 62.

[108]   H. Shen, A. L. Ackerman, V. Cody, A. Giodini, E. R. Hinson, P. Cresswell, R. L. Edelson, W. M. Saltzman, D. J. Hanlon, *Immunology* **2006**, 117, 78.

[109]   J. Gilleron, W. Querbes, A. Zeigerer, A. Borodovsky, G. Marsico, U. Schubert, K. Manygoats, S. Seifert, C. Andree, M. Stoter, H. Epstein-Barash, L. Zhang, V. Koteliansky, K. Fitzgerald, E. Fava, M. Bickle, Y. Kalaidzidis, A. Akinc, M. Maier, M. Zerial, *Nat. Biotechnol.* **2013**, 31, 638.

[110]   T. F. Martens, K. Remaut, J. Demeester, S. C. De Smedt, K. Braeckmans, *Nano Today* **2014**, 9, 344.

[111]   M. S. Cartiera, K. M. Johnson, V. Rajendran, M. J. Caplan, W. M. Saltzman, *Biomaterials* **2009**, 30, 2790.

[112]   C. Peetla, S. Jin, J. Weimer, A. Elegbede, V. Labhasetwar, *Langmuir* **2014**, 30, 7522.

[113]   J. E. Summerton, *Ann N Y Acad Sci* **2005**, 1058, 62.

[114]   G. J. Tesz, M. Aouadi, M. Prot, S. M. Nicoloro, E. Boutet, S. U. Amano, A. Goller, M. Wang, C. A. Guo, W. E. Salomon, J. V. Virbasius, R. A. Baum, M. J. O'Connor, E. Soto, G. R. Ostroff, M. P. Czech, *Biochem J* **2011**, 436, 351.

[115]   E. Frohlich, *Int. J. Nanomedicine* **2012**, 7, 5577.

[116]   I. E. Fernandez, O. Eickelberg, *Lancet* **2012**, 380, 680.

[117]   M. Eghbali, *Cardiovasc Pathol* **1993**, 2, 199.

[118]   R. K. Moreira, *Arch Pathol Lab Med* **2007**, 131, 1728.

[119]   R. Weiskirchen, S. Weiskirchen, F. Tacke, *Mol. Aspects Med.* **2019**, 65, 2.

[120]   H. R. Fan, Q. Lin, G. R. Morrissey, P. A. Khavari, *Nat. Biotechnol.* **1999**, 17, 870.

[121]   C. Czerkinsky, J. Holmgren, *Mucosal Immunol.* **2010**, 3, 545.

[122]   E. R. Toke, O. Lorincz, Z. Csiszovszki, E. Somogyi, G. Felfoldi, L. Molnar, R. Szipocs, A. Kolonics, B. Malissen, F. Lori, J. Trocio, N. Bakare, F. Horkay, N. Romani, C. H. Tripp, P. Stoitzner, J. Lisziewicz, *Gene Ther.* **2014**, 21, 566.

[123]   S. Sengupta, D. Eavarone, I. Capila, G. L. Zhao, N. Watson, T. Kiziltepe, R. Sasisekharan, *Nature* **2005**, 436, 568.

[124]   M. E. Hegi, A. Diserens, T. Gorlia, M. Hamou, N. de Tribolet, M. Weller, J. M. Kros, J. A. Hainfellner, W. Mason, L. Mariani, J. E. C. Bromberg, P. Hau, R. O. Mirimanoff, J. G. Cairncross, R. C. Janzer, R. Stupp, *N. Engl. J. Med.* **2005**, 352, 997.

[125]   R. Babu, P. G. Kranz, V. Agarwal, R. E. McLendon, S. Thomas, A. H. Friedman, D. D. Bigner, C. Adamson, *J. Neurooncol.* **2014**, 119, 177.

[126]   C. M. Hu, S. Aryal, L. Zhang, *Ther Deliv* **2010**, 1, 323.

APPENDICES

SUPPORTING INFORMATION FOR CHAPTER 2: ATTUNATING ABNORMAL SCARS WITH LIPOSOMAL SNAS AND AUSNAS
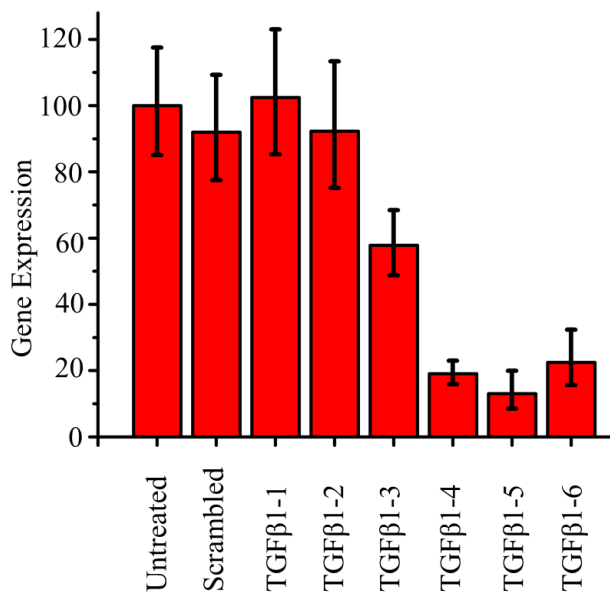
Appendix 1: Screening of antisense sequences targeting TGFβ1
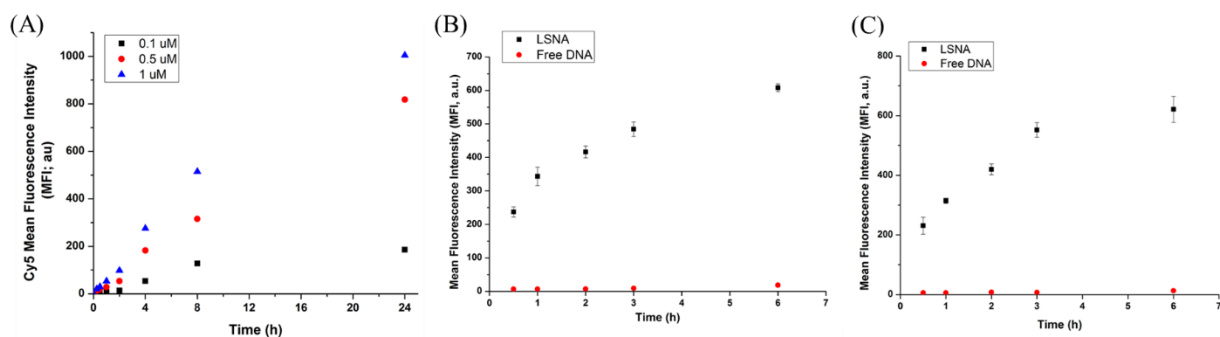
Appendix 2: Cellular uptake of LSNAs into KF and HSF cells. (A) Uptake into Rab9 (B) Uptake into KF (C) Uptake into HSF.
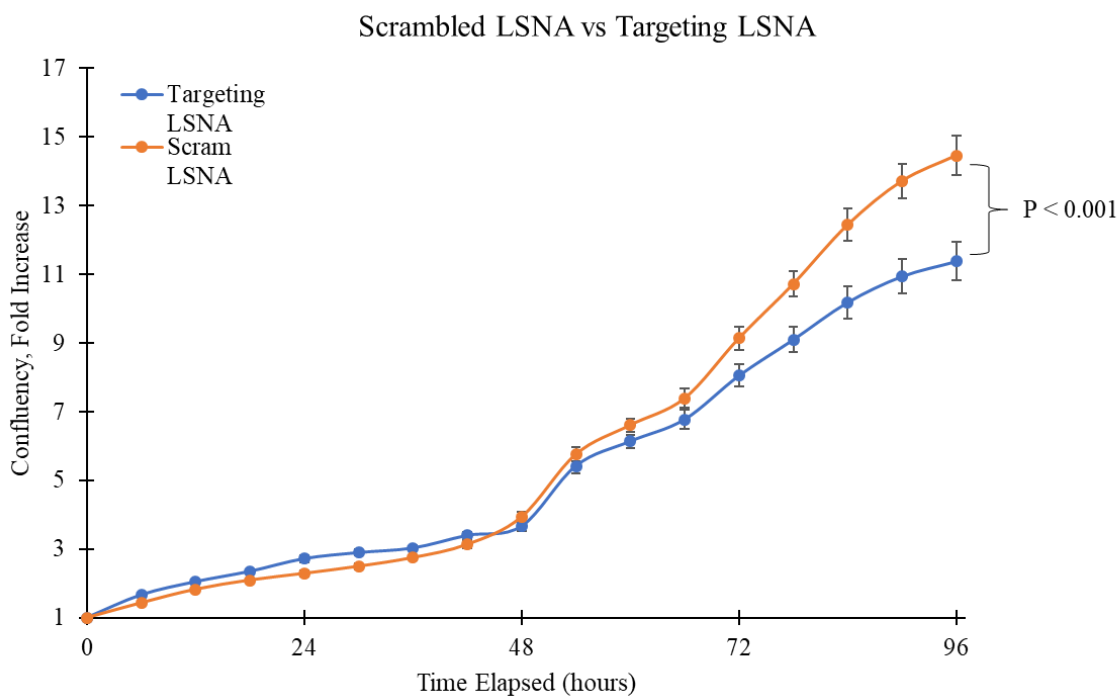
Appendix 3. Proliferation of Rab9 cells treated with TGFβ1 LSNA as compared to scrambled LSNA. Results were expressed as mean ± standard deviation of triplicates
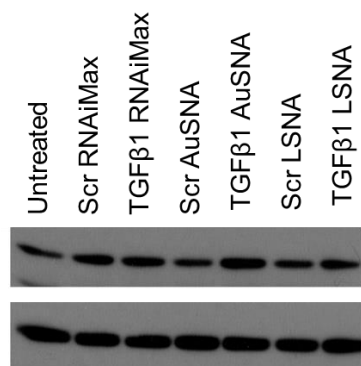
Appendix 4. AuSNAs and LSNAs targeting TGFβ1 in mouse fibroblasts (NIH 3T3).

	ddCt (mean, n=6)	Normalized expression
Rab9	13.36	1
Human HSF	5.15	29.6
Human KF110	4.82	37.2

Appendix 5. Comparison of mRNA expression levels in Rab9, HSF, and KF110 fibroblasts by qPCR

Name	Sequence	M.W	Extinction
TGFβ1 SH-DNA	5'-GCC AGC AGC CGG TTG CTG AG - (Sp18)$_2$ - SH	7091.9	186100
TTGFβ1 SH-DNA Cy3	5'-GCC AGC (Cy3) AGC CGG TTG CTG AG - (Sp18)$_2$ - SH	7598.5	191000
TGFβ1 Tocopherol-DNA	5'-(Tocopherol)-(Sp18)$_2$- GCC AGC AGC CGG TTG CTG AG	7546.5	186100
TGFβ1 Tocopherol Cy3 DNA	5'-(Tocopherol)-(Sp18)$_2$- GCC AGC AGC CGG TT (Cy3) G CTG AG	8053.1	191000
TGFβ1 Scrambled SH-DNA	5'-GTT TCA CCA CCC AAT TC - (Sp18)$_2$ - SH	5998.2	153300
TGFβ1 Scrambled Tocopherol-DNA	5'-(Tocopherol)-(Sp18)$_2$- GTT TCA CCA CCC AAT TC	6452.8	153300
TGFβ1 SH-LNA	5'-GCC +AGC AGC CGG TTG C+TG +AG - (Sp18)$_2$ - SH	7182	186100
TGFβ1 Tocopherol-LNA	5'-(Tocopherol)-(Sp18)$_2$-GCC +AGC AGC CGG TTG C+TG +AG	7636	186100
TGFβ1 Scrambled SH-LNA	5'-GT+T TCA CCA CCC A+AT +TC - (Sp18)$_2$ - SH	6088	153300
TGFβ1 Scrambled Tocopherol-LNA	5'-(Tocopherol)-(Sp18)$_2$- GT+T TCA CCA CCC A+AT +TC	6542.8	153300

Appendix 6. Oligonucleotide sequences used in this study. Plus sign indicates incorporation of locked nucleic acid.

SUPPORTING INFORMATION FOR CHAPTER 3: PLGA SPHERICAL NUCLEIC ACIDS
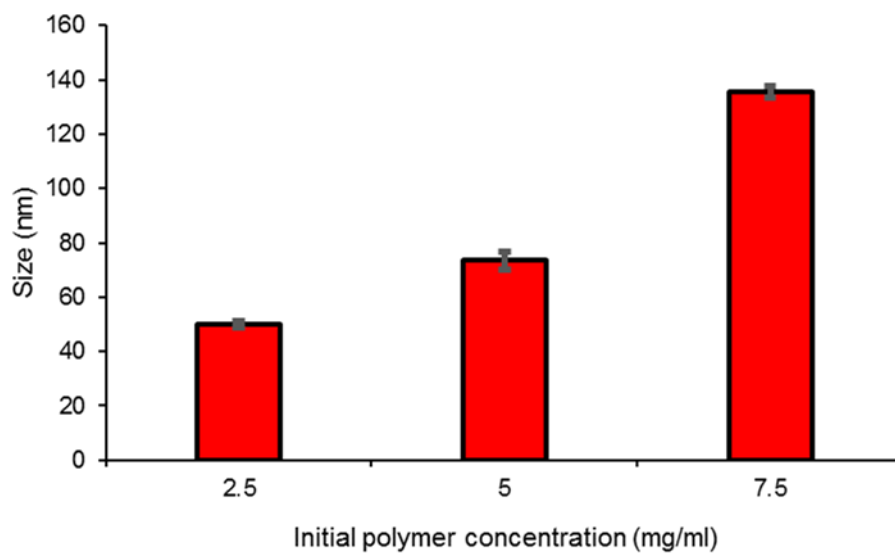
Appendix 7. Size distribution of PLGA-PEG-N$_3$ nanoparticles as a function of polymer concentration.
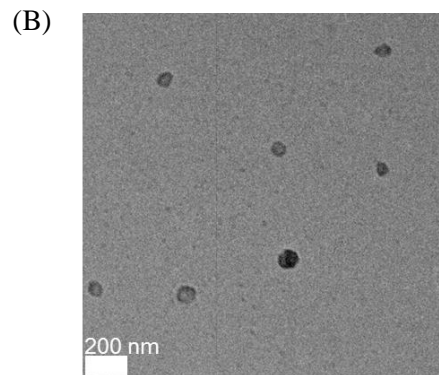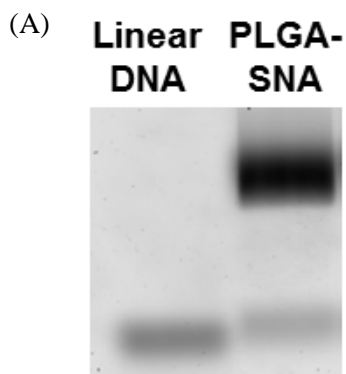
Appendix 8 (A) Linear DNA and PLGA-SNA resolved by 1% agarose gel electrophoresis (B) TEM image of PLGA-N$_3$-PEG NPs.
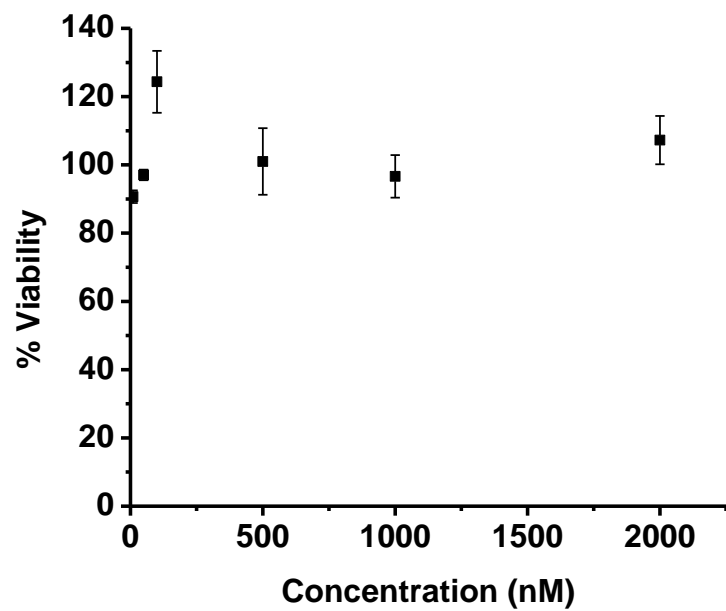
Appendix 9: Toxicity of PLGA-SNAs in Raw Blue-Macrophages

	PLGA-SNAs	ICP-SNAs	DBBC-SNAs	ProSNAs	Lipid-tail LSNAs
Core-materials	PLGA	Fe (III)	PCL	β-galactosidase	DOPC lipid
Biocompatibility	Biodegradable / biocompatible	Biocompatible	Biocompatible	Biocompatible	Biocompatible
Ease of preparation	Easy	Challenging	Challenging	Intermediate	Intermediate
Size (nm)	50	10-20	30-50	Non-spherical	50
Strands/particle	200	113	302	25	150
Surface density (pmole/cm^2)	5.2	32.6	22.2	Variable	3.2
Function of core	Encapsulation of hydrophobic agents	Template for conjugation	Template for conjugation	Enzyme delivery	Encapsulation of hydrophilic agents
Demonstrated therapeutic applications	TLR 9 activation	Knockdown Her 2	Knockdown EGFP	Enzyme delivery	TLR 9 activation
Key advantage	Co-delivery of nucleic acids with hydrophobic drugs	High surface density	High surface density	Delivery of functional enzyme and nucleic acids	Enhanced stability

Appendix 10 Comparisons between different SNA constructs that utilize click chemistry for surface functionalization

SUPPORTING INFORMATION FOR CHAPTER 4: ENHANCING GENE REGULATION WITH PLGA-SNAS
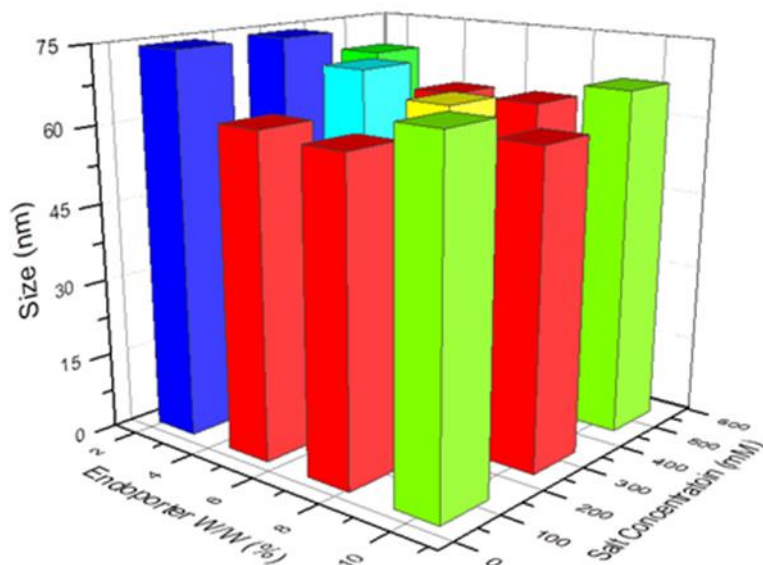
Appendix 11. Size of Endoporter-loaded PLGA nanoparticles as a function of Endoporter initial feedback amount and salt concentration
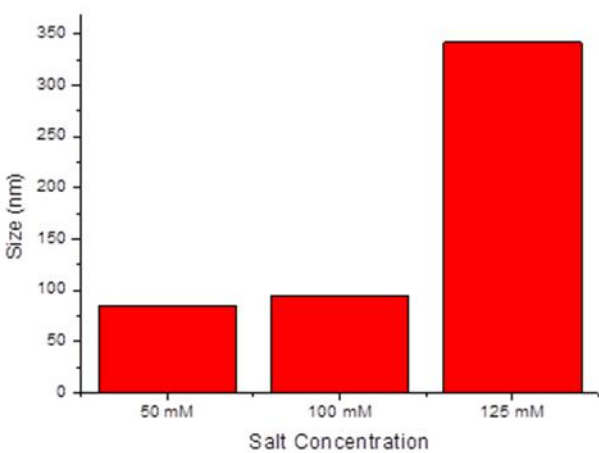
Appendix 12. Size of Endoporter-loaded (5% w/w) PLGA-SNAs as a function of salt concentration. (A) Size increase as a function of salt concentration (B) Aggregation of Endoporter-loaded PLGA-SNAs in high ionic strength solution.
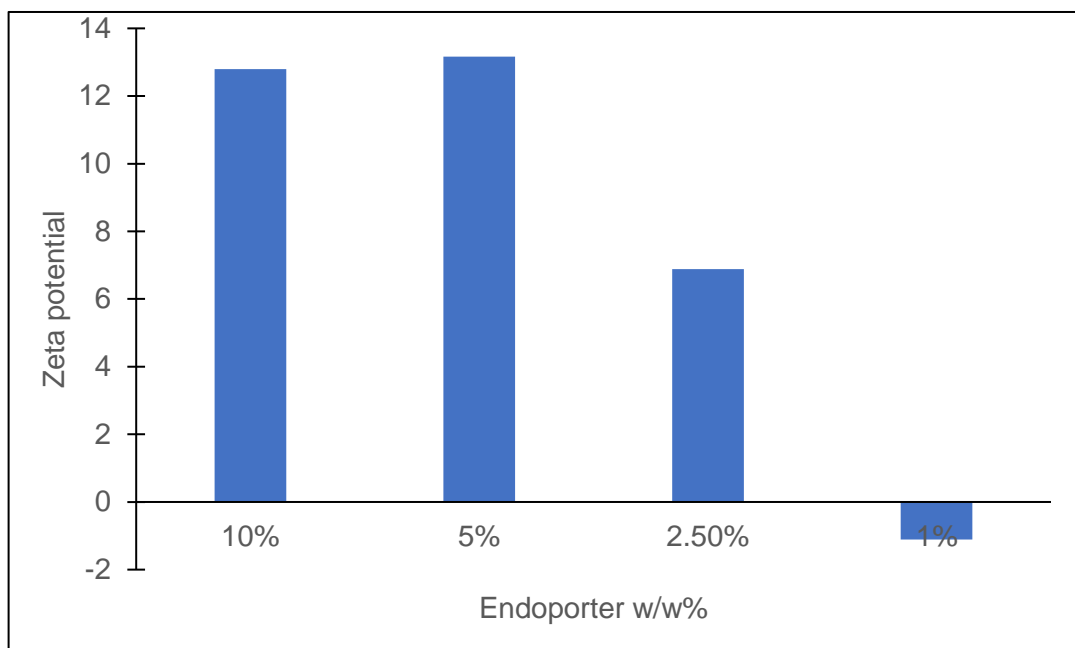
Appendix 13. Surface charge of Endoporter-loaded PLGA at various Endoporter feed concentrations

Control Particles (no Cy5-endoporter)
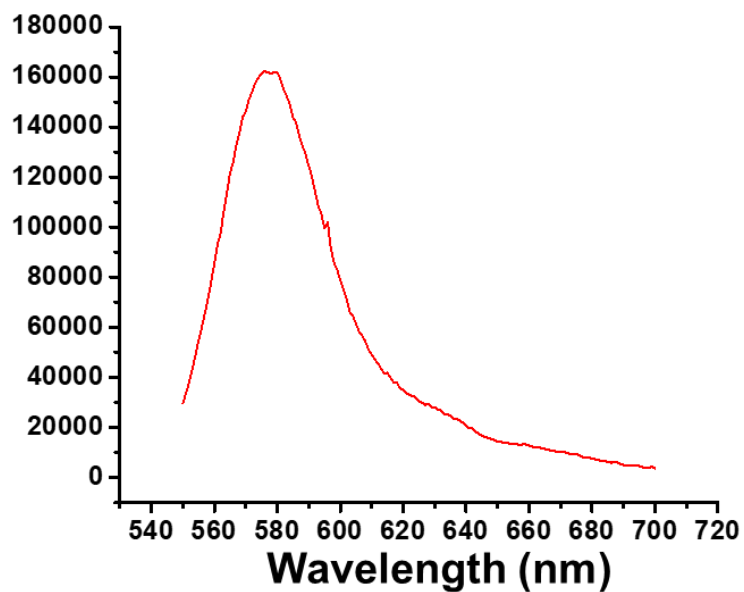
Appendix 14. FRET signal of PLGA-SNAs labelled with rhodamine as a control.
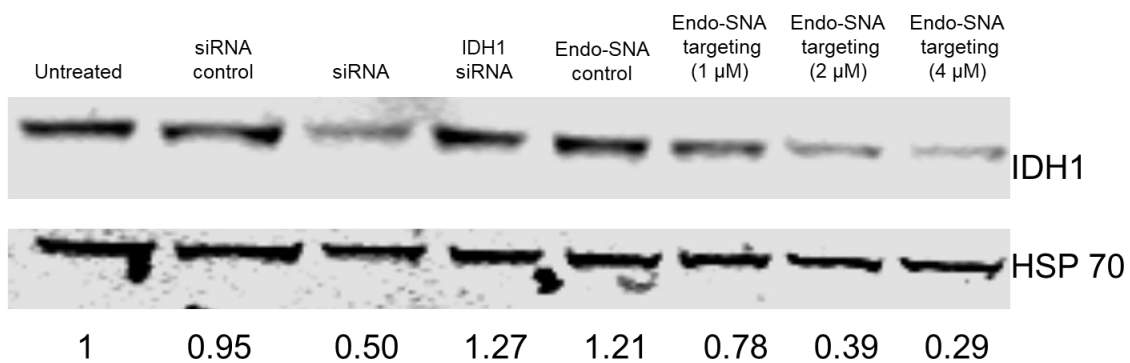
Appendix 15. Does-dependent knockdown of IDH1 by Endoporter-loaded PLGA-SNAs.
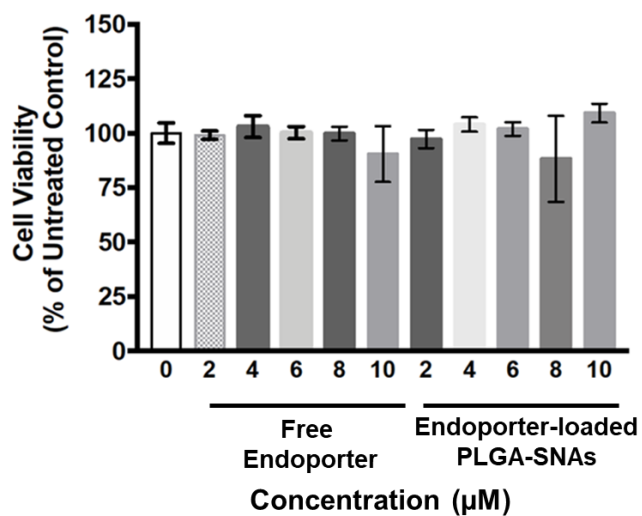
Appendix 16 Toxicity of free Endoporter and Endoporter-loaded PLGA-SNAs at various concentrations.